

TRIBOLOGY OF 316L AUSTENITIC STAINLESS STEEL
CARBURIZED AT LOW TEMPERATURE

by

LUCAS J. O'DONNELL

Submitted in partial fulfillment of the requirements for the degree of
Master of Science

Thesis Advisor: Dr. Arthur H. Heuer

Department of Materials Science Engineering

CASE WESTERN RESERVE UNIVERSITY

January 2010

CASE WESTERN RESERVE UNIVERSITY
SCHOOL OF GRADUATE STUDIES

We hereby approve the thesis/dissertation of

candidate for the _____ degree *.

(signed) _____

(chair of the committee)

(date) _____

*We also certify that written approval has been obtained for any proprietary material contained therein.

Table of Contents

List of Tables	6
List of Figures	7
Acknowledgements.....	12
Abstract.....	13
1.0 Introduction and Background	14
1.1 Austenitic Stainless Steels	14
1.2 Surface Engineering of Stainless Steels to Improve Wear Resistance	15
1.3 Low Temperature Carburization; Theory, Process, and Properties.....	16
2.0 Tribology Review.....	21
2.1 Contact of Real Surfaces.....	23
2.2 Friction and Frictional Heating	24
2.3 Contact Mechanics	29
2.3.1 Static Contact Mechanics	29
2.3.2 Contact Mechanics of Sliding Surfaces.....	31
2.3.3 Contact Mechanics and Low Temperature Carburized Materials.....	32
2.4 Sliding Wear of Metallic Materials	33
2.4.1 Simple Theory of Sliding Wear, Archard’s Wear Equation.....	33
2.4.2 Adhesive Wear.....	34
2.4.3 Oxidative Wear	38
2.4.4 Fatigue Wear and Delamination.....	41
2.4.5 Abrasive Wear	44

2.5 Wear Regime Transitions and Wear Maps	46
3.0 Materials & Methods	51
3.1 Pin-on-Disk Wear and Friction Testing.....	51
3.2 Wear Scar Characterization.....	53
3.2.1 Disk Scar	53
3.2.2 Ball Scar	55
3.3 Friction Observation.....	56
4.0 Review of Previous Carburized 316L Tribology Investigations	58
5.0 Wear of 316L Carburized at Low Temperature Sliding Against Hard Materials.....	61
5.1 Objective & Motivation	61
5.2 Experimental Materials & Methods	62
5.3 Results and Discussion	64
5.4 Summary of Wear Performance Sliding vs. Hard Materials.....	67
6.0 Wear Maps of 316L Carburized at Low Temperature	68
6.1 Objective & Motivation	68
6.2 Materials.....	68
6.3 Experimental Methods.....	70
6.3.1 Pin-on-disk Apparatus and Procedure.....	70
6.3.2 Experimental Design	70
6.3.3 Wear Scar Characterization	74
6.3.4 Wear Debris Characterization	75
6.3.5 Construction of Wear Maps	75

6.4 Results	76
6.4.1 Friction Results	76
6.3.2 Wear Volume	79
6.3.3 Wear Debris and Wear Scar Analysis	81
6.5 Wear Maps	87
6.6 Wear Maps of Carburized 316L, Summary and Conclusions	89
7.0 Relationship of the Case Hardened Region's Properties to Wear Resistance.....	91
7.1 Background and Motivation.....	91
7.2 Materials and Methods	92
7.3 Results and Discussion	96
7.3.1 Wear Results.....	96
7.3.2 Friction Results	101
7.4 Experiment 3 Summary	103
8.0 Discussion of Experimental Results	107
9.0 Summary and Conclusions	111
10.0 Recommended Work	114
Appendix	117
A1.0 Wear of Low Temperature Carburized Martensitic Precipitation Hardened Stainless Steels	117
Works Cited.....	120

List of Tables

TABLE 1 GENERAL MATERIALS SELECTION CHART FOR TRIBOLOGICAL APPLICATIONS (FROM (17), G. STOCHOWIAK, ENGINEERING TRIBOLOGY, 2005).....	23
TABLE 2 HARDNESS OF SELECTED MATERIALS FOR PIN-ON-DISK HARD COUNTERFACE STUDY, OBTAINED BY VICKERS MICROHARDNESS TESTS UTILIZING A 50 G LOAD.	62
TABLE 3 PIN-ON-DISK TEST CONDITIONS FOR CARBURIZED 316L AND NON-TREATED 316L SLIDING AGAINST VARIOUS HARD COUNTERFACE MATERIALS.....	63
TABLE 4 LOAD AND VELOCITY EFFECTS ON WEAR PIN-ON-DISK TEST CONDITIONS FOR DRY SLIDING AGAINST AN ALUMINA BALL.....	74
TABLE 5 EMPIRICAL WEAR MODEL CONSTANTS OBTAINED BY REGRESSION OF PIN-ON-DISK DATA FOR CARBURIZED AND NON-TREATED 316L STAINLESS STEEL.....	87
TABLE 6 CASE PROPERTIES VS. WEAR RESISTANCE PIN-ON-DISK TEST CONDITIONS	96

List of Figures

FIGURE 1 TTT DIAGRAM FOR 316 STAINLESS STEEL WITH TWO DIFFERENT CARBON LEVELS (FROM (5) MICHAL ET AL, ACTA MATERIALIA, 2004)	18
FIGURE 2 SWAGELOK LOW TEMPERATURE CARBURIZATION PROCESS DIAGRAM, AN EXAMPLE PROCESS (FROM (6), F. MARTIN, ELECTROCHEMICAL AND SOLID-STATE LETTERS, 2007)	20
FIGURE 3 (A.) CARBON CONCENTRATION & HARDNESS DEPTH PROFILES, AND (B.) RESIDUAL STRESS DEPTH PROFILE (FROM (5), MICHAL ET AL, ACTA MATERIALIA, 2004)	21
FIGURE 4 REAL AREA OF CONTACT BETWEEN TWO SURFACES, INSET ILLUSTRATES CONTACT BETWEEN ASPERITIES (FROM B. BHUSHAN, PRINCIPLES AND APPLICATIONS OF TRIBOLOGY, 1999 (8)). A_A REFERS TO THE APPARENT AREA OF CONTACT AND A_R REFERS TO THE REAL AREA OF CONTACT. THE INSET IS A MAGNIFIED VIEW OF THE MICRO-CONTACT.	24
FIGURE 5 PLASTIC DEFORMATION COMPONENT OF FRICTION, (A) ASPERITY CONTACT DURING SLIDING, AND (B) MICRO VIEW OF ASPERITY DURING SLIDING AND DEFORMATION INDUCED BY THE HARDER SURFACE ((8) FROM BHUSHAN, PRINCIPLES AND APPLICATIONS OF TRIBOLOGY, 1999)	25
FIGURE 6 FRICTIONAL HEATING UNDER LOW LOAD WHEN REAL AREA OF CONTACT IS LESS THAN THE APPARENT AREA OF CONTACT, AND UNDER HIGH LOAD WHEN A_R AND A_A ARE EQUAL (FROM (8), BHUSHAN, PRINCIPLES AND APPLICATIONS OF TRIBOLOGY, 1999).	27
FIGURE 7 SCHEMATIC OF THE PIN-ON-DISK TEST AS IT RELATES TO FRICTIONAL HEATING EQUATIONS 1-3 (ADAPTED FROM SIMILAR SCHEMATIC, ASHBY ET AL, TRIBOLOGY TRANSACTION, 1991 (20)).	28
FIGURE 8 HERTZIAN CONTACT AREA FOR A SPHERE ON FLAT WHERE A IS THE RADIUS OF CONTACT, σ_R IS THE RADIAL STRESS, AND σ_θ IS THE HOOP STRESS.....	30
FIGURE 9 CONTACT, ADHESION, AND TRANSFER DUE TO ELECTRON TRANSFER AND ADHESIVE BOND FORMATION, TYPICALLY THE SOFTER OR WEAKER MATERIAL IS TRANSFERRED TO THE STRONGER MATERIAL (FROM (7), STOCHOWIAK, ENGINEERING TRIBOLOGY 3 RD ED, 2005).	35
FIGURE 10 ALTERNATIVE MODELS FOR THE PRODUCTION OF WEAR DEBRIS AND DEFORMATION BY ADHESIVE CONTACT OF ASPERITIES (FROM (7), STOCHOWIAK ENGINEERING TRIBOLOGY 3 RD ED., 2005).....	37

FIGURE 11 POSSIBLE MECHANISM OF WEAR DEBRIS FORMATION DUE TO ADHESIVE TRANSFER (FROM (7), STOCHOWIAK ENGINEERING TRIBOLOGY 3 RD ED., 2005)	38
FIGURE 12 GENERAL PRINCIPAL OF OXIDATIVE WEAR (FROM (7), STOCHOWIAK ENGINEERING TRIBOLOGY 3 RD ED., 2005).	39
FIGURE 13 PROPOSED MECHANISM OF OXIDATIVE WEAR AT HIGH SPEEDS (FROM (7) STOCHOWIAK ENGINEERING TRIBOLOGY 3 RD ED., 2005).	40
FIGURE 14 PROPOSED MECHANISM OF OXIDATIVE WEAR AT LOW SLIDING SPEEDS (FROM (7), STOCHOWIAK ENGINEERING TRIBOLOGY 3 RD ED., 2005).	41
FIGURE 15 LAYERS OF STRAIN ACCUMULATION RELEVANT TO DELAMINATION WEAR. $\Delta\Gamma$ IS THE STRAIN ACCUMULATION INCREMENT AS DESCRIBED BY EQUATION 16 ABOVE, Δ_z IS THE THICKNESS OF EACH TRIBOLAYER, A IS THE RADIUS OF CIRCULAR CONTACT AREA FOR SLIDING OR ROLLING CONTACT OF A SPHERE ON A FLAT SURFACE, AND P_0 IS THE HERTZIAN CONTACT PRESSURE (FROM (13), KAPOOR, WEAR, 2000).	44
FIGURE 16 FOUR POTENTIAL MECHANISMS OF ABRASIVE WEAR, (A.) CUTTING, (B.) FRACTURE, (C.) FATIGUE, (D.) GRAIN PULL-OUT, FROM (7), STOCHOWIAK, ENGINEERING TRIBOLOGY 3 RD ED., 2005).....	45
FIGURE 17 TWO-BODY AND THREE-BODY ABRASIVE WEAR (FROM (7), STOCHOWIAK, ENGINEERING TRIBOLOGY 3 RD ED., 2005).	46
FIGURE 18 WEAR REGIME TRANSITION FOR DRY SLIDING OF A BRASS PIN AGAINST A STELLITE RING (FROM (15), HERST AND LANCASTER, JOURNAL OF APPLIED PHYSICS, 1956).....	47
FIGURE 19 VARIATION IN WEAR RATE WITH SLIDING SPEED FOR BRASS SLIDING AGAINST STEEL IN AIR AND PURE OXYGEN AT VARIOUS TEMPERATURES (FROM LANCASTER J.K., PROCEEDINGS OF THE ROYAL SOCIETY OF LONDON, 1963 (16)).	49
FIGURE 20 WEAR MAP FOR DRY PIN-ON-DISK SLIDING OF STEEL AGAINST STEEL (FROM LIM, ASHBY, AND BRUNTON, ACTA MET, 1987 (17)).....	50
FIGURE 21 GENERALIZED PIN-ON-DISK WEAR TEST SETUP (FROM BLAU, WEAR, 2007 (19)).	52
FIGURE 22 EXAMPLE WEAR SCAR PROFILE OBTAINED BY LASER SCANNING CONFOCAL MICROSCOPY.....	54
FIGURE 23 EXAMPLE FRICTION PROFILE FOR CARBURIZED 316L SLIDING AGAINST A WC BALL AT 0.1 M/S UNDER A 5 N APPLIED LOAD.....	57

FIGURE 24 EFFECTS OF TEMPERATURE ON WEAR BEHAVIOR UNDER DRY SLIDING CONDITIONS (BALL/DISK), (FROM (19), QU ET AL, WEAR, 2007).	58
FIGURE 25 EFFECTS OF TEMPERATURE ON FRICTION UNDER DRY SLIDING CONDITIONS (BALL/DISK), (FROM (19), QU ET AL, WEAR, 2007).	59
FIGURE 26 WEAR IN SALT WATER, (FROM (19), QU ET AL, WEAR, 2007).	59
FIGURE 27 ABRASIVE WEAR TEST COMPARISON, (FROM (19), QU ET AL, WEAR, 2007).	60
FIGURE 28 WEAR RATE OF TREATED 316 DISKS VS. VARIOUS COUNTERFACE MATERIALS FOR (A.) THIS EXPERIMENT, AND (B.) PREVIOUS ORNL DATA (19), (T=CARBURIZED 316L, NT=NON- TREATED 316L).	65
FIGURE 29 WEAR RATE COMPARISON OF VARIOUS MATERIAL PAIRS FOR (A.) GREEN - CWRU NON- TREATED 316L RESULTS, (B.) BLUE - ORNL TREATED 316L RESULTS, AND (C.) RED - ORNL BLAU & QU RESULTS (19), (T= TREATED 316L AND NT=NON-TREATED 316L).	65
FIGURE 30 FRICTION COMPARISON FOR (A.) NON-TREATED 316L DATA FROM CWRU, AND (B.) TREATED 316L DATA FROM ORNL (19), (T=CARBURIZED 316L, NT=NON-TREATED 316L).	67
FIGURE 31 OPTICAL MICROGRAPH OF CARBURIZED 316L MICROGRAPH OBTAINED USING NOMARSKI CONTRAST.	69
FIGURE 32 HARDNESS DEPTH PROFILE OF CARBURIZED 316L OBTAINED USING A 10 G LOAD AND A BUEHLER MICROHARDNESS TESTER	69
FIGURE 33 SURFACE SHEAR STRESS DISTRIBUTION DUE TO TRACTION FOR DRY SLIDING OF AN Al_2O_3 BALL AGAINST A STAINLESS STEEL DISK UNDER NORMAL LOADS OF 5 N, 40 N, AND 2 N FOR AN ASSUMED COEFFICIENT OF FRICTION EQUAL TO 0.8. $K_{MATERIAL}$ IS THE APPROXIMATE SHEAR STRENGTH OF CARBURIZED 316L (T_{316}) AND NON-TREATED 316L (NT_{316}), τ IS THE SHEAR STRESS DUE TO NORMAL LOAD AND TRACTION, AND x/A IS THE NORMALIZED DISTANCE FROM THE CENTER OF THE CIRCULAR CONTACT AREA.	72
FIGURE 34 FLASH TEMPERATURE APPROXIMATION FOR DRY SLIDING OF AN ALUMINA BALL AGAINST A 316L STAINLESS STEEL DISK	73
FIGURE 35 STEADY STATE COF OBSERVED FOR 0.1 M/S DRY SLIDING AGAINST ALUMINA	77
FIGURE 36 STEADY STATE COEFFICIENT OF FRICTION OBSERVED FOR 0.3 M/S DRY SLIDING AGAINST ALUMINA.....	78

FIGURE 37 STEADY STATE COEFFICIENT OF FRICTION FOR 0.6 M/S DRY SLIDING AGAINST ALUMINA	78
FIGURE 38 PIN-ON-DISK TEST RESULTS COMPARING (A.) NON-TREATED 316L STAINLESS STEEL, AND (B.) CARBURIZED 316L STAINLESS STEEL	80
FIGURE 39 WEAR DEBRIS GENERATED AT 0.1 M/S COMPARING (A.) NON-TREATED 316L UNDER 4N APPLIED LOAD, (B.) NON-TREATED 316L UNDER 40N APPLIED LOAD, (C.) CARBURIZED 316L UNDER 4N APPLIED LOAD; HIGHLIGHTED AREA REFERS TO FIGURE 6, (D.) CARBURIZED 316L UNDER 40N APPLIED LOAD.....	82
FIGURE 40 XEDS SPECTRUM SHOWING THE HIGH OXYGEN LEVEL PRESENT ON CARBURIZED FLAKE DEBRIS RESULTING FROM SLIDING UNDER A 4 N LOAD AT 0.1 M/S; THE INSET IS A MAGNIFIED IMAGE OF THE OXIDE LAYER HIGHLIGHTED IN FIG. 5C.	83
FIGURE 41 WEAR SCARS GENERATED UNDER 40 N APPLIED LOAD AND 0.1 M/S FOR (A.) NON- TREATED 316L, AND (B.) CARBURIZED 316L	83
FIGURE 42 WEAR SCARS GENERATED UNDER 40 N APPLIED LOAD AND 0.3 M/S SLIDING (A.) NON- TREATED 316L (B.) CARBURIZED 316L	84
FIGURE 43 COMPARISON OF WEAR DEBRIS GENERATED AT 0.3 M/S SLIDING SPEED FOR (A.) NON- TREATED 316L UNDER 4 N APPLIED LOAD, (B.) NON-TREATED 316L UNDER 40 N APPLIED LOAD, (C.) CARBURIZED 316L UNDER 4 N APPLIED LOAD, AND (D.) CARBURIZED 316L UNDER 40 N APPLIED LOAD	84
FIGURE 44 COMPARISON OF WEAR DEBRIS GENERATED AT 0.3 M/S SLIDING SPEED FOR (A.) NON- TREATED 316L UNDER 4 N APPLIED LOAD, (B.) NON-TREATED 316L UNDER 40 N APPLIED LOAD, (C.) CARBURIZED 316L UNDER 4 N APPLIED LOAD, AND (D.) CARBURIZED 316L UNDER 40 N APPLIED LOAD	86
FIGURE 45 WEAR SCARS GENERATED UNDER 40 N APPLIED LOAD AND 0.6 M/S SLIDING FOR (A.) NON-TREATED 316L, AND (B.) CARBURIZED 316L.....	86
FIGURE 46 WEAR SCARS GENERATED UNDER 40 N APPLIED LOAD AND 0.6 M/S SLIDING FOR (A.) NON-TREATED 316L, AND (B.) CARBURIZED 316L.....	86
FIGURE 47 PARITY PLOTS SHOWING THE GOODNESS OF FIT FOR THE EMPIRICAL MODEL DEVELOPED FROM PIN-ON-DISK DATA FOR (A.) NON-TREATED 316L STAINLESS STEEL, AND (B.) CARBURIZED 316L.....	88

FIGURE 48 WEAR MAPS COMPARING THE OBSERVED DRY SLIDING WEAR BEHAVIOR UNDER VARIOUS LOADS AND SLIDING SPEEDS FOR (A.) NON-TREATED 316L, AND (B.) CARBURIZED 316L; THE CONTOUR LINES REPRESENT THE VOLUME OF MATERIAL LOST BY WEAR (MM ³) FOR THE VARIOUS CONDITIONS	89
FIGURE 49 CARBURIZED 316L DISK SURFACE HARDNESS (VICKERS, 50 G LOAD) AFTER ELECTROPOLISHING.....	92
FIGURE 50 CARBURIZED 316L OF VARYING SURFACE HARDNESS AND CASE DEPTHS OF (A.) 10 MM, (B.) 15 MM, (C.) 18 MM, (D.) 25 MM, (E.) 30 MM, AND (F.) 32 MM.....	93
FIGURE 51 GDOES COMPOSITION DEPTH PROFILE OF LOW TEMPERATURE CARBURIZED 316L, NOTE THE INACCURACY OF THE CARBON RICH REGION COMPARED TO THAT OBSERVED BY MICROSTRUCTURAL ANALYSIS (FIG. 50). (GDOES FIGURE PROVIDED BY SWAGELOK CO.)	94
FIGURE 52 WEAR VS. CASE THICKNESS FOR CARBURIZED 316L SLIDING AT 0.1 M/S AGAINST ALUMINA UNDER A 5 N APPLIED LOAD.....	97
FIGURE 53 INFLUENCE OF CARBURIZED 316L SURFACE HARDNESS ON WEAR WHEN SLIDING AGAINST ALUMINA UNDER AN APPLIED LOAD OF 5 N AT 0.1 M/S.....	98
FIGURE 54 DISK AND BALL WEAR FOR AN ALUMINA BALL SLIDING AT 0.1 M/S UNDER AN APPLIED LOAD OF 40 N AGAINST CARBURIZED 316L DISKS OF VARIOUS CASE THICKNESSES AND SURFACE HARDNESSES.....	99
FIGURE 55 INFLUENCE OF CARBURIZED 316L SURFACE HARDNESS ON WEAR WHEN SLIDING AGAINST ALUMINA UNDER AN APPLIED LOAD OF 40 N AT 0.1 M/S.....	100
FIGURE 56 (A.) DISK WEAR SCAR DEPTH VS. CASE THICKNESS OF CARBURIZED 316L DISKS FOR 0.1 M/S SLIDING AGAINST AN ALUMINA BALL, AND (B.) ENLARGED VIEW OF SELECTED REGION FROM 56A, ILLUSTRATING THE SHARP CHANGE TO NON-TREATED LIKE WEAR ONCE THE CASE HARDENED REGION IS WORN THROUGH	101
FIGURE 57 STEADY STATE FRICTION FOR DRY 0.1 M/S SLIDING OF AN ALUMINA BALL VS. CARBURIZED 316L DISKS; (A.) FRICTION VS. THICKNESS OF CARBURIZED REGION AFTER ELECTROPOLISHING, AND (B.) FRICTION VS. SURFACE HARDNESS OF CARBURIZED DISK AFTER ELECTROPOLISHING.....	103

Acknowledgements

I would like to gratefully acknowledge the guidance and insight of my thesis advisor, Dr. Arthur H. Heuer, and the faculty of Case Western Reserve University whom collaborated on this project; Dr. Gary M. Michal, Dr. Frank Ernst, and Dr. Hal Kahn. We would also like to thank Dr. Peter Blau and Dr. Jun Qu (Oak Ridge National Labs) for helpful discussions and training, Dr. David Hovis (CWRU) for assistance with laser confocal microscopy and wear scar imaging, and the Swagelok Co. for low temperature carburization of all specimens.

This work was funded by an Ohio Department of Development Third Frontier Grant.

Tribology of 316L Austenitic Stainless Steel Carburized at Low Temperature

Abstract

by

LUCAS J. O'DONNELL

Historically it has been very difficult to harden the surface of stainless steels without the loss of corrosion resistance. A novel low temperature carburization process developed by Swagelok Co. which greatly improves the wear resistance of stainless steel has accomplished this feat. This project has studied the friction and wear behavior of low temperature carburized AISI 316L; 1.) Sliding against hard materials, 2.) Sliding under a range of contact stresses and sliding speeds, and 3.) The relationship of wear resistance to the properties of the surface hardened region. It was found that low temperature carburization provided an immense improvement in wear resistance when sliding against hard materials, and this improvement is maintained under stresses and sliding speeds that are too severe for non-treated stainless steels. Furthermore, the improvement in wear resistance was found to be heavily dependent on the hardness and thickness of the case hardened region.

1.0 Introduction and Background

1.1 Austenitic Stainless Steels

The material of focus throughout this project is austenitic stainless steel AISI 316L. Austenitic stainless steels are iron based alloys which have a face centered cubic structure that is obtained by heavy alloying with austenizing elements such as Ni, Mn, and N. The austenitic family of stainless steel has a general composition of 16-25 at% Cr, residual-20 at% Ni, up to 18 at% Mn, and minor amounts of other alloying elements. Austenitic stainless steels are widely used and well known for their exceptionally high toughness, good ductility, formability, high impact energy, and excellent corrosion resistance (1). Austenitic alloys are most commonly used in low carbon annealed form. AISI 316L, is the “low carbon” form of AISI 316. AISI 316L has a general composition of 0.03max at% C, 17 at% Cr, 12 at% Ni, 2.5 at% Mo, and minor amounts of other alloying elements. The low carbon austenitic alloys are formulated to avoid the formation of chromium carbides which result in a depletion of chromium from the austenite matrix and a loss in corrosion resistance; this phenomenon is referred to as sensitization (2). Strong carbide formers, such as Nb and Ti, are often alloyed with these materials in order to prevent the formation of chromium bearing carbides. Austenitic stainless steels generally have better corrosion resistance than ferritic and martensitic steels. (1)

AISI 316L, is very widely used for its corrosion resistance, and generally has better mechanical properties, and corrosion resistance in certain environments, such as dilute sulfuric acid, than other 300 series stainless steels such as 304 or 321 (1). One strong limitation of austenitic stainless steels is their poor wear resistance. These

materials are generally quite soft, and thus are susceptible to many common forms of wear and contact damage (1). Because of the inherently poor wear resistance of these alloys, their range of potential application is limited. For this reason, hardening the surface of stainless steels to improve wear resistance without deteriorating other desirable properties is of great interest, and is the focus of this project.

1.2 Surface Engineering of Stainless Steels to Improve Wear Resistance

“Surface Engineering” is a general phrase that describes a very broad range of processes which alter a materials surface to improve surface properties or modify a materials interaction with the surrounding environment. The most common surface engineering technologies applied to steel alloys include transformation hardening, surface melting, conventional carburization, conventional nitriding, coating, and plating. Surface hardening of stainless steels for improved wear resistance while maintaining corrosion resistance and ductility has historically been very difficult. Traditional carburization carried out at temperatures over 900°C can significantly harden the surface of austenitic stainless steels; however, the unavoidable formation of chromium carbides causes a depletion of chromium from the matrix within the case hardened layer, deteriorating the corrosion resistance of the alloy (2, 3). Nitriding techniques can also be used to significantly harden the surface of these materials, however the surface layer can become very brittle, and if chromium nitrides form corrosion resistance can be lost (4, 5). Many other surface engineering methods are available for use with stainless steels, such as coating or electroplating, however each has significant weaknesses. This

research project focuses on a new surface engineering technology, developed by the Swagelok Co. (Solon, OH), that significantly hardens the surface of stainless steels without adversely affecting corrosion resistance by kinetically limiting the formation of chromium carbides.

1.3 Low Temperature Carburization; Theory, Process, and Properties

The Swagelok low temperature carburization process diffuses carbon into the surface of stainless steel and results in significant hardening by achieving a “colossal” super saturation of carbon within the matrix of austenitic stainless steels. Carburized austenitic stainless steels have been experimentally proven to display many improved properties including fatigue life, surface hardness, wear resistance, and corrosion resistance (6-9). Furthermore, these improvements are obtained without a significant decrease in ductility which has been experimentally demonstrated by tensile strength tests and Transmission Electron Microscopy (TEM) observations of dislocation densities within case hardened TEM foils (3). It is clear that these austenitic stainless steel property improvements will lead to improved performance in many applications, and could potentially introduce austenitic stainless steels into applications that would typically be considered too harsh for this class of alloys.

The improved properties achieved by low temperature carburization are a result of the extremely high concentration of carbon reached within the surface region of the treated material. It is possible to achieve such high carbon concentrations due to the greatly increased solubility of carbon in the austenitic stainless steel matrix under

paraequilibrium conditions. The term “paraequilibrium” is used to describe the state of a system in which some but not all of its components are in thermodynamic equilibrium. This thermodynamic state can be reached when some species in the system are mobile while others are rendered immobile due to kinetically suppressed diffusion (4). Paraequilibrium is important to low temperature carburization because under these processing conditions carbon is highly mobile with respect to chromium and nickel, which are essentially frozen at these temperatures thus preventing long range diffusion (12). Therefore, during low temperature carburization, carbon diffuses into the stainless steel due to the chemical potential driving force provided by the carbon rich treatment atmosphere, and would eventually reach a state of paraequilibrium if provided enough time. Meanwhile, chromium and other substitutional solutes are not able to diffuse despite the chemical potential driving force that is created as carbon diffuses into the material. This concept is what enables such high concentrations of carbon to be dissolved within the austenitic stainless steel matrix without the formation of equilibrium carbides.

The low temperature carburization process achieves a surface carbon concentration of roughly 12 at% for austenitic stainless steel grade AISI 316L, resulting in a surface hardness of ≈ 12 GPa (5). This high carbon concentration in the austenite matrix is not achievable through conventional carburizing because the high treatment temperature leads to carbide formation; thus low temperature carburization can achieve a greater surface hardness than conventional carburizing for austenitic stainless steels. The formation of chromium carbides in stainless steels deteriorates the

corrosion resistance of the alloy by depleting the matrix of chromium which is essential to the formation of the corrosion resistant passive oxide film. Thus, preventing the formation of these precipitates is advantageous to preserving the corrosion resistance of the treated material. This concept and its relation to the low temperature carburization process can be illustrated with the Time-Temperature-Transformation (TTT) diagram for the austenitic stainless steel alloy 316 (Fig. 1) (5). As shown in the TTT diagram, the Swagelok low temperature carburization process operating temperature is below the formation temperature for carbides.

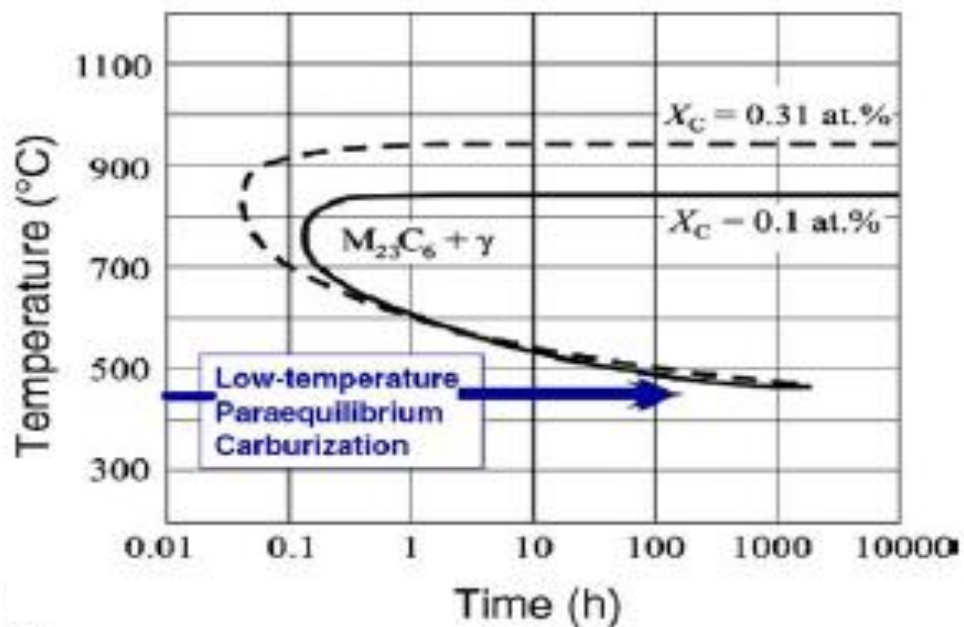


Figure 1 TTT Diagram for 316 Stainless Steel with two different carbon levels (from (5) Michal et al, Acta Materialia, 2004)

The patented Swagelok low temperature carburization process is composed of several steps, an example of which is shown in Figure 2. First, the passive film of the target materials is removed by an activation step which exposes the stainless steel to dry HCl-containing gas at $\approx 250^\circ\text{C}$ for a time of approximately two hours. Following the

first activation step, the temperature of the process chamber is increased and an initial carburization step ensues for approximately two hours within a carbon rich gas atmosphere. Following this brief initial carburization step, a second activation step takes place to ensure that the passive film has been entirely removed along with any surface contamination. After the second and final activation step, the primary carburization step begins at a specified treatment temperature in a carbon-rich gas environment, and continues for an extended period of time, often twenty hours or longer. The exact treatment temperature is dependent on the specific alloy being treated and is typically around 450°C for austenitic stainless steels. During carburization, the gas environment within the chamber maintains a very high carbon activity which creates a high chemical potential gradient from the process atmosphere to the core of the material being treated. This chemical potential gradient is the key driving force promoting diffusion of carbon from the process atmosphere into the target material's surface. As shown by **Figure 2**, the carbon activity of the treatment environment is slowly reduced from a very high initial level to less than 1.0 during the treatment cycle; this is done to initially boost the diffusion of carbon and then to prevent sooting. (13-16)

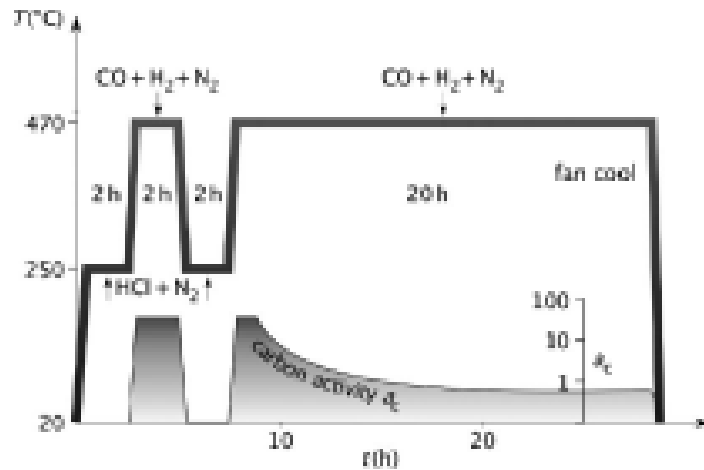


Figure 2 Swagelok Low Temperature Carburization Process Diagram, an example process (From (6), F. Martin, Electrochemical and Solid-State Letters, 2007)

A typical carbon concentration and hardness depth profile within the case hardened layer of low temperature carburized 316L is shown in **Figure 3**. As shown by **Figure 3**, the case hardened layer extends roughly 25 μm below the surface of the treated material, has a maximum hardness of ≈ 1200 HV near the surface which decreases to around 250-300 HV in the core of the material, which is equal to the hardness of non-treated 316L material. Due to the high supersaturation of carbon within interstitial sites of the austenite matrix, an expansion of the austenite lattice occurs within the hardened layer and has been observed experimentally (5). The degree of lattice expansion is directly related to the amount of carbon that is in solution within the matrix. A maximum lattice expansion of $\approx 3\%$ has been observed at the surface of 316L stainless steel and corresponds to a carbon concentration of ≈ 12 at%. Because the austenite matrix of the case hardened layer undergoes a lattice expansion while constrained by the non-treated core (which does not undergo lattice expansion), bi-axial compressive stresses develop within the case. A typical relationship between the

residual compressive stresses within the case, the carbon concentration, and the depth from the surface of treated 316L is shown in **Figure 3** (5).

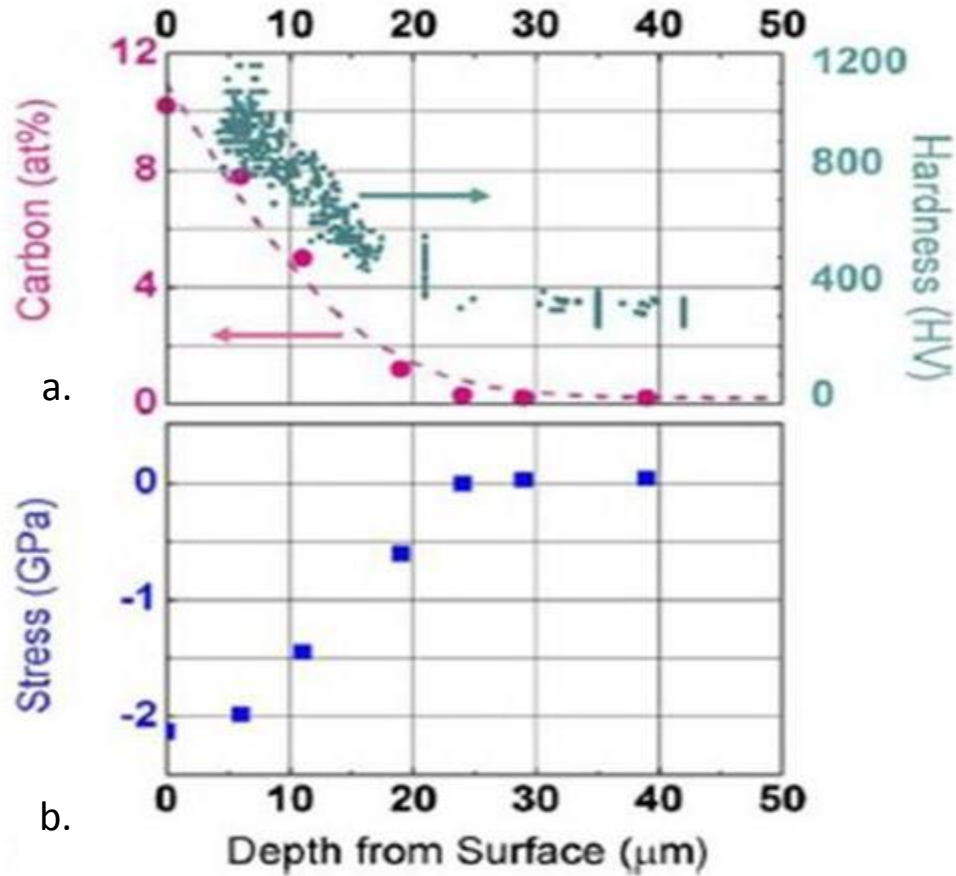


Figure 3 (a.) Carbon Concentration & Hardness Depth Profiles, and (b.) Residual Stress Depth Profile (from (5), Michal et al, Acta Materialia, 2004)

2.0 Tribology Review

The field of tribology is defined as the science of the mechanisms of friction, lubrication, and wear of contacting surfaces that are in relative motion, as set forth by The Organization for Economic Cooperation and Development in 1967 (7). Tribology has been studied for over three centuries and is an interdisciplinary field in which physicists, chemists, mechanical engineers, and materials scientists all partake. Its importance and

economic impact on society is evident in the fact that the majority of failures in machines containing moving parts such as gears, bearings, couplings, seals, cams, clutches, and valves, is a result of relative motion between contacting surfaces (7). This project primarily focuses on the materials science aspects of the improvement in stainless steel wear resistance achieved with the Swagelok Co. low temperature carburization process. **Table 1**, from Stochowiak (7), shows a generalized guide to materials selection for tribological applications. As shown by **Table 1**, increasing the hardness of a material is likely to improve resistance to abrasive, erosive, and adhesive wear. Furthermore, improvements in fatigue resistance are expected to reduce wear by abrasion, erosion, cavitation, fretting, and fatigue-wear mechanisms. Thus the low temperature carburization process should positively impact the wear behavior of stainless steels through the extreme increase in hardness as well as the resulting improvement in fatigue life.

Critical materials property	Wear mechanism							
	Abrasive	Erosive	Cavitation	Corrosive	Fretting	Adhesive	Melting	Fatigue
Hardness	✓	✓	○	○	○	✓	○	○
Toughness	○	✓	✓	○	○	○	○	✓
Fatigue resistance	✓	✓	✓	○	✓	○	○	✓
Inertness	○	○	○	✓	✓ ^①	○	○	○
High melting point	○	○	○	○	○	✓	✓	○
Heterogeneous microstructure	✓	○	○	✗ ^②	○	✓	○	○
Non-metallic character	○	○	○	✓	○	✓	○	○

- ✓ Important
- Marginal
- ✗ Unfavourable

- ① Fretting in air for metals
- ② Homogeneous microstructure inhibits electrochemical corrosion and, with it, most forms of corrosive wear

Table 1 General materials selection chart for tribological applications (from (7), G. Stochowiak, *Engineering Tribology*, 2005)

Before proceeding to the experimental work of this study, it is important to review the basic principles of tribology, friction, and wear. These are discussed in the following sections, including friction and frictional heating, contact mechanics of sliding surfaces, and general wear mechanisms.

2.1 Contact of Real Surfaces

Real surfaces are not perfectly flat and contain some amount of topography. Many common engineering surfaces contain a significant amount of surface roughness, and typically contain a distribution of many peaks and valleys. These peaks of surface roughness are commonly referred to as asperities. When two real surfaces come into contact, these asperities directly contact each other while the surface valleys remain apart. Asperity dimensions range widely in size depending on the topography of the surface. In general, the asperity size is much smaller than the apparent area of contact.

Because of this, the contacting force is distributed amongst the individual contacting asperity areas, which are relatively small. This generally results in the plastic deformation of asperities to accommodate the contact force. **Figure 4**, from Bhushan (8), illustrates the concept of real surfaces in contact. This concept plays a vital role in the friction and wear behavior of materials.

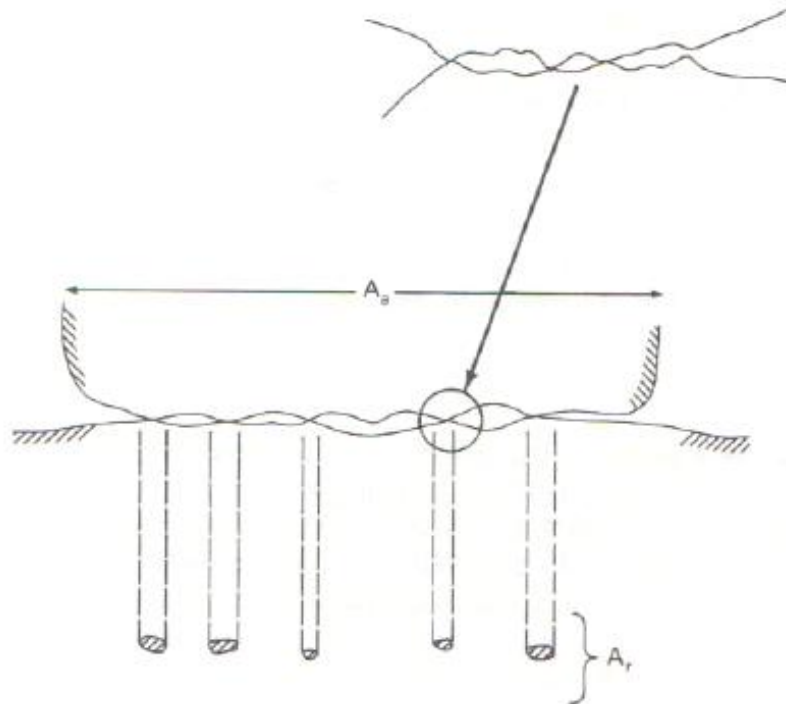


Figure 4 Real area of contact between two surfaces, inset illustrates contact between asperities (from B. Bhushan, Principles and Applications of Tribology, 1999 (8)). A_a refers to the apparent area of contact and A_r refers to the real area of contact. The inset is a magnified view of the micro-contact.

2.2 Friction and Frictional Heating

Frictional theory has been studied for centuries, dating more than 500 years ago, to Leonardo da Vinci (8). The relationship between friction and wear seems intuitively obvious, however the details of this relationship can be quite complex. When two contacting surfaces slide against each other, a frictional force is generated opposite to

the direction of sliding. The Coefficient of Friction is defined as the ratio of this frictional force to the applied normal force at the interface of the two sliding surfaces, as described by Amontons' law which was developed in 1699 (8). In the 1930's, and through the 1970's, Bowden and Tabor of Cambridge University developed a widely accepted theory of friction that accounts for the energy loss caused by friction. The Bowden and Tabor model explains that friction is made of two components, 1.) energy losses due to adhesion (discussed further in **section 2.4.2**), and 2.) energy losses due to deformation. Since the models' conception, it has been proven that these two components are not completely independent of each other, although conceptually it can be beneficial to think of them as separate processes (**Fig 5**), (9).

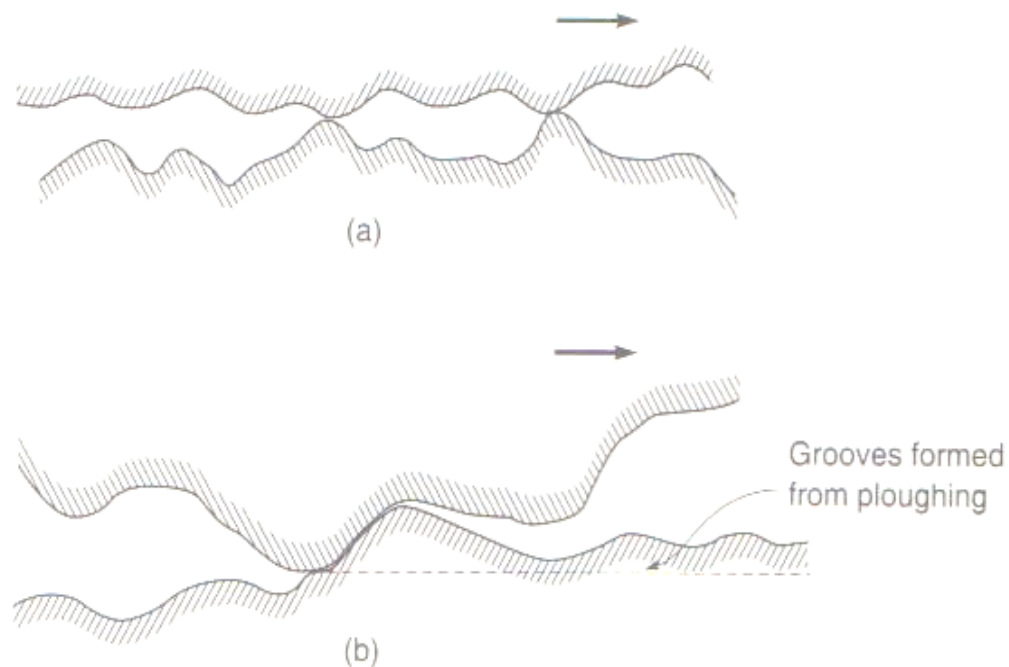


Figure 5 Plastic deformation component of friction, (a) asperity contact during sliding, and (b) micro view of asperity during sliding and deformation induced by the harder surface (8) from Bhushan, Principles and Applications of Tribology, 1999)

During sliding, nearly all of the work that is done against friction is transformed to heat at the interface of the sliding surfaces (10). Both the geometry and the material properties of the contacting surfaces determine the fraction of heat that flows into the two respective surfaces. This generation of frictional heat at the sliding interface can alter the local material properties of the sliding surfaces and, in turn, influence the coefficient of friction, wear rate, and dominant mechanisms of wear (8).

When two imperfectly smooth surfaces come into contact, the peaks of each “rough” surface form contacting asperity junctions, and the valleys of each surface may not contact each other. During sliding, both the size of these asperities, and the time in which they contact significantly influence the local increase in temperature due to friction. The time in which these asperities are in contact depends on both the size of the asperity junction, typically nanometers to several microns in diameter, and the relative sliding velocity of the interface, and can commonly range from nanoseconds to microseconds (8). If the normal load is sufficiently high, the real contact area (A_r) becomes equal to the apparent contact area (A_a) due to asperity deformation, and frictional heating occurs throughout this contact. This concept is illustrated in **Figure 6**.

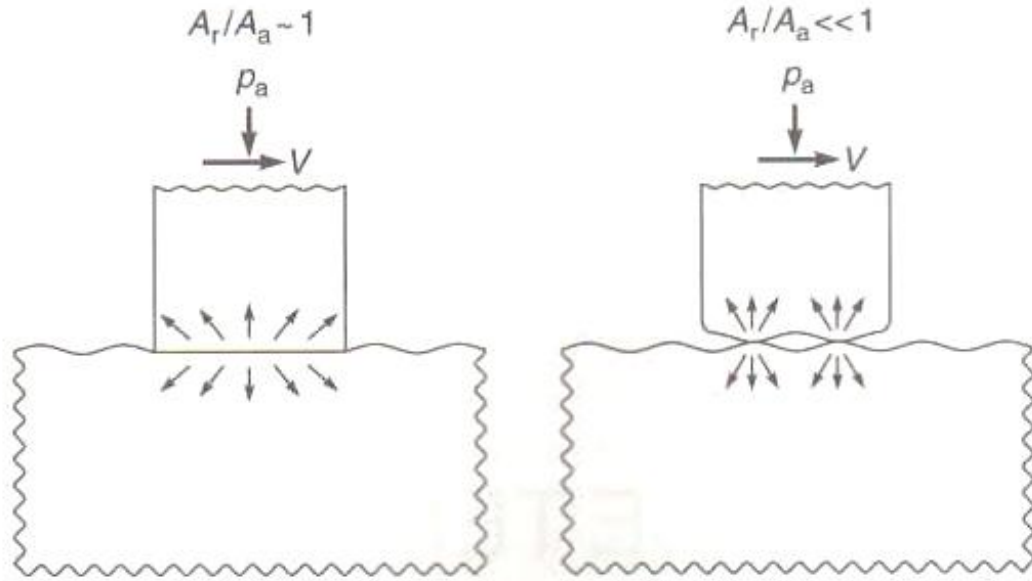


Figure 6 Frictional heating under low load when real area of contact is less than the apparent area of contact, and under high load when A_r and A_a are equal (from (8), Bhushan, Principles and Applications of Tribology, 1999).

Attempts to theoretically estimate the rise in temperature due to frictional heating have been made for more than 100 years. In 1991, an influential paper titled “Temperature Maps for Frictional Heating in Dry Sliding” was published in the Journal of Tribology Transactions by Ashby (10). Ashby applied known heat transfer models describing frictional heating in dry sliding, initially developed by Jaeger, and modified them specifically for the pin-on-disk test which is heavily utilized in wear and tribology research. The bulk temperature due to frictional heating can be estimated using the following equations derived by Ashby; here T_b is the bulk surface temperature assuming that frictional heat is uniformly injected into the sliding surface, T_0 is the temperature of the heat sink (often room temperature), k_1 and k_2 are the thermal conductivity of surface one and two respectively, μ is the coefficient of friction, l_{1b} and l_{2b} are the equivalent linear heat diffusion distances from the interface of materials one and two respectively to their respective heat sinks (typically taken as their fixtures) (Fig. 7), F is

the applied load, v is the sliding velocity, and A_n is the nominal or apparent contact area.

Equation 1
$$T_b = \frac{\mu F v}{A_n} \left(\frac{1}{\frac{k_1}{l_{1b}} + \frac{k_2}{l_{2b}}} \right) + T_0$$

Equation 2
$$T_f = \frac{\mu F v}{A_n} \left(\frac{1}{\frac{k_1}{l_{1b}} + \frac{k_2}{l_{2b}}} \right) + T'_b$$

Equation 3
$$T'_b = T_b - \frac{A_r}{A_n} (T_b - T_0)$$

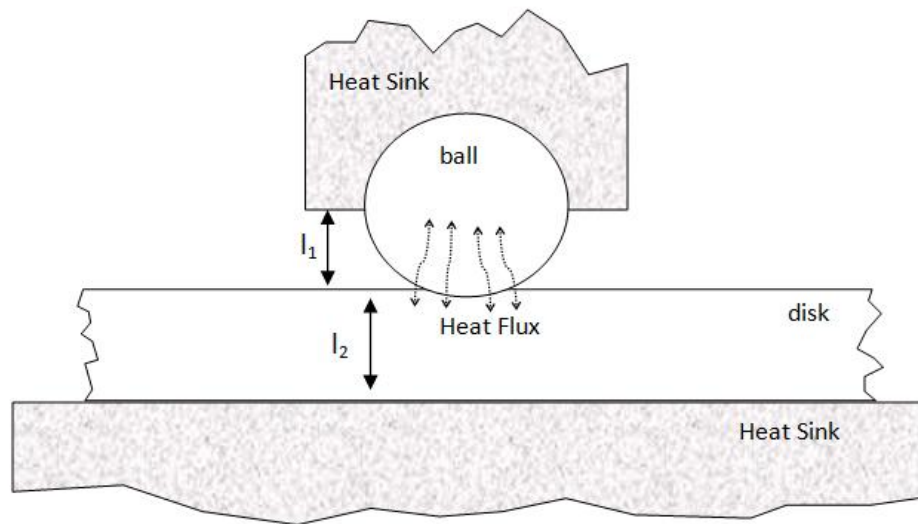


Figure 7 Schematic of the pin-on-disk test as it relates to frictional heating Equations 1-3 (Adapted from similar schematic, Ashby et al, Tribology Transaction, 1991 (20)).

These equations are rarely used to directly obtain accurate flash temperature predictions without the support of experimental bulk temperature data. This is mainly because the heat diffusion distances (l_{1b} and l_{2b}) in Equation 1 and Equation 2 are rarely equal to the physical distance measured for the experimental setup (l_1 and l_2 in **Fig. 7**). Factors such as the shape and efficiency of contact between material and fixture, radiation heat loss, and convection heat loss can all significantly affect the linear equivalent heat diffusion distance. Thus typically the bulk temperature of a disk under

various sliding conditions is measured and used to correct for these influences. Another source of potential error in these calculations is the calculated real area of contact, which can be affected by surface roughness, surface hardness, frictional heating, and other factors.

2.3 Contact Mechanics

Hertz was the first known scientist to investigate and advance the understanding of contact mechanics. In 1980, K.L. Johnson of Cambridge University assembled the renowned book “Contact Mechanics”. Johnson’s work focused on linking the science of contact mechanics to the many engineering interests in the field, including sliding of surfaces with frictional considerations. In order to fully understand the difference in wear behavior of low temperature carburized stainless steels and standard non-treated stainless steels, an understanding of the mechanics involved with fundamental wear processes is helpful, and is discussed in the following sections.

2.3.1 Static Contact Mechanics

When two surfaces come into contact, elastic and plastic deformation occurs at their interface. When a perfectly elastic, perfectly smooth sphere comes into contact with a perfectly elastic, perfectly smooth flat plane, a circular contact area results at the interface. The stress distribution within the contacting interface is not uniform. The maximum compressive stress is located at the center of the circular interface, and the perimeter is in a state of pure shear, due to the hoop stress and radial stress being of equal and opposite magnitude. A schematic of the surface stresses due to Hertzian loading of a sphere on flat is shown in **Figure 8**. (11)

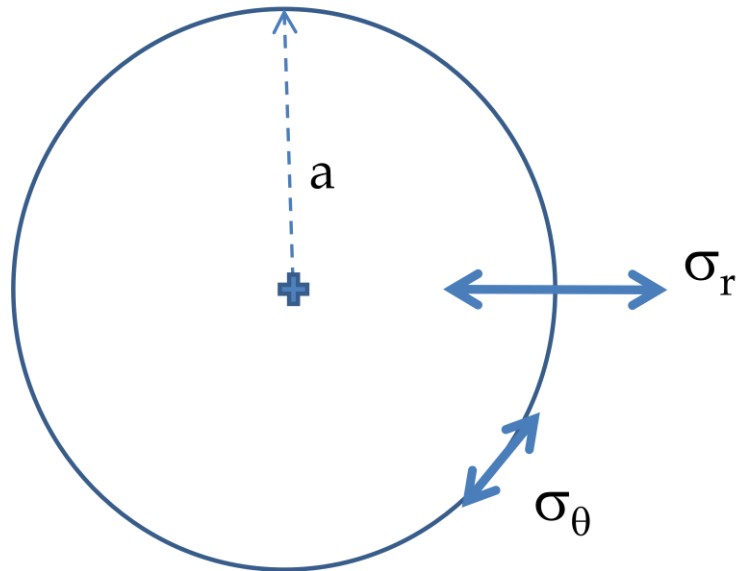


Figure 8 Hertzian contact area for a sphere on flat where a is the radius of contact, σ_r is the radial stress, and σ_θ is the hoop stress

The distributions of stresses beneath the circular contacting interface are also of interest, the most important of which is the shear stress distribution. The maximum shear stress under static normal load is located beneath the center of the contact area at a distance of $0.48a$, where a is the radius of the apparent contact area at the interface (for contact of sphere on flat only). The location of the maximum shear stress is of importance because it corresponds to the location of first yield within the material, and this remains true once friction is introduced to the system. If the maximum shear stress exceeds the shear strength of the material, then yielding will occur at this point.

(11)

The maximum Hertzian contact stress, maximum shear stress, and depth of the max shear stress can be calculated using **Equations 4-9**; here E is the elastic modulus, E^* is the relative elastic modulus, ν is Poisson's ratio, $R_\#$ is the radius of the respective contacting material, R is the relative radius, a is the radius of the circular contact area, P

is the applied load, τ_1 is the maximum shear stress, z is the depth of τ_1 beneath the contacting interface, and P_0 is the maximum Hertzian contact stress (11). These equations assume smooth surfaces so that the real area of contact is equal to the apparent area of contact.

Equation 4 $a = \text{radius of contact area} = \left(\frac{3PR}{4E^*}\right)^{1/2}$

Equation 5 $P_0 = \text{Max Hertz Contact Stress} = \left(\frac{3P}{2\pi a^2}\right) = \left(\frac{6PE^{*2}}{\pi^3 R^2}\right)^{1/3}$

Equation 6 $\tau_1 = \text{Max Shear Stress} = 0.31P_0$

Equation 7 $z = \text{depth of max shear stress} = 0.48a$

Equation 8 $R \equiv \left(\frac{1}{R_1} + \frac{1}{R_2}\right)^{-1} = \text{relative radius of contacting materials}$

Equation 9 $E^* \equiv \left(\frac{1-\nu_1^2}{R_1} + \frac{1-\nu_2^2}{R_2}\right)^{-1} = \text{relative modulus of materials}$

2.3.2 Contact Mechanics of Sliding Surfaces

When two contacting surfaces slide against each other, friction is introduced to the system. During simple sliding, the friction force, or traction force is considered to be exerted in a direction perpendicular to the applied load and parallel to the direction of sliding. As friction increases, the location of the maximum shear stress moves closer to the sliding interface. According to the Von Mises Yield Criterion (11), once the coefficient of friction becomes equal to or greater than 0.3, the maximum shear stress will be located at the interfacial plane of the sliding surfaces, and this will be the location of first plastic yield. This shear stress can be estimated by **Equation 10**, as described by Johnson (11); here μ is the coefficient of friction, and P_0 is the maximum

Hertzian contact stress under static conditions. If τ_1 is greater than the shear strength of the sliding material, then yielding will occur resulting in plastic deformation related wear.

Equation 10

$$\tau_1 = \mu P_0$$

2.3.3 Contact Mechanics and Low Temperature Carburized Materials

The yield stress of stainless steel hardened by the Swagelok Co. low temperature carburization process can be approximated using indentation microhardness. Vickers microhardness is related to the yield stress of a material through the approximation shown in **Equation 11**; here h is the indentation hardness, n is the strain hardening coefficient, and σ_{yield} is the approximated yield strength. (12)

Equation 11

$$\sigma_{yield} = \frac{h}{3} (0.1)^n$$

According to **Equation 11**, low temperature carburized stainless steel achieving a surface hardness of 12 GPa will have a yield strength at the surface of approximately 2.3 GPa, which was discussed by Michal et al (5). This is much greater than the yield strength of non-treated 316L; approximately 200-300 MPa.

An increase in yield strength due to surface hardening will also correspond to an increase in shear strength. The shear strength, or yield stress when in a stress state of pure shear, is related to yield strength through **Equation 12**; here k is the shear strength (11).

Equation 12

$$k = \frac{\sigma_{yield}}{\sqrt{3}}$$

According to **Equation 12**, the shear strength of 316L stainless steel will be increased from approximately 115 MPa to 1.3 GPa. The greatly improved strength in pure shear suggests that low temperature carburized stainless steels will exhibit much less plastic deformation than non-treated stainless steel when subjected to tractional forces which create a pure shear stress state at the sliding interface. From this perspective, a drastic improvement in wear resistance can be expected after carburizing due to increased shear strength and the resulting reduction in plastic deformation which is a major component of many wear mechanisms (9).

2.4 Sliding Wear of Metallic Materials

2.4.1 Simple Theory of Sliding Wear, Archard's Wear Equation

Archard and Hold proposed a simplistic theoretical analysis describing wear due to the sliding of two surfaces in contact. When two surfaces in contact are sliding, at least one of the surfaces will experience wear. Archard's theory of wear relates the volume of material lost by wear to the total distance of sliding, the applied load, the contacting area, and the hardness of the softer material of the contacting/sliding pair. The theory is derived from models of sliding contact and the nature of the contacting interface, and is shown by **Equation 13**; here Q is the material volume worn away per unit sliding distance (mm^3/m), K is a constant called the Archard wear coefficient, W is the normal load applied to the contacting interface (N), and H is the hardness of the softer material (Pa). A derivation of this equation is discussed by Hutchings. (19)

The Archard Wear Equation states that the volume of material worn away is directly proportional to the applied normal load and total sliding distance of the contacting surfaces. While in most cases wear is directly proportional to the total sliding distance, it often is not directly proportional to the applied normal load. For most metallic materials, the total volume of material worn away will behave as described by the Archard wear equation over a certain range of loads, but sharp transitions in wear rate will occur once a certain load is reached. This abrupt transition in wear rate is not accurately described by the Archard wear equation, and several models of greater complexity have been developed in attempts to obtain a more complete theoretical model of sliding wear that considers the multitude of possible wear mechanisms. (19)

2.4.2 Adhesive Wear

When two solid materials that are completely free of surface contamination come into contact within an ultra high vacuum environment, adhesion at their interface will occur. Often, the adhesive force between two contacting surfaces under UHV will be greater than the contact force. Contaminants such as passive films, oxidation, lubricants, and adsorbed gases reduce the adhesion of two surfaces by providing a barrier that decreases the amount of real contact area. The mechanism by which two intimately contacting surfaces adhere to each other is through electron transfer, which results in the formation of adhesive bonds (7). **Figure 9** illustrates the basic concept of adhesion and transfer due to material contact.

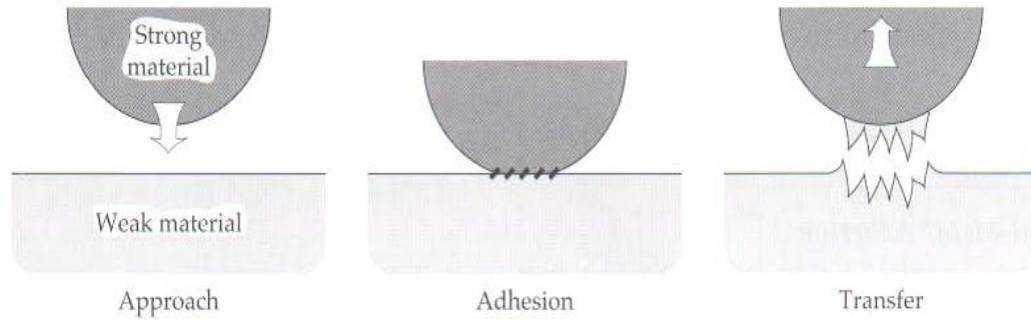


Figure 9 Contact, adhesion, and transfer due to electron transfer and adhesive bond formation, typically the softer or weaker material is transferred to the stronger material (from (7), Stochowiak, *Engineering Tribology* 3rd ed, 2005).

The adhesion force observed for identical homogeneous ductile materials is typically greater than that of heterogeneous materials and brittle materials such as ceramics. While adhesion between contacting ceramics can occur, the real area of contact is limited because of the high yield stress of these materials. When two ductile materials, such as face centered cubic iron-base alloys, come into contact, asperities experience plastic deformation and increase the real contact area available to form adhesive bonds. Metallic materials with a low number of slip systems, such as hexagonally close packed metals, generally show less adhesion than cubic metals. Heterogeneous materials such as carbide rich tool steels are known to exhibit less adhesion than homogeneous metallic materials because the dual phase structure reduces contact of chemically identical surfaces. Adhesion between ceramic and metallic materials may also occur, particularly for oxygen-rich ceramics such as alumina. Adhesive bonding between the oxygen atoms in the alumina lattice may occur with contacting metallic surfaces which usually results in transfer of the metallic material to the ceramic interface (7).

Adhesion has long been known to play an important role in tribology. Tabor and Bowden of Cambridge University initially proposed friction theories which relied on the adhesive contact of solid materials in the 1930's. Their general theory which was developed through the 1970's, suggested that the total friction force experienced by sliding surfaces consists of two independent components; 1.) friction due to adhesion, and 2.) friction due to deformation. It was later proven that these two components are not completely independent of each other; however, examining them both separately is beneficial when illustrating the relationship between wear and friction.

Adhesive wear is thought to take place by the following general mechanism. First, sliding commences and friction is relatively low due to surface contamination. Friction increases in proportion to the rate at which the surface contamination is removed from the sliding interface. Once surface contamination is completely removed, adhesion of contacting asperities will occur, resulting in a high friction force, provided that no tribochemical oxidation (discussed in next section) occurs. Following adhesive contact, fracture of the weaker material and transfer to the stronger material may occur. This results in the formation of a transfer layer or film. When adhesion of sliding asperities occurs, fracture and transfer film formation is not the only possible mechanism by which wear occurs. As shown by **Figure 10**, asperity fracture following adhesion may occur by brittle fracture of the weaker asperity, or strain to failure.

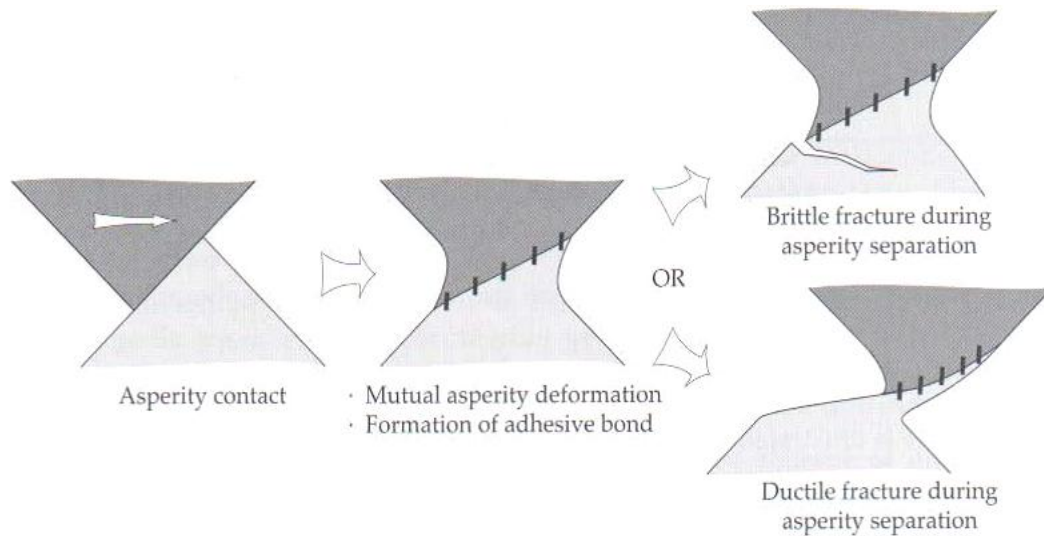


Figure 10 Alternative models for the production of wear debris and deformation by adhesive contact of asperities (from (7), Stochowiak Engineering Tribology 3rd ed., 2005).

Plate-like wear debris particles may also form as a result of adhesive wear. As shown by **Figure 11**, successive adhesion and transfer may result in a relatively round debris particle that are composed of material from both sliding surfaces. If this particle continues to grow, it will likely become flattened by plastic deformation as it is sandwiched between the sliding surfaces. Adhesive processes will continue to grow the transfer particle until it reaches a critical thickness and detaches. Flake-like wear debris may also be produced from other mechanisms which are discussed in following sections.

(7)

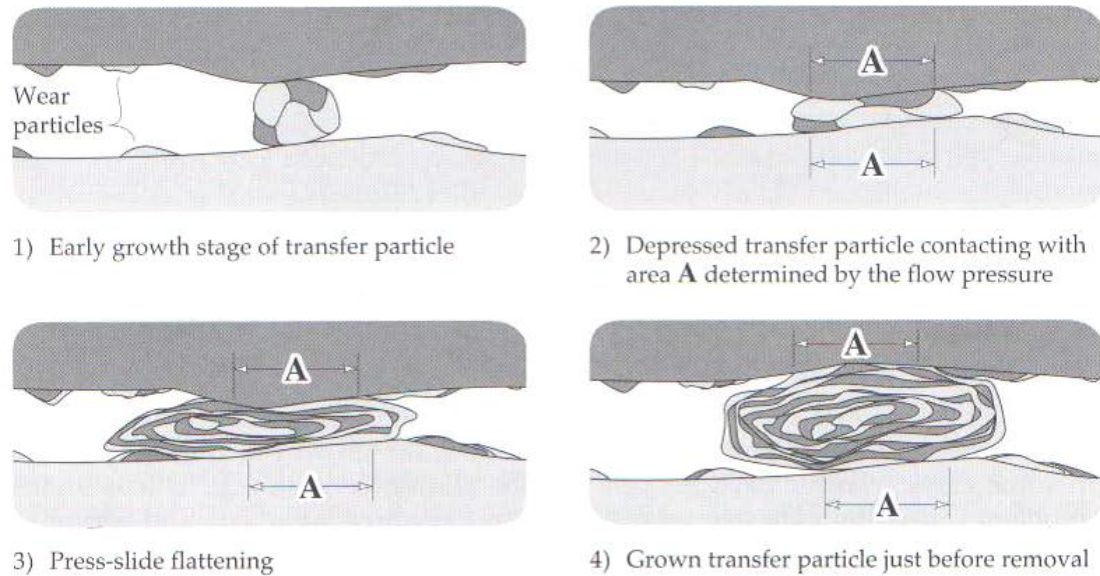


Figure 11 Possible mechanism of wear debris formation due to adhesive transfer (from (7), Stochowiak Engineering Tribology 3rd ed., 2005)

2.4.3 Oxidative Wear

Oxidative wear, as implied by its designation, is dependent on the formation of a tribochemically induced oxide film on the sliding metallic surface. For this to occur, an environment which enables oxidation of metallic surfaces (ex: air), and a sufficient driving force must be present. When an oxide film of sufficient thickness forms, direct contact of the sliding surfaces is reduced or eliminated and the shear strength of the interface is effectively reduced by mitigating adhesive forces. Under dry sliding conditions the maximum applied shear stress is located at the interface of the sliding material; thus the reduced interfacial shear strength provided by the oxide layer limits subsurface deformation and strain accumulation, consequently reducing wear.

Similar to static thermal oxidation, oxidative wear is a thermally driven process. The rate of oxide film growth can be modeled by an Arrhenius relationship as shown by

Equation 14; here k is the parabolic rate constant for tribochemically induced oxide film growth, Q is the activation energy, R is the universal gas constant, and T is the interface temperature (9).

Equation 14

$$k = A \exp(-Q/RT)$$

As described by this model, anything that will effectively increase the interfacial temperature will result in an increased rate of oxide film growth. Thus, the rate of oxide film growth can be increased by elevated frictional heating and/or increased ambient environment temperature. While tribochemical oxidation is similar to thermal oxidation, it occurs at a much faster rate. This is due to the difference in material properties affecting diffusion near the surface under sliding conditions, which are altered by defects, stress, and deformation, which may accelerate oxide growth. An illustration of oxidative wear is shown in **Figure 12**. (7)

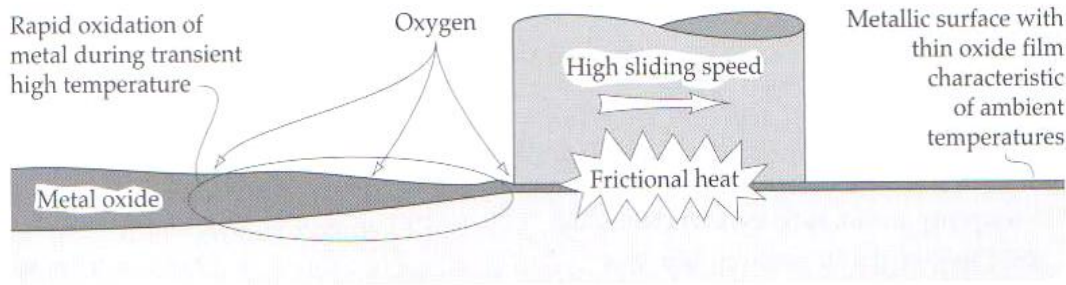


Figure 12 General principal of oxidative wear (from (7), Stochowiak Engineering Tribology 3rd ed., 2005).

Oxidative wear can occur at high speeds when a high level of frictional heating occurs, and also at low sliding speeds when the contacting force is sufficiently low. Under these two regimes, oxidative wear occurs by slightly different mechanisms. During oxidative wear at high sliding speeds, an initial period of severe wear occurs eliminating the native oxide film. This is followed by a period of mild wear and re-

growth of the oxide layer. At high sliding speeds, frictional heating is so high that thick oxide films are rapidly generated. Because only sliding surface asperities (not the entire surface) experience this frictional heating, oxide grows preferentially at contacting asperities. Once the oxide reaches a critical thickness it can no longer support the frictional shear stresses or applied load and spalls off. At sufficiently high sliding speeds, oxidative wear can become detrimental if significant material loss occurs through the repetitive growth and removal of oxide layers. **Figure 13** shows an example of oxidative wear at high sliding speeds. (7)

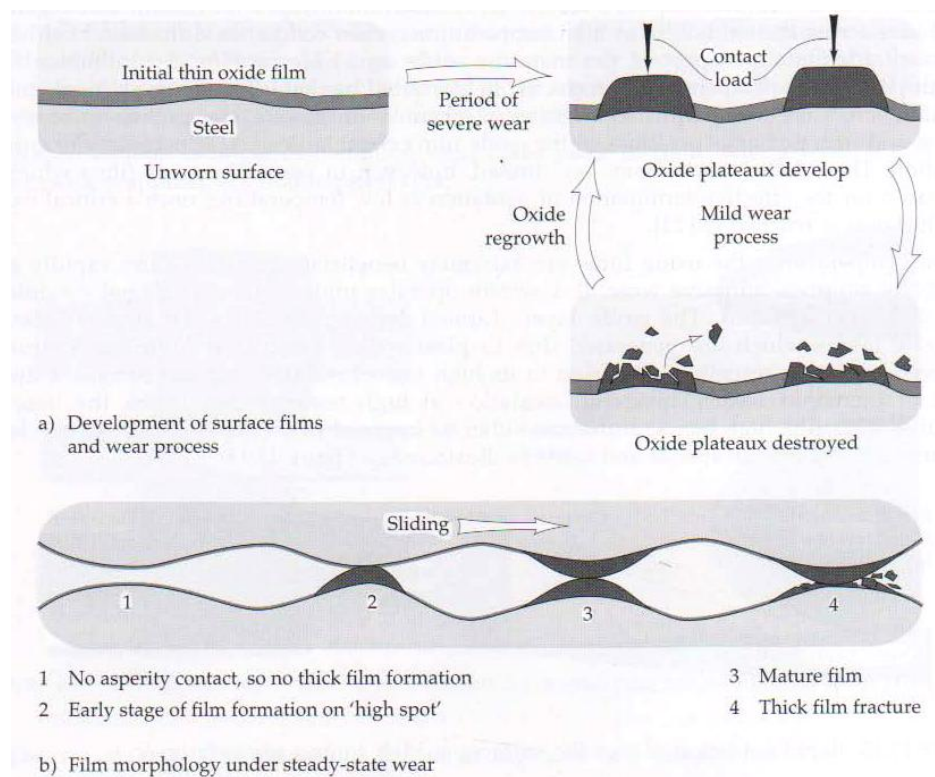


Figure 13 Proposed mechanism of oxidative wear at high speeds (from (7) Stochowiak Engineering Tribology 3rd ed., 2005).

Under low sliding speeds, oxidative wear occurs by a different mechanism. Because frictional heating is not sufficiently high, a thin oxide film forms on the sliding surfaces and its growth is limited by slow diffusion. As the thin oxide film fractures and

metallic wear debris become oxidized while tumbling between the sliding contacts, a compact layer of mixed wear debris forms. This layer is formed by a mixture of oxide debris and oxidized metallic debris, and often results in a reduction in both friction and wear. **Figure 14** illustrates a mechanism of oxidative wear at low sliding speeds, as described by Stochowiak. (7)

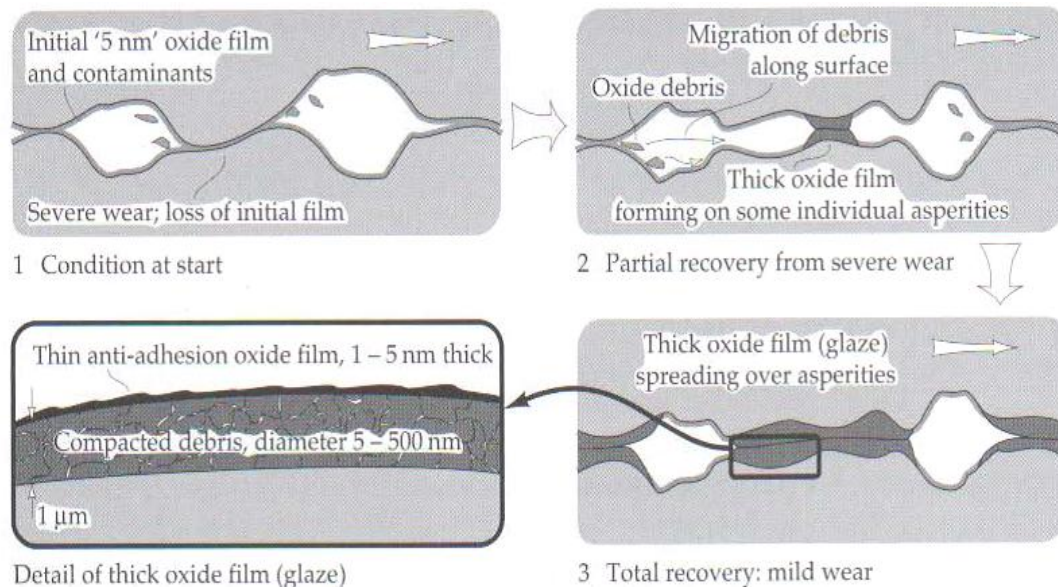


Figure 14 Proposed mechanism of oxidative wear at low sliding speeds (from (7), Stochowiak Engineering Tribology 3rd ed., 2005).

2.4.4 Fatigue Wear and Delamination

Fatigue wear is caused by cyclic contact stresses. During sliding, this results in cyclic crack growth and failure of regions near the surface. There are several theories describing the details by which this process occurs during sliding of metals, delamination wear is perhaps the most recognized. The original theory of delamination wear was proposed and extensively investigated by NP Suh's research group at the Massachusetts Institute of Technology in the 1970's. The model proposed that sub-surface crack

initiation, propagation, and crack linkage resulted in the spallation of flake-like debris from the surface of sliding contacts. Since the conception of this theory, several attempts to model wear of materials based on delamination have been made. Johnson of Cambridge University, and others, applied linear elastic fracture mechanics (LEFM) to model crack growth due to delamination wear. These models made important advances to the understanding of this process; however the use of LEFM for delamination wear is invalid because 1.) crack growth due to tribological contact stresses occurs within a region that has undergone significant plastic deformation, 2.) LEFM predicts crack growth in Mode II and experimental observation has proven that crack growth due to tribological contact stresses occurs in Mode I, and 3.) LEFM does not account for crack initiation. (13)

A delamination wear model that accounts for Mode I crack growth within a heavily deformed plastic region was proposed by Kapoor of the University of Sheffield in 2000. This model proposes that delamination wear is a competitive fracture process between two mechanisms, low cycle fatigue (LCF) and ratcheting failure (RF). LCF is the process by which cyclic crack growth is drastically shortened due to high amounts of plastic deformation, high stress amplitudes, and high stress concentrations. LCF can be described by **Equation 15**, the Coffin-Manson relationship (14); here, $\frac{\Delta\epsilon_p}{2}$ is the plastic strain amplitude, ϵ'_f is the fatigue ductility coefficient, $2N_f$ is the number of load reversals to failure, and c is the fatigue ductility exponent.

Equation 15

$$\frac{\Delta\epsilon_p}{2} = \epsilon'_f (2N_f)^c$$

RF is the process by which strain accumulation due to plastic deformation resulting from cyclic stresses grows until a critical threshold is reached. Once the strain accumulation threshold is reached, ductile failure occurs by exceeding the strain to failure limit.

Under the framework of Kapoor's delamination wear theory, the LCF and RF processes occur independently of each other. Thus each process occurs simultaneously under tribological contact until the critical level of crack growth or strain accumulation is reached, causing fracture of the surface region.

Kapoor proposed a convenient way to describe this process which considers the surface region of the sliding or rolling contact to be comprised of layers. Strain accumulation occurs in each layer during cyclic stressing if the applied shear stress exceeds the effective shear strength of the material within the layer, according to **Equation 16**; here $\Delta\gamma$ is the increment of shear strain due to the applied cyclical stress, τ_{zx} is the maximum applied shear stress at a given subsurface depth caused by sliding or rolling contact, k_{eff} is the effective yield stress of the tribolayer in pure shear which must account for the effects of work hardening and the other tribological phenomenon that alter material properties as discussed above.

Equation 16

$$\Delta\gamma = 0.00237 \left(\frac{\tau_{zx}}{k_{eff}} - 1 \right)$$

Once strain accumulation and/or crack growth reach a critical level, the layer of material closest to the surface will spall off due to delamination wear, exposing the next layer which becomes the new sliding surface. This process is cyclically repeated as the

surface layers delaminate, causing subsurface layers to move towards the surface.

Figure 15 illustrates the delamination wear process.

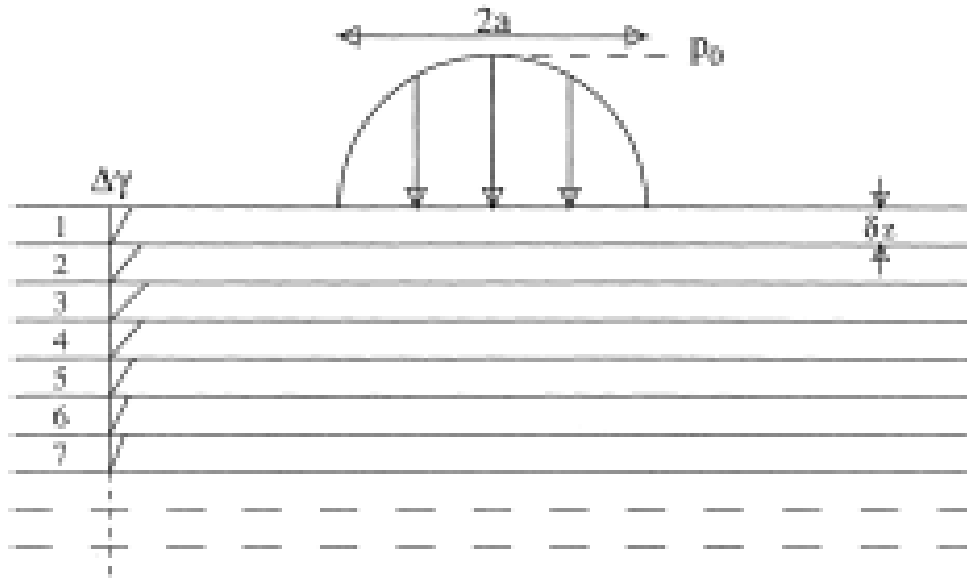


Figure 15 Layers of strain accumulation relevant to delamination wear. $\Delta\gamma$ is the strain accumulation increment as described by equation 16 above, δ_z is the thickness of each tribolayer, a is the radius of circular contact area for sliding or rolling contact of a sphere on a flat surface, and p_0 is the Hertzian contact pressure (from (13), Kapoor, Wear, 2000).

2.4.5 Abrasive Wear

The mechanism of abrasive wear is caused by the sliding or rolling of hard particles on the surface of a softer material. When moving in contact with the surface of a softer material, hard particles cause deformation and result in wear by several different mechanisms. Cutting, ploughing, grain pull out, fatigue, and brittle fracture may produce abrasive wear (**Fig. 16**).

During cutting, a hard particle is embedded in the softer material and dragged causing plastic deformation and material displacement around the particle's edges.

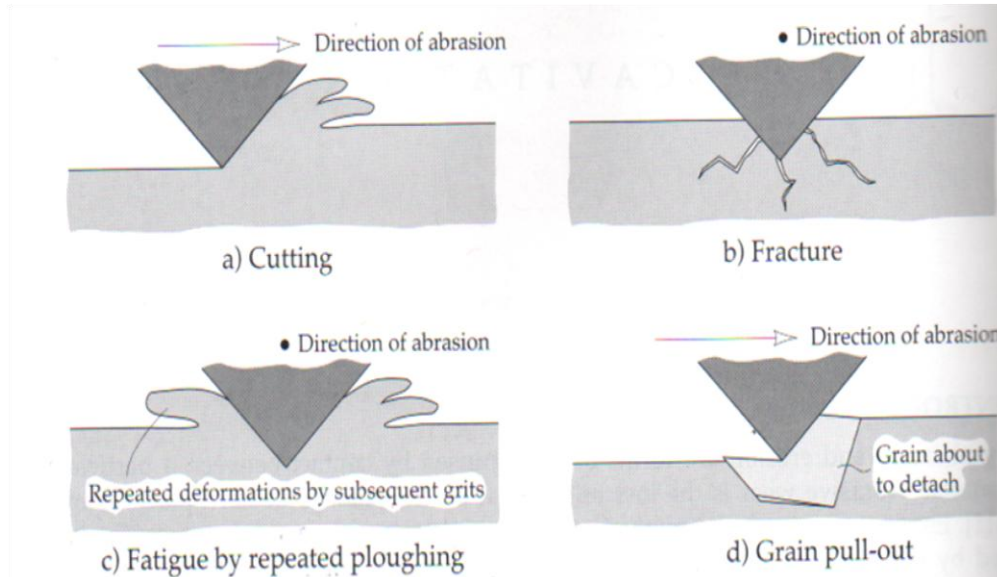


Figure 16 Four potential mechanisms of abrasive wear, (a.) cutting, (b.) fracture, (c.) fatigue, (d.) grain pull-out, from (7), Stochowiak, Engineering Tribology 3rd ed., 2005).

Ploughing by abrasive hard particles is similar, but plastic displacement of material occurs around the abrasives edges, while also building up in front of the particle. These mechanisms of wear are analogous to a snow shovel slicing through a pile of snow sideways (cutting), or pushing through a pile of snow in a direction perpendicular to the wide face of the shovel (ploughing). Grain pull out is a relatively rare form of wear that is most common in ceramics, but may occur in metallic materials if brittle phases form on grain boundaries.

Abrasive wear may occur by two-body or three-body abrasion. Two-body abrasion refers to hard grains that are fixed in a rigid mounting and are sliding against a softer material. Three-body abrasive wear refers to hard particles that are freely moving between two sliding surfaces (**Fig. 17**). During sliding of hard materials, particles of wear debris may be generated that result in three-body abrasive wear.

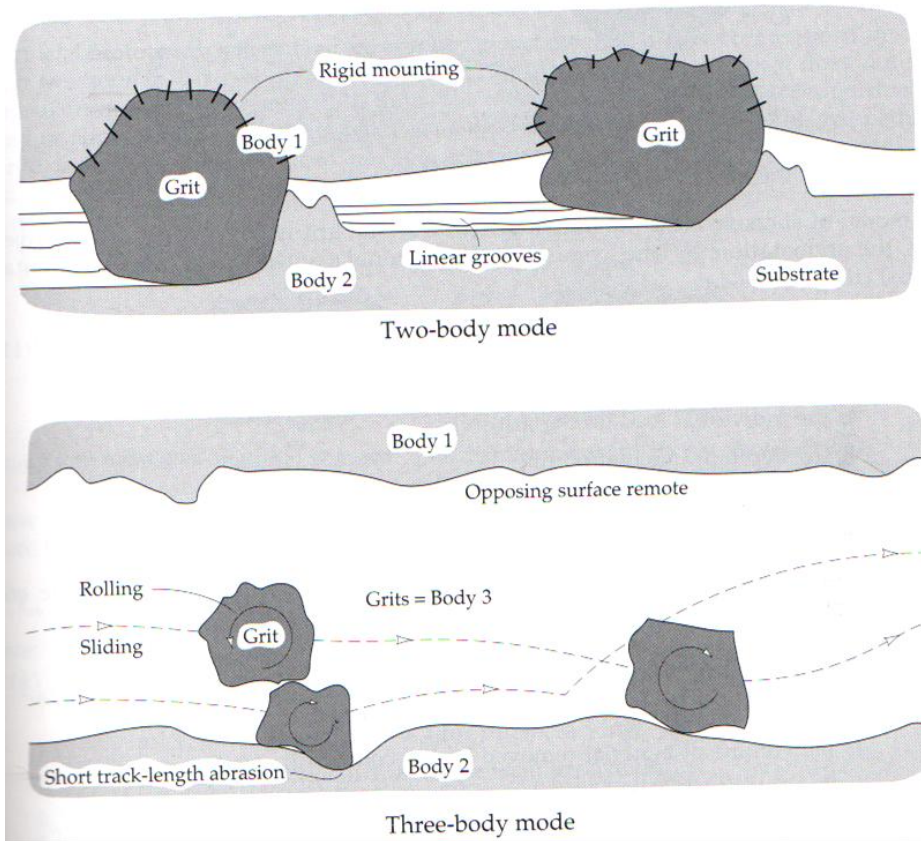


Figure 17 Two-body and Three-body abrasive wear (from (7), Stochowiak, *Engineering Tribology* 3rd ed., 2005).

2.5 Wear Regime Transitions and Wear Maps

The tribological performance of material pairs is heavily dependent on the contact conditions at the interface of the two sliding materials. The contact conditions determine the wear mechanisms that govern material removal from the sliding surfaces. Local changes in material properties, temperature, environment, stress, and real contact area can significantly alter the wear and friction behavior of material pairs.

The Archard Wear Theory predicts a proportional relationship between the wear of a material and the applied load. While this is the case for many materials under a range of contact conditions, it has been experimentally proven that sharp changes in

wear behavior can occur under small changes in load for many materials. An example of this for a brass pin sliding against a steel ring under non-lubricated conditions was described by Hutchings and is shown in **Figure 18 (9)**.

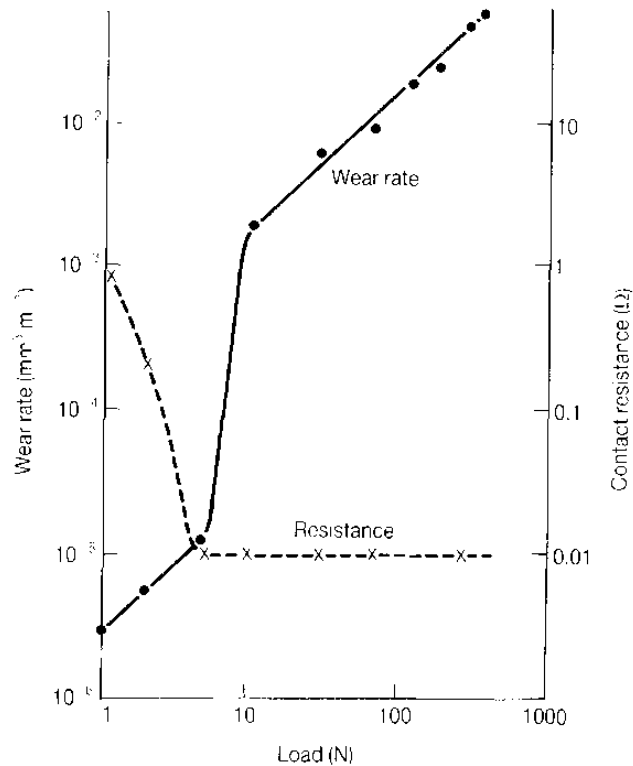


Figure 18 Wear regime transition for dry sliding of a brass pin against a stellite ring (from (15), Herst and Lancaster, *Journal of Applied Physics*, 1956).

As illustrated by **Figure 18**, a linear relationship between wear and load was observed at low applied loads. As the applied load approached 10 N, the wear rate increased by more than two orders of magnitude. This abrupt change can be explained by a change in the contact conditions at the sliding interface which results in a transition to more severe wear mechanisms. The change in contact condition is illustrated by the electrical contact resistance of the contacting materials as a function of applied load in **Figure 18**, here more electrical contact resistance corresponds to less contact at the interface.

Note that the sudden change in wear rate corresponds to a sharp decrease in electrical contact resistance between the sliding materials, indicating a high amount of directly contacting metal surface. (9)

Sudden transitions in friction and wear behavior can also be observed for many materials when the sliding speed of the material pair in contact is changed to a significant level. This is due to the influence of sliding speed on frictional heating and the temperature at the interface of the sliding materials. Changes in the interface temperature result in material property changes at the surface, thermal expansion or contraction, and changes in tribochemical reactions at the interface of the sliding material pair. When metallic materials are sliding in an oxygen-rich environment such as air, a significant increase in sliding speed often corresponds to significant drop in the wear rate due to an increased tribochemical oxidation rate. This results in the formation of a protective oxide film on the surface of the sliding materials. A further increase in sliding speed for cyclical sliding material pairs may lead to a sudden increase in wear rate due to the insufficient availability of time to form a protective oxide layer between sliding cycles, despite the increased sliding interface temperature. This concept was also described by Hutchings for brass sliding against steel in air and pure oxygen and is illustrated below by **Figure 19** (9).

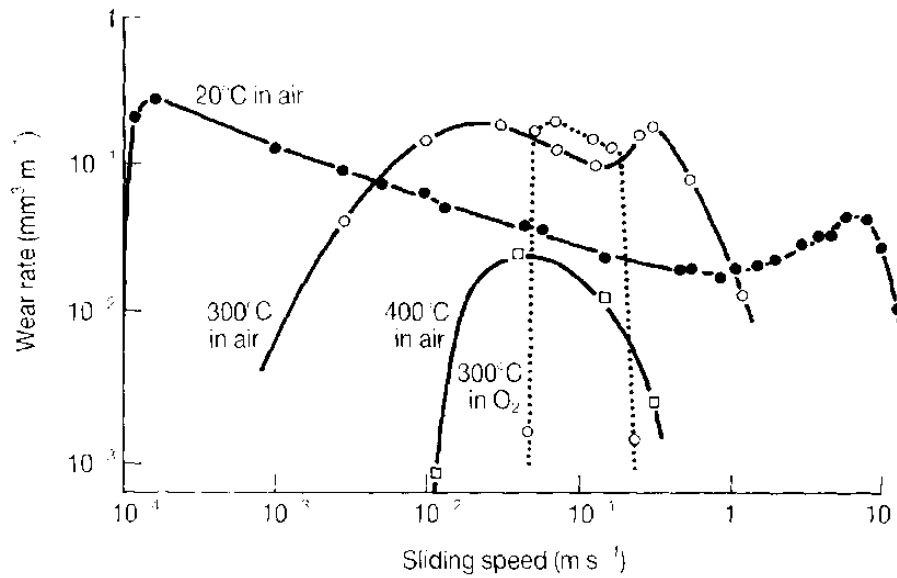


Figure 19 Variation in wear rate with sliding speed for brass sliding against steel in air and pure oxygen at various temperatures (from Lancaster J.K., *Proceedings of the Royal Society of London*, 1963 (16)).

As shown by **Figure 19**, at low sliding speeds sufficient time for the formation of a protective oxide film at the sliding interface was available and the observed wear rate was relatively low. Once the sliding speed was increased beyond a critical point, insufficient time was available to create a protective oxide layer and the observed wear rate sharply increased. Upon further increased sliding speed, the interfacial temperature was so high that a protective oxide film quickly formed despite the short time available for oxidation, and the wear rate dropped to a level similar to that at low sliding speeds. This pattern was observed for dry sliding in air, air at elevated temperatures, and in pure oxygen.

Because the influences of sliding speed and applied load on wear are not independent of each other, a useful way to observe the combined effects of these parameters is through wear maps. Wear maps are contour plots which are used to

illustrate the effects of two independent variables on the wear behavior of a material. This tool can be used to qualitatively describe the transitions in wear mechanisms observed under various sliding conditions by connecting the observed wear data with wear scar and wear debris analysis. An example wear map for unlubricated sliding of steel on steel was described by Lim and Ashby, and is shown in **Figure 20**.

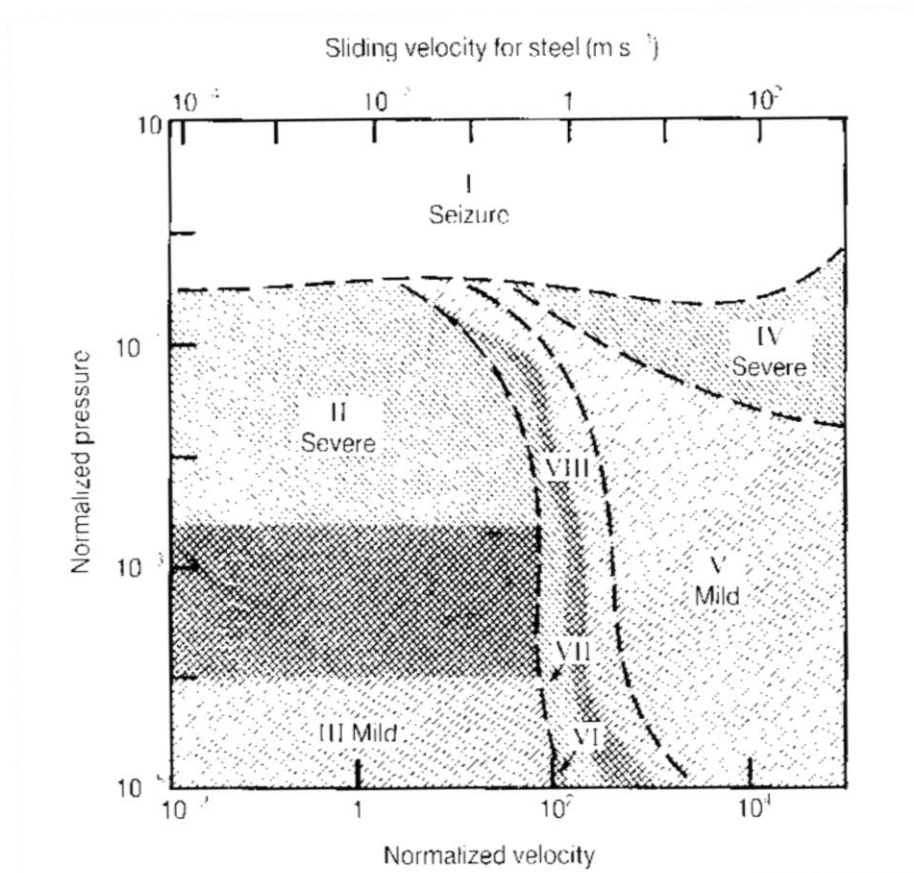


Figure 20 Wear map for dry pin-on-disk sliding of steel against steel (from Lim, Ashby, and Brunton, *Acta Met*, 1987 (17)).

3.0 Materials & Methods

3.1 Pin-on-Disk Wear and Friction Testing

The pin-on-disk test method is commonly used to evaluate the sliding friction and wear behavior of material pairs in various environments, at various sliding speeds, and under various applied loads (contact stresses). A disk of one material is contacted with a pin of a second material. A normal load is applied from the ball to the disk and held constant throughout the duration of the test. One material, typically the pin, is held stationary while the other (typically the disk) rotates or traverses back and forth (reciprocates) allowing the materials to slide against each other. The velocity of the moving material is held constant throughout the duration of rotating pin-on-disk experiments while the average velocity of the moving material is held constant for reciprocating pin-on-disk experiments. Typically, the normal force, friction force, coefficient of friction, and displacement from the initial interface are recorded throughout the duration of the test. ASTM Standard G99-05 for wear testing of materials with the pin-on-disk method gives requirements for surface roughness of materials tested, surface preparation and cleaning, test apparatus specifications, dimensions of materials tested, relative humidity and temperature for dry sliding tests, and data reporting. These specifications are purposefully very broad due to the many different types of experiments that can be conducted utilizing the pin-on-disk test method for simulation of various applications and environments. The maximum

allowable surface roughness recommended by ASTM G99-05 is $R_a \approx 0.6 \mu\text{m}$. A drawing of the general pin-on-disk test arrangement is shown in **Figure 21**. (18)

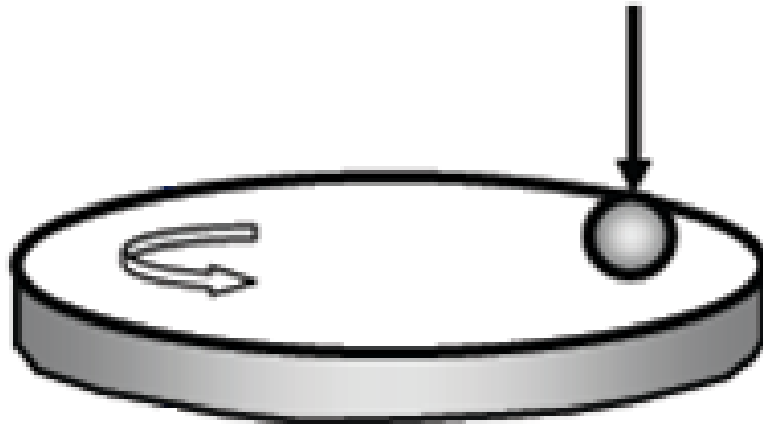


Figure 21 Generalized pin-on-disk wear test setup (from Blau, *Wear*, 2007 (19)).

A Center for Tribology Research Inc. (CETR) tribometer, model UMT 2.0, was used to conduct rotational pin-on-disk tests throughout this project in accordance with ASTM specification G99-05 (18), except where specified otherwise. The CETR UMT 2.0 is equipped with a rotational stage, normal and tangential force sensors, suspension, and position sensors. This apparatus utilizes a spherical sample as the pin and a nominally flat material positioned horizontally on a rotating stage as the disk. Prior to placing each sample within their fixtures for testing, each was rinsed with water and dried. Once secured in the tribometer for testing, each sample was swabbed with acetone to remove any surface contamination, and lastly swabbed with ethanol to remove any residue left behind by the acetone. Following testing, disk wear, ball wear, wear debris, and friction data can be analyzed depending on the goals of the experiment.

3.2 Wear Scar Characterization

3.2.1 Disk Scar

After the completion of a pin-on-disk experiment, it is necessary to characterize the damage incurred on the material surfaces. The wear-induced damaged zone is often referred to as a wear scar. Wear scars include material that has been removed from the surface by wear, material that has been displaced from its original location by plastic deformation, and often both. The primary measurement of wear is the volume of material removed or displaced under a given set of test conditions. In order to obtain this data from the wear scar, two-dimensional topographic profile data must be recorded from several cross sections of the wear scar. Several methods are available to obtain the topographic profile of a wear scar. The most common method is contact profilometry; other methods include optical and laser profilometry. Throughout this project, Laser Scanning Confocal Microscopy (LSCM) was utilized to collect topographic wear scar data (except where otherwise specified). This method of wear scar characterization has been proven to be more accurate, in general, than contact profilometry (20). This is because the profilometer's tip cannot fit inside pits, craters, or cracks that are smaller than the tip itself, which is not a problem when using lasers. A sample wear scar cross section profile, obtained by LSCM, is shown in **Figure 22**; note the slight ridge of plastically deformed material which is above the original flat surface.

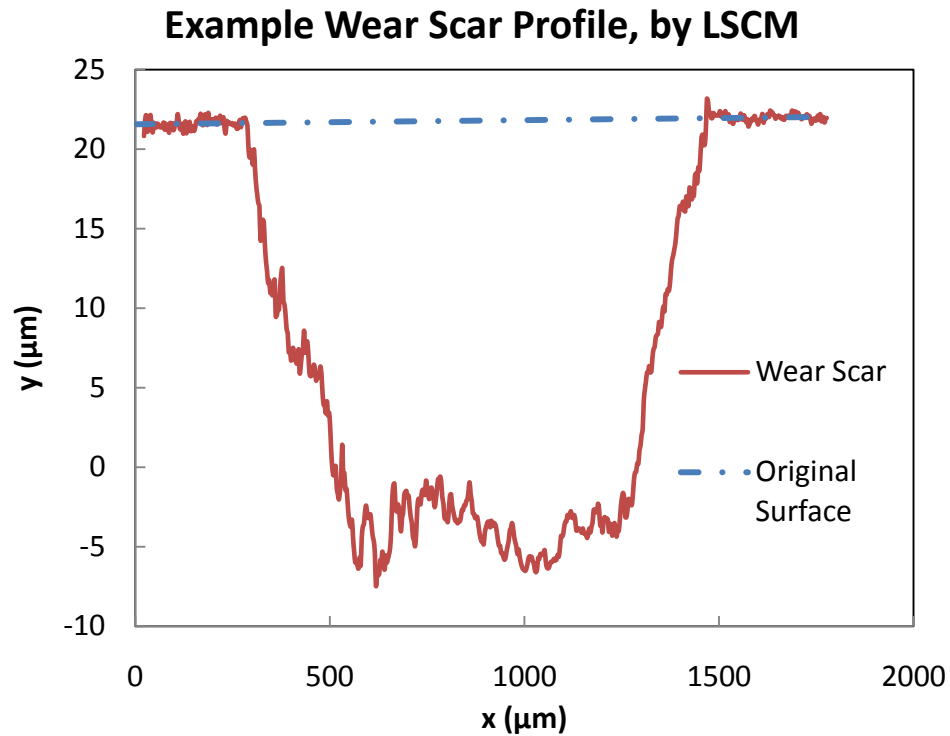


Figure 22 Example wear scar profile obtained by laser scanning confocal microscopy.

Because wear damage may not be evenly distributed throughout the entirety of the wear scar, typically three profiles are taken from equidistant points along its length or circumference. Each topographic profile is then used to determine the volume of material displaced or removed by wear using the following calculation sequence:

- 1) Calculate the area of material removed by wear from the original surface for each topographic profile (usually 3 profiles taken from equidistant points along the wear scar). This is equal to the area between the topographic curve of the wear scar and the original flat field.
- 2) Multiply the area of material removed by the circumference of the wear scar (or length of scar for reciprocating POD tests), to get the approximate volume of material displaced by wear representative of the individual topographic profile.
- 3) Repeat steps 1-2 for each profile.

- 4) Average the area of material removed from each topographic profile to get the estimated volume of wear for the disk.

3.2.2 Ball Scar

Each ball scar was optically imaged and the dimensions of the scar were observed using 2D images because 3D topography analysis of pin scars can be very time consuming. In the case of a circular wear scar, **Equation 17** was utilized to estimate the volume of pin material lost due to wear for each test; here V is the volume of material worn from the pin (mm^3), R_0 is the radius of the spherical pin (m), d_{scar} is the diameter of the wear scar (m), and h is expressed by **Equation 18** (21).

Equation 17
$$V = \frac{1}{3} \pi h^2 (3R_0 - h)$$

Equation 18
$$h = R_0 - \sqrt{\left(R_0^2 - \frac{d_{\text{scar}}^2}{4}\right)}$$

In the case of an elliptical wear scar, the wear volume calculation is slightly different as shown by **Equation 19**; here a is defined as one half the length of the ellipse, b is one half the width of the ellipse, and h is defined by **Equation 20**.

Equation 19
$$V = \frac{a}{3b} \pi h^2 (3R_0 - h)$$

Equation 20
$$h = R_0 - \sqrt{\left(R_0^2 - b^2\right)}$$

Note that these simplified calculation methods do not account for the presence of any compound curvature of the pin wear scar, and were used for simplicity and efficiency. A more sophisticated and accurate technique which uses a contact

profilometer was described by Blau and Qu (21), but could not be utilized in this work due to the unavailability of a suitable profilometer.

3.3 Friction Observation

Throughout each pin-on-disk test, the applied normal load, and friction force were recorded with time. The coefficient of friction is the ratio of these forces. Plotting the coefficient of friction versus time gives a friction profile; an example of which is shown below (**Fig. 23**). Depending on the test conditions, several changes in friction may result throughout the test. Generally, there is a very brief period of low friction resulting from surface contamination (ex: adsorbed moisture from the atmosphere), followed by a high level of friction due to the elimination of surface roughness (sometimes referred to as break-in or run-in), and finally a steady state regime in which friction is relatively constant. Steady state friction is often taken as the average coefficient of friction over the last 1,000 seconds of sliding, and is often used to compare the friction performance of material pairs. (22)

Carburized 316L Sliding vs. Tungsten Carbide

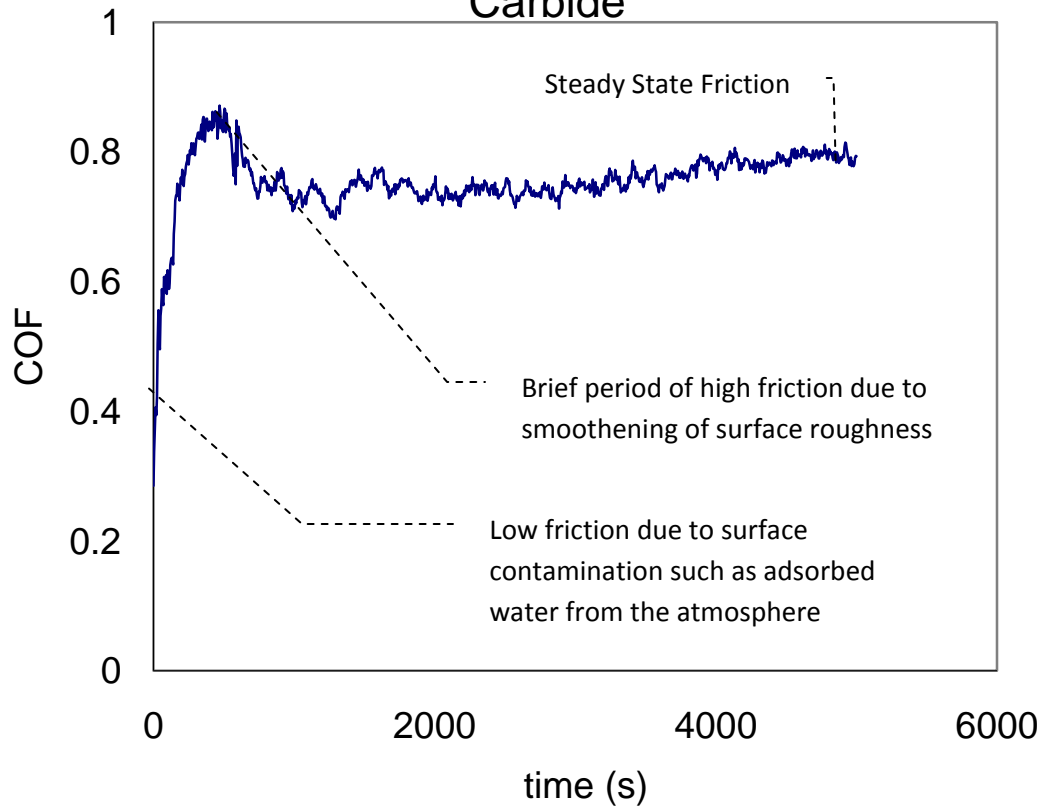


Figure 23 Example friction profile for carburized 316L sliding against a WC ball at 0.1 m/s under a 5 N applied load

4.0 Review of Previous Carburized 316L Tribology Investigations

The tribological properties of austenitic stainless steel AISI 316L carburized by the Swagelok low temperature process have been investigated by Qu et al (19), who studied friction and wear behavior utilizing pin-on-disk tests. The carburized 316L displayed remarkably improved wear resistance compared to non-treated 316L when sliding in salt water, and air at temperatures up to 400°C (Fig. 24 and Fig. 25). They also observed that steady state friction coefficients of self mated carburized 316L were slightly higher than those of non-treated 316L under similar sliding conditions (Fig. 26).

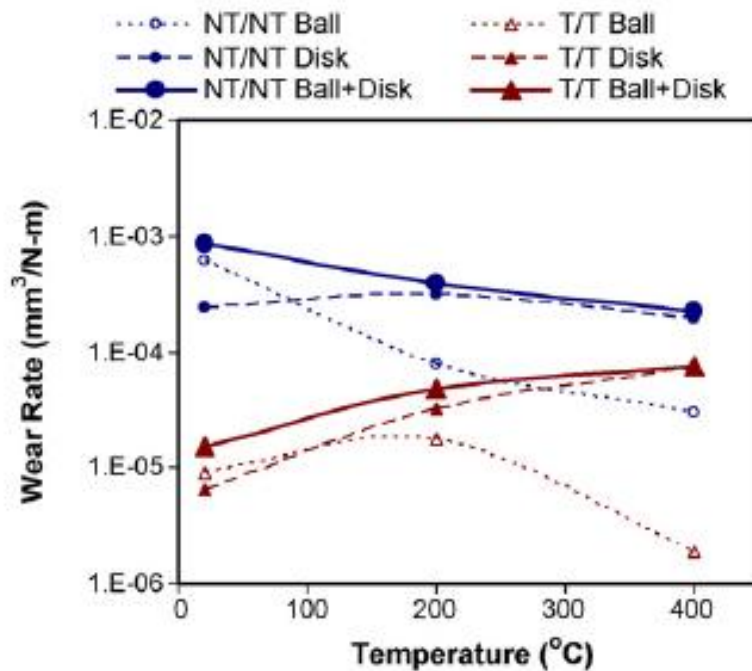


Figure 24 Effects of temperature on wear behavior under dry sliding conditions (ball/disk), (from (19), Qu et al, Wear, 2007).

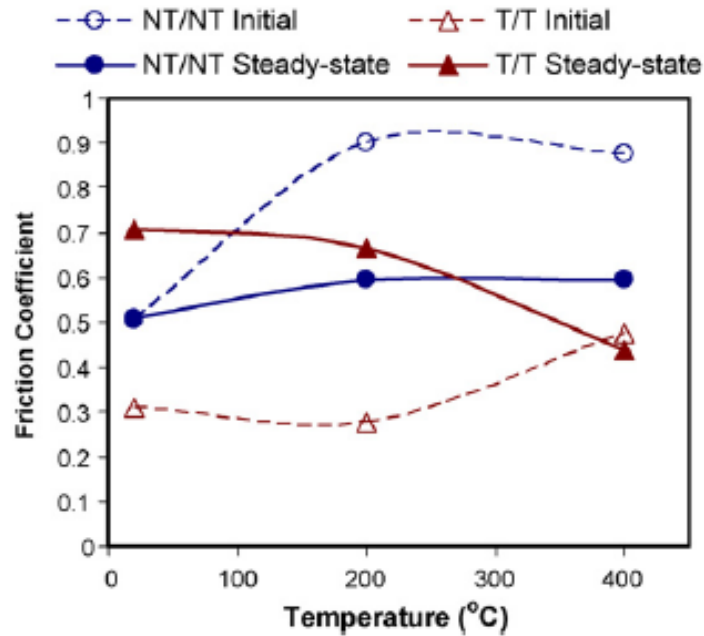


Figure 25 Effects of temperature on friction under dry sliding conditions (ball/disk), (from (19), Qu et al, Wear, 2007).

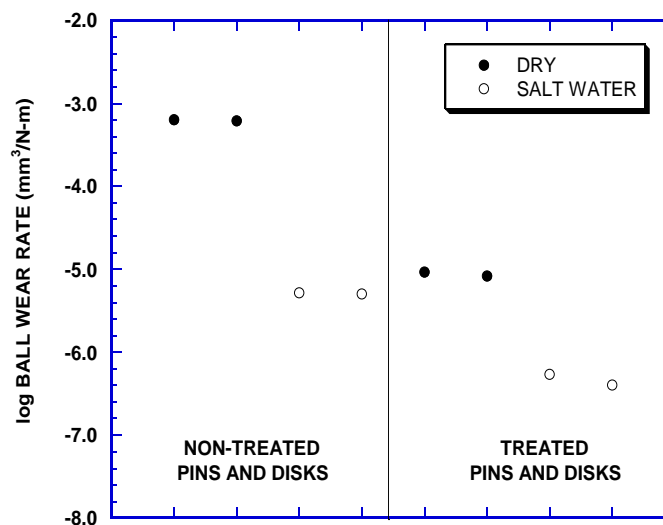


Figure 26 Wear in salt water, (from (19), Qu et al, Wear, 2007).

Abrasive wear tests were also conducted by Blau and Qu. They found that low temperature carburization reduced abrasive wear by almost 40% (Fig. 27). The sum of these findings illustrates the wide range of tribological benefits gained by low temperature carburization.

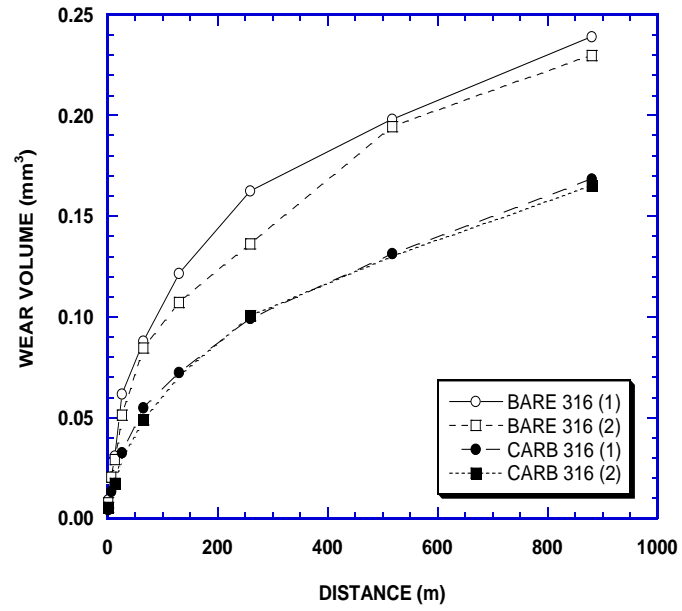


Figure 27 Abrasive wear test comparison, (from (19), Qu et al, Wear, 2007).

5.0 Wear of 316L Carburized at Low Temperature Sliding Against Hard Materials

5.1 Objective & Motivation

Hard materials, when sliding against relatively soft materials (stainless steels), can cause several types of wear, including plastic deformation-induced wear, such as plowing, scratching, and extruding. This is due to the high yield strength of the hard material with respect to the stainless steel. Debris that is generated from the hard material during sliding will act as third body hard particles tumbling between the sliding surfaces, leading to abrasive wear. Two-body abrasive wear may also occur due to the sliding of sharp rigid features on the hard counterface. The observed resistance to abrasive wear, shown experimentally by Blau and Qu (19), suggests that low temperature carburization will improve the wear resistance of stainless steels when sliding against very hard materials.

Pin-on-disk tests were performed to evaluate the wear resistance of carburized 316L when sliding against various hard counterface materials. This work was conducted at Oak Ridge National Labs under the guidance of Dr. Peter Blau and Dr. Jun Qu, and was intended as a training exercise, to gain the skills necessary to investigate the friction and wear behavior of low temperature carburized stainless steels. The wear resistance of non-treated 316L sliding against hard materials was also evaluated at Case Western Reserve University to provide a comparison to the wear of carburized 316L.

5.2 Experimental Materials & Methods

The pin-on-disk test method was utilized to investigate friction and wear behavior of carburized and non-treated 316L sliding against three hard counterface materials, in accordance with ASTM G99-05 (18). Al₂O₃, WC-Co, and M50 tool steel (Salem Ball Co.) were the three hard counterface materials used to evaluate friction and wear of carburized 316L. The hardness of the materials tested are shown in **Table 2**.

Material	Hardness (GPa)
316L	3.8
Carburized 316L	9.1
Al ₂ O ₃	24.8
WC-Co	17.3
M50 Tool Steel	9.0

Table 2 Hardness of selected materials for pin-on-disk hard counterface study, obtained by Vickers microhardness tests utilizing a 50 g load.

The tribometer used to investigate carburized 316L was custom built by Oak Ridge National Laboratory (ORNL). 316L disks of approximately one inch diameter by 0.25 inch thickness were metallographically polished to $R_a \approx 0.1 \mu\text{m}$, and then carburized by the Swagelok low temperature process. Following the ORNL tests, non-treated 316L was evaluated under similar conditions at Case Western Reserve University using a Center for Tribology Research Inc. (CETR) tribometer. Ideally these tests would be conducted with the same tribometer; however this was not possible due to time and access constraints at ORNL. **Table 3** shows the experimental conditions for each test.

Ball Material	Disk Material	Load (N)	Track dim (mm)	Speed (m/s)	Test length (m)	Rel. Humid (%)	T _{room} (°C)	Test Location
M-50	Carburized 316L	5	18.5	0.1	500	33	21	ORNL
Alumina	Carburized 316L	5	18.5	0.1	500	32	21	ORNL
WC/Co	Carburized 316L	5	18.5	0.1	500	32	21	ORNL
WC/Co	Carburized 316L	5	18.5	0.1	500	41	21	ORNL
M-50	Carburized 316L	5	18.5	0.1	500	41	21	ORNL
Alumina	Carburized 316L	5	18.5	0.1	500	41	21	ORNL
Alumina	316L	5	24	0.1	500	35	21	CWRU
WC	316L	5	24	0.1	500	35	21	CWRU
M50	316L	5	24	0.1	500	35	21	CWRU

Table 3 Pin-on-disk test conditions for carburized 316L and non-treated 316L sliding against various hard counterface materials

For tests conducted at ORNL, ball and disk wear was measured using contact profilometry. Three topographic profiles were recorded for each disk. The disk wear volume was then calculated by integrating to obtain the area between the scar profile and the original flat surface, which was then multiplied by the length of the scar to obtain the wear volume. Contact profilometry was not available for use at CWRU, thus Laser Scanning Confocal Microscopy (LSCM) was used to obtain topographic wear scar data for all tests conducted at CWRU. Three topographic profiles for each wear scar were obtained using LSCM, and the volume of wear was calculated using the same methodology described above.

Friction data was recorded throughout the duration of each test (both ORNL and CWRU) and the steady state friction coefficient value was taken as the average observed for the final 1,000 seconds of sliding.

5.3 Results and Discussion

The pin-on-disk test results show that low temperature carburization leads to an enormous improvement in wear resistance when sliding against hard counterface materials. The normalized wear rate of treated 316L sliding against the three hard materials was similar to that obtained by Blau and Qu (discussed above) for carburized 316L sliding against non-treated and carburized 316L (**Fig. 28**). This suggests that carburized 316L is very resistant to wear by abrasive hard particles generated by the counterface materials during sliding. Carburized 316L wear was greatest when sliding against non-treated 316L, and was least when sliding against alumina. This may be a result of adhesive wear, which should be more pronounced when sliding against a soft material of similar composition, and would be minimized when sliding against a hard non-metallic material such as alumina.

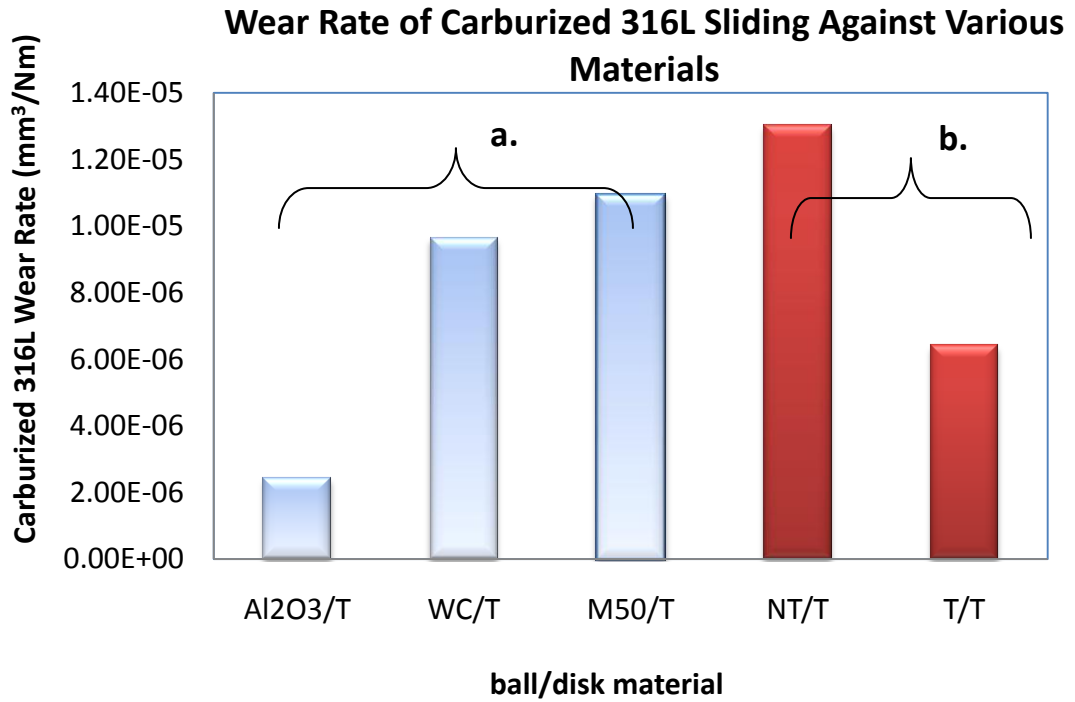


Figure 28 Wear rate of treated 316 disks vs. various counterface materials for (a.) this experiment, and (b.) previous ORNL data (19), (T=carburized 316L, NT=non-treated 316L).

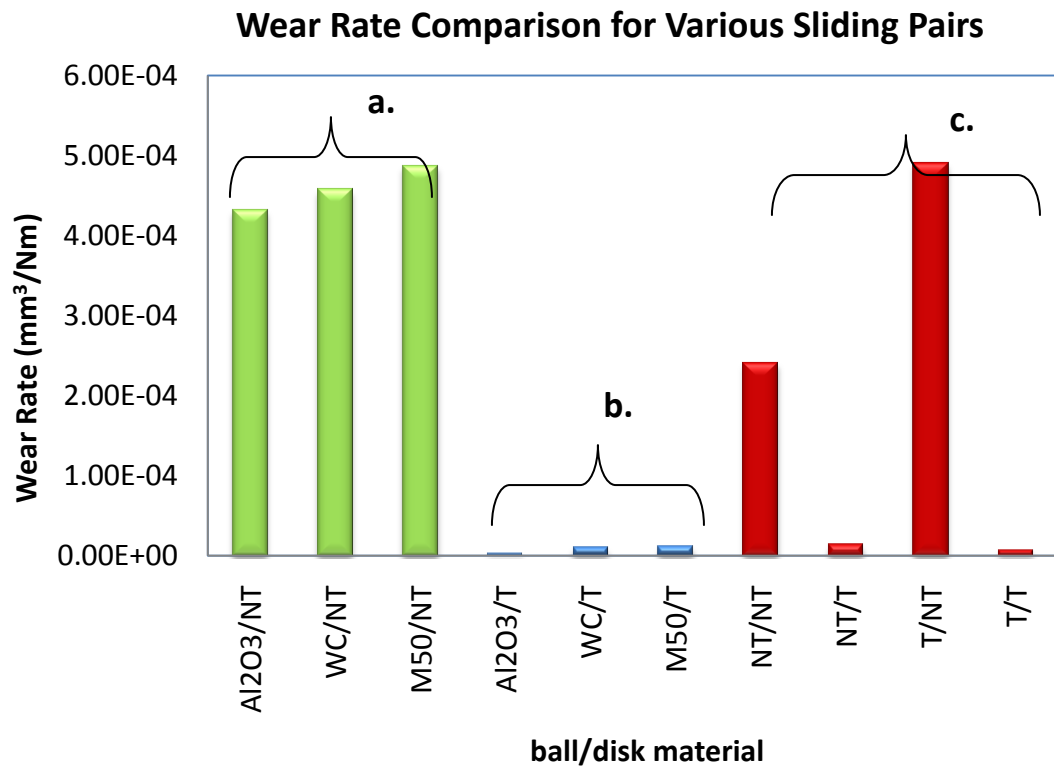


Figure 29 Wear rate comparison of various material pairs for (a.) green - CWRU non-treated 316L results, (b.) blue - ORNL treated 316L results, and (c.) red - ORNL Blau & Qu results (19), (T= treated 316L and NT=non-treated 316L)

The non-treated 316L disks tested at CWRU showed a much greater wear rate than carburized 316L. The wear rates observed for 316L sliding against M50 steel, WC, and alumina were similar to that observed for non-treated 316L sliding against treated 316L by Blau and Qu (**Fig 29**). From this data it is clear that low temperature carburization greatly enhances the wear resistance of 316L when sliding against materials of high hardness. The wear rate of non-treated 316L sliding against itself is significantly less than when sliding against hard materials (including carburized 316L). This may be due to 316L's susceptibility to abrasive wear, which would be much more prevalent when sliding against a hard material that produces abrasive wear debris.

The steady state friction coefficients observed for carburized 316L were slightly greater than that of non-treated 316L for all test conditions (**Fig. 30**). This may be due to the increased yield strength of the expanded austenite region which requires more energy for plastic deformation, thus leading to an increased resistance to sliding under these conditions. While the increased yield strength of the carburized region results in an increase in friction during dry sliding, it also results in greatly improved resistance to abrasive wear. Abrasive wear causes plastic deformation by the embedding and sliding of hard particles into the soft sliding surface. The generally small size of abrasive wear particles results in high contact stresses at their interface with the sliding material. This combined with their high hardness easily enables the plastic deformation of 316L, however once carburized; the significantly increased yield stress of the surface region greatly inhibits this mechanism of wear.

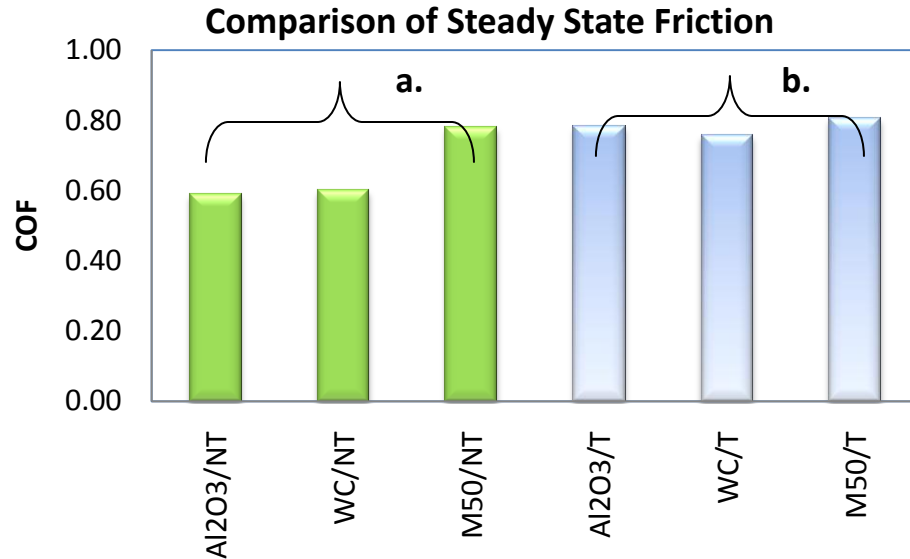


Figure 30 Friction comparison for (a.) non-treated 316L data from CWRU, and (b.) treated 316L data from ORNL (19), (T=carburized 316L, NT=non-treated 316L)

5.4 Summary of Wear Performance Sliding vs. Hard Materials

Pin-on-disk tests were conducted at Oak Ridge National Labs and Case Western Reserve University investigating the friction and wear behavior of non-treated and carburized 316L when sliding against hard counterface materials. Previous studies by Blau and Qu revealed that low temperature carburization greatly enhances 316L's resistance to abrasive wear. This was further confirmed by this set of experiments, where low temperature carburization was found to greatly enhance the wear resistance of 316L sliding against hard counterface materials. Carburization also increased the steady state coefficient of friction, which was lower for non-treated 316L under all test conditions. These results show that although low temperature carburization increases friction when sliding against hard materials, wear resistance is greatly enhanced due to the elevated yield stress of the carburized region.

6.0 Wear Maps of 316L Carburized at Low Temperature

6.1 Objective & Motivation

The purpose of this series of experiments was to observe the combined effects of load and sliding speed on the wear of low temperature carburized 316L to gain an understanding of the extended application range achievable. Strong changes in wear rate resulting from slight changes in applied load or sliding speed are known to occur for the sliding of many metallic materials. The influence of low temperature carburization on wear rate transitions due to load and sliding speed were observed. Wear maps illustrating the combined effects of load and velocity on wear rate and wear mechanisms were constructed to show the benefits of low temperature carburization.

6.2 Materials

AISI 316L material (17.46% Cr, 12.93% Ni, 2.71% Mo, 1.27% Mn, 0.67% Si, 0.17% Cu, 0.14% Co, 0.02% C, <0.02% P, and <0.01% S (23)) was obtained from Carpenter Technology Corporation, and machined to 2.75"x2.75"x0.25" specimens. Each disk was ground to a surface roughness of $R_a \approx 0.6 \mu\text{m}$ and then carburized in a production furnace by the Swagelok Co. Prior to wear testing, the specimens were metallographically polished to a surface roughness of $R_a \approx 0.3 \mu\text{m}$. A cross section of the carburized material was metallographically polished and etched to observe the thickness of the hardened case (**Fig. 31**). Vickers microhardness tests were performed using a 10 g load on the cross sectioned specimen to obtain a hardness depth profile of the carburized material (**Fig. 32**).

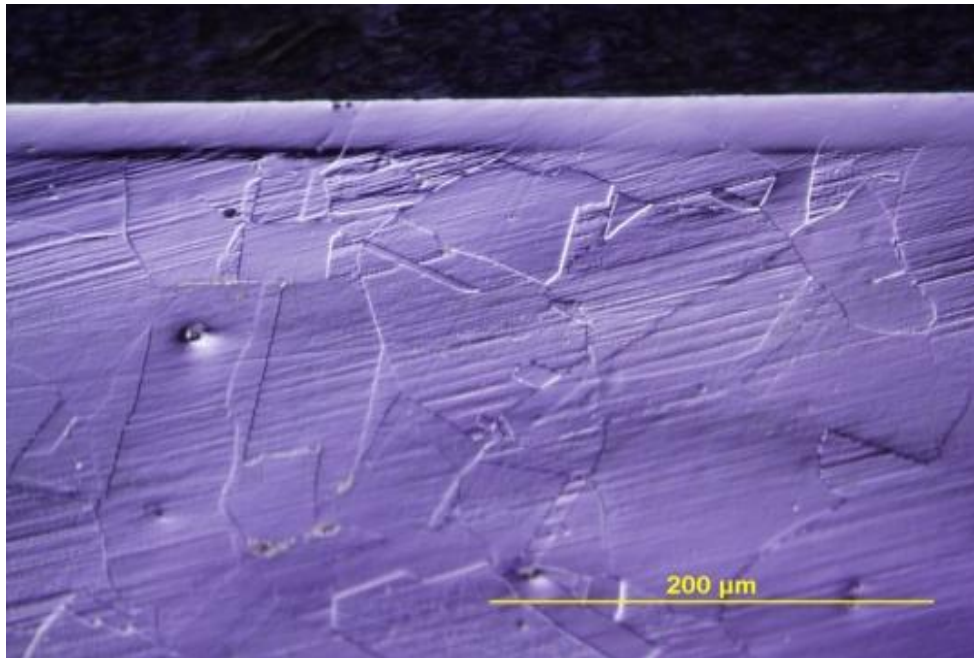


Figure 31 Optical micrograph of carburized 316L micrograph obtained using Nomarski contrast

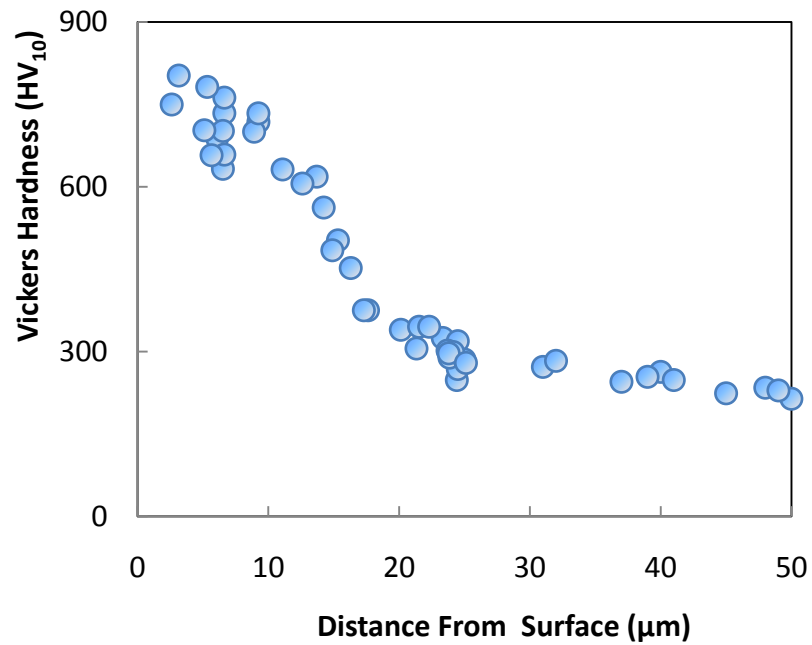


Figure 32 Hardness depth profile of carburized 316L obtained using a 10 g load and a Buehler microhardness tester

As shown in **Figures 31 and 32**, the etch-resistant surface-hardened region of the carburized material extends roughly 25 μm beneath the surface and reaches a hardness

of approximately 800 HV₁₀ in the near-surface region. The surface microhardness (HV₂₅) of the non-treated and carburized materials was 280 HV and 1010 HV respectively.

Each disk was paired with a high alumina ceramic ball for unlubricated sliding tests (McMaster Carr, product #9599K13, surface hardness specified by McMaster of 1700 HV, and sphericity of 0.000025" (24)). Alumina was selected as the counterface material because of its high hardness with respect to both carburized and non-treated 316L.

6.3 Experimental Methods

6.3.1 Pin-on-disk Apparatus and Procedure

Pin-on-disk tests were utilized to observe the friction and wear of carburized and non-treated 316L disks sliding against Al₂O₃ for sliding speeds of 0.1 m/s, 0.3 m/s, and 0.6 m/s, under loads ranging from 4 N to 40 N. A Center for Tribology Research Inc. (CETR) tribometer, model UMT 2.0, was used to conduct the pin-on-disk tests in accordance with ASTM specification G99-05 (18).

6.3.2 Experimental Design

The loads used were selected based on estimates of the maximum shear stress due to traction. The maximum shear stress caused by traction under a given normal load will be located at the interface of the sliding materials when the coefficient of friction is greater than 0.3 (11). This shear stress can be estimated using **Equations 20 and 21**, where μ is the coefficient of friction, P is the applied normal load, P_0 is the maximum contact pressure under static conditions, R is the relative radius of the

contacting surfaces, and E^* is the relative elastic modulus of the contacting materials (11).

Equation 21

$$\tau_1 = \mu P_0$$

Equation 22

$$P_0 = \left(\frac{6PE^{*2}}{\pi^3 R^2} \right)^{1/3}$$

If a coefficient of friction of 0.8 is assumed for pin-on-disk dry sliding tests of carburized 316L stainless steel paired with alumina, which was a good average of that measured in the sliding wear tests, the maximum shear stress due to traction can be estimated as 0.88 to 1.90 GPa for applied loads of 4 to 40 N (**Fig. 33**). This shear stress range far exceeds the yield strength in pure shear of 316L stainless steel (≈ 0.23 GPa), and was selected to test the tribological performance of carburized 316L under conditions that would typically be considered too severe for conventional stainless steels.

Surface Shear Stress Distribution Under Traction Compared to the Shear Strength of Carburized and Non-Treated 316L
 $\mu=0.8$

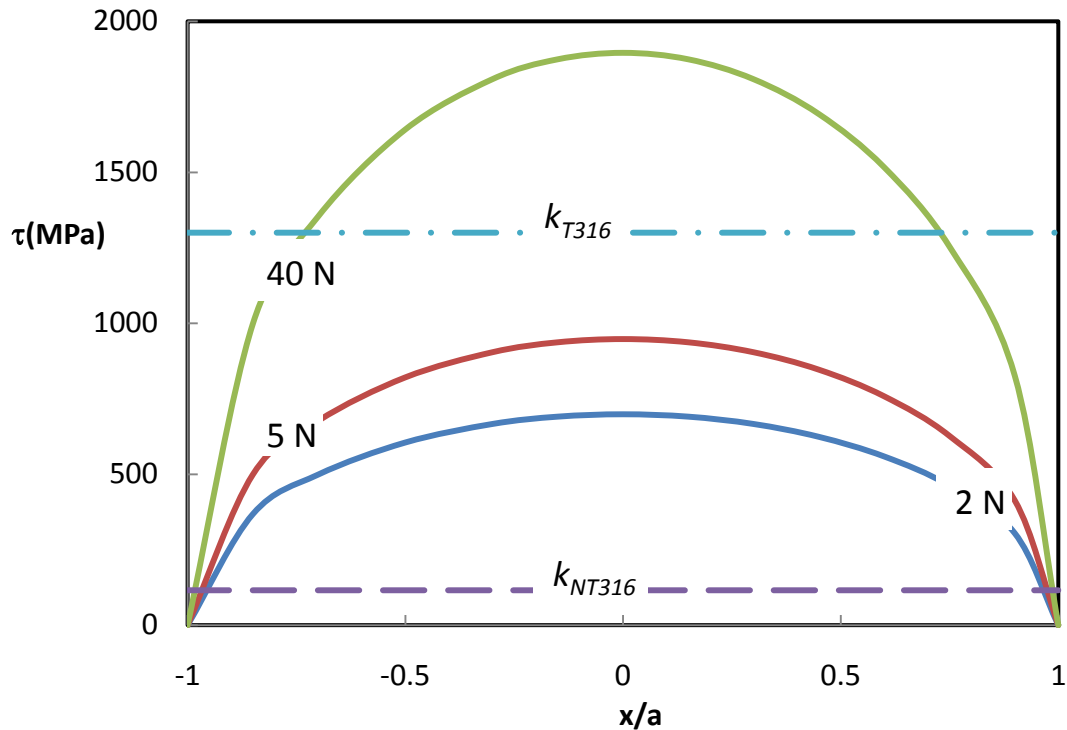


Figure 33 Surface shear stress distribution due to traction for dry sliding of an Al_2O_3 ball against a stainless steel disk under normal loads of 5 N, 40 N, and 2 N for an assumed coefficient of friction equal to 0.8. k_{material} is the approximate shear strength of carburized 316L (T_{316}) and non-treated 316L (NT_{316}), τ is the shear stress due to normal load and traction, and x/a is the normalized distance from the center of the circular contact area.

The sliding speed range, 0.1 m/s – 0.6 m/s, was selected based on estimated interfacial flash temperatures, the maximum temperature achieved at the interface of sliding asperities due to frictional heating. Temperature rise of several hundred degrees ($^{\circ}\text{C}$) are possible under dry sliding conditions. While this phenomenon is difficult to observe experimentally, it can be approximated theoretically using **Equations 1-3**, as discussed by Ashby (10).

Because theoretical approximation of flash temperature is dependent on the assumed real contact area and heat transfer parameters of the system, these estimates

are often inaccurate. A primary source of this error is the heat sink diffusion distance of the pin, which is a function of the real pin-fixture contact area, and the conductive heat transfer coefficient (Fig. 8). Because the conductive heat transfer coefficient and the real pin-fixture contact area are unknown, high and low estimates of flash temperature were made by assuming several values of this diffusion distance. From these estimates, dry sliding of 316L against alumina can produce asperity interface temperatures of 400°C or more at sliding speeds of 0.6 m/s, depending on the contact conditions (**Fig 34**).

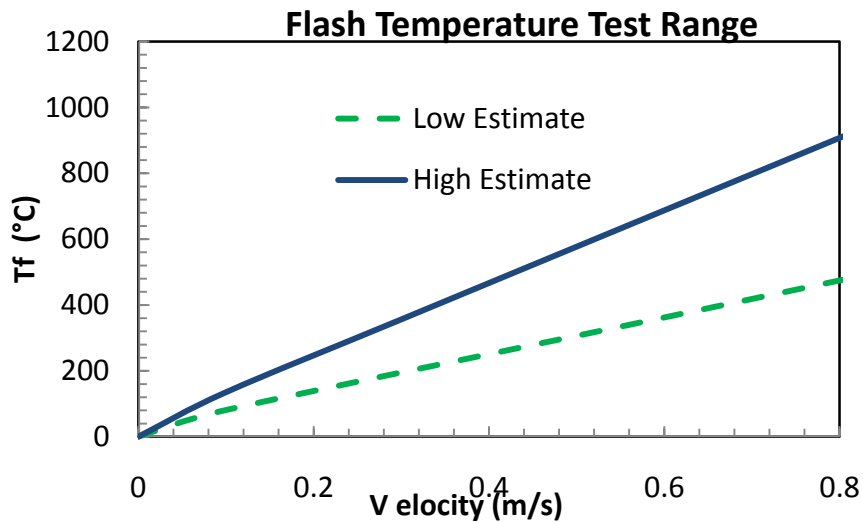


Figure 34 Flash temperature approximation for dry sliding of an alumina ball against a 316L stainless steel disk

The test conditions for each pin-on-disk test conducted in this study are listed in **Table 4**.

Disk Material	Load (N)	Velocity (m/s)	Total Sliding Distance (m)	Track Diameter (mm)	Temperature (°C)	Relative Humidity (%)
Carburized 316L	4	0.1	1,000	36	21	52
Carburized 316L	7	0.1	1,000	34	22	51
Carburized 316L	30	0.1	1,000	42	23	51
Carburized 316L	12	0.1	1,000	50	23	51
Carburized 316L	20	0.1	1,000	58	23	50
Carburized 316L	40	0.1	1,000	58	22	55
Carburized 316L	4	0.3	1,000	24	21	49
Carburized 316L	12	0.3	1,000	34	21	49
Carburized 316L	20	0.3	1,000	42	21	49
Carburized 316L	25	0.3	1,000	50	22	49
Carburized 316L	30	0.3	1,000	58	22	49
Carburized 316L	40	0.3	1,000	80	21	58
Carburized 316L	4	0.6	1,000	40	23	56
Carburized 316L	12	0.6	1,000	46	21	51
Carburized 316L	40	0.6	1,000	52	21	51
Carburized 316L	25	0.6	1,000	60	24	51
316L	4	0.1	1,000	34	22	57
316L	12	0.1	1,000	52	22	59
316L	20	0.1	1,000	42	23	54
316L	40	0.1	1,000	50	23	56
316L	4	0.3	1,000	40	22	51
316L	20	0.3	1,000	30	23	51
316L	30	0.3	1,000	38	24	51
316L	40	0.3	1,000	46	22	54
316L	4	0.6	1,000	58	23	54
316L	12	0.6	1,000	30	21	50
316L	30	0.6	1,000	50	20	58
316L	40	0.6	1,000	60	20	60

Table 4 Load and Velocity Effects on Wear, pin-on-disk test conditions for dry sliding against an alumina ball

6.3.3 Wear Scar Characterization

A Laser Scanning Confocal Microscope (LCSM) was used to characterize the wear scars from each experiment. Three topographic profiles of each disk scar were recorded at equally spaced locations around their perimeters. The volume of material lost was calculated by multiplying the area between the scar profile and the flat field surface by

the circumference of the wear scar. Three dimensional models of each wear scar were constructed using the confocal data to compare scar features such as plastic ridge formation and scar size.

6.3.4 Wear Debris Characterization

Wear debris obtained from each test was collected and observed using a Hitachi S4500 Scanning Electron Microscope (SEM). This was accomplished by transferring loose wear particles from the surface of each disk to carbon tape, which was then mounted in the SEM. The size, morphology, and composition of the wear debris were used to diagnose and compare wear mechanisms.

6.3.5 Construction of Wear Maps

Wear maps were made by combining the wear scar data with wear debris observations. Least squares linear regression of wear, applied load, and sliding velocity data was utilized to obtain an empirical relationship (**Equation 23**) describing wear; here V is the volume of material removed by wear (mm^3), P is the applied load (N), v is the sliding velocity (m/s), and α , β , δ , γ , ϵ , and c are constants.

Equation 23

$$V = \alpha P + \beta v P + \gamma v + \delta P^2 + \epsilon v^2 + c$$

This approach considers the effects of sliding speed and load, and interactions between these variables, on wear. Contour lines indicating the volume of material lost by wear vs. the applied load and the sliding speed were constructed using these empirical relationships. Wear scar and wear debris analyses were overlaid onto the contour plots to relate the observed wear mechanisms to the wear resistance of each material.

6.4 Results

6.4.1 Friction Results

The coefficient of friction (COF) was recorded throughout each pin-on-disk test by utilizing the tangential and normal load sensors of the CETR tribometer. The ratio of these forces is equal to the coefficient of friction as described above. The steady state coefficient of friction, which represents the stable friction value observed once steady state has been reached, was taken to be the average coefficient of friction over the last 1,000 seconds of sliding. Under all test conditions, friction for carburized 316L was greater than that of non-treated 316L, however the magnitude of this difference was dependant on the test conditions.

For sliding at 0.1 m/s, the COF for carburized 316L was least, 0.4, when sliding under a 4 N applied load. As the applied load increased, the COF increased and reached a maximum of 0.87 when sliding under a 12 N applied load (**Fig. 35**). Upon further load increase, the COF fell to about 0.71. Non-treated 316L sliding at 0.1 m/s against alumina revealed a similar trend, with a minimum of 0.39 under a 4N load, and a maximum of 0.56 under a 12 N load.

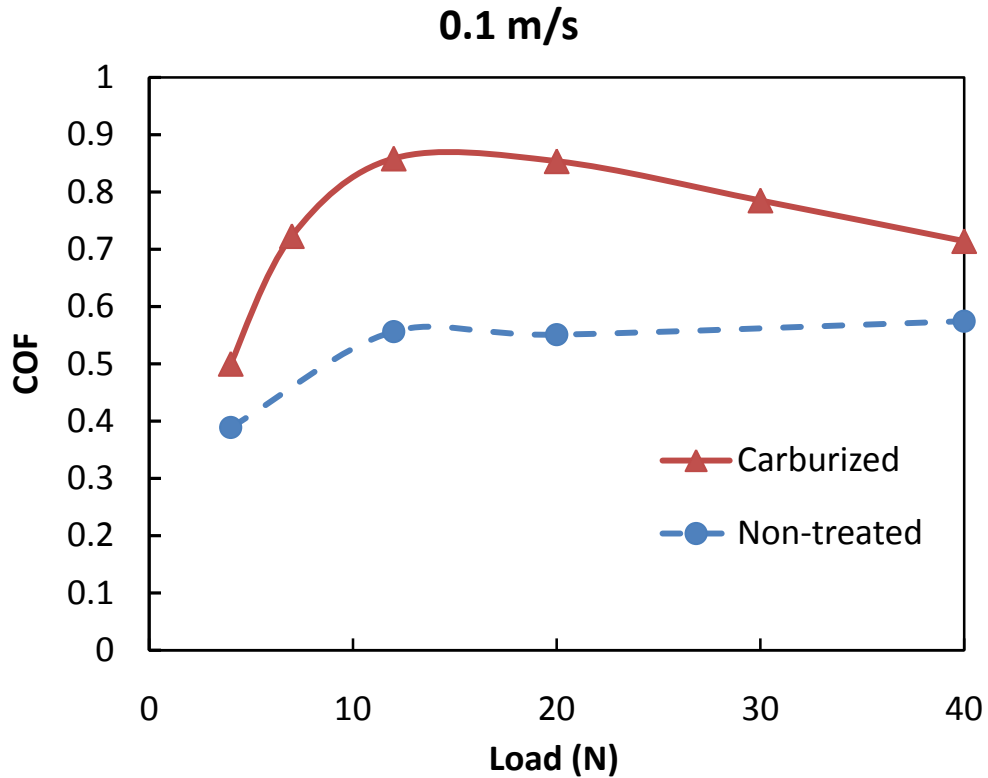


Figure 35 Steady State COF observed for 0.1 m/s dry sliding against alumina

Once the sliding speed was increased to 0.3 m/s, the relationship between friction and applied load became slightly different. The maximum COF of 0.85 for carburized 316L was observed when sliding under a load of 4 N, and a minimum of 0.66 was observed under a load of 40 N (**Fig. 36**). Similarly, non-treated 316L showed maximum friction when sliding under an applied load of 4N, 0.67. As the applied load increased, the COF of non-treated 316L decreased and reached a minimum of 0.36 under an applied load of 30 N. This was likely due to increased oxidation and plasticity resulting from frictional heating. Once the applied load reached 40 N, the COF increased to 0.61, which was likely due to a sharp increase in the real contact area once the load reached 40 N, resulting in increased friction.

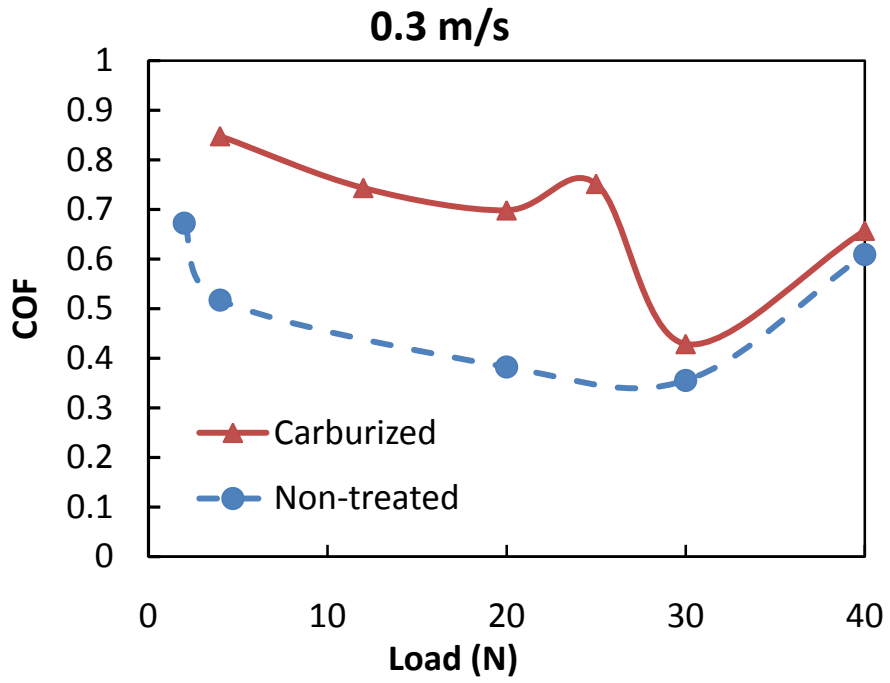


Figure 36 Steady state coefficient of friction observed for 0.3 m/s dry sliding against alumina

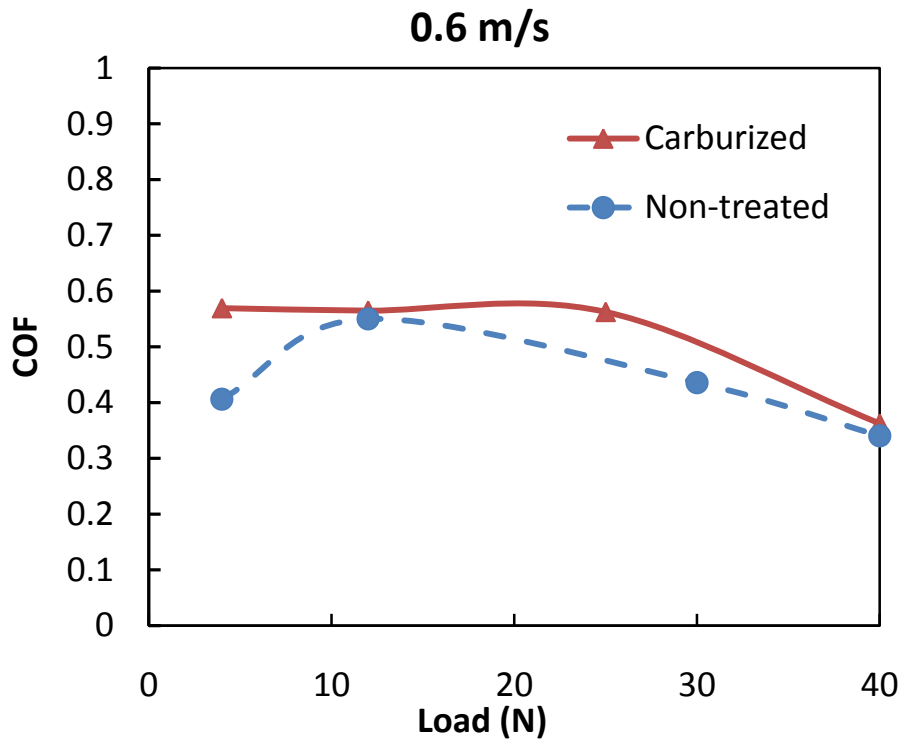


Figure 37 Steady state coefficient of friction for 0.6 m/s dry sliding against alumina

For sliding speeds of 0.6 m/s, carburized 316L again showed greater friction than non-treated 316L over the complete range of applied loads. Maximum coefficient of friction for carburized 316L was 0.57 under an applied load of 4N, and a minimum of 0.36 under an applied load of 40 N (**Fig. 37**). The minimum coefficient of friction observed for non-treated 316L was under an applied load of 40 N, and the maximum, 0.55, was observed under a load of 10 N. Note that when sliding at 0.6 m/s, the steady-state friction difference between carburized 316L and non-treated 316L is much less than that observed at lower sliding speeds. This is likely due to frictional heating effects such as oxidative wear or local reduction of yield strength.

6.3.2 Wear Volume

Several abrupt changes in wear were observed for non-treated 316L stainless steel as the applied load increased for the three sliding speeds utilized (**Fig. 38a**). A sharp transition from mild to severe wear was observed for 0.3 m/s sliding at an applied load of 30 N. Another transition from mild to severe wear was observed for 0.1 m/s sliding between 20 N and 40 N. In contrast, the wear rate of non-treated 316L for 0.6m/s sliding remained relatively constant for loads ranging from 10 N to 40 N.

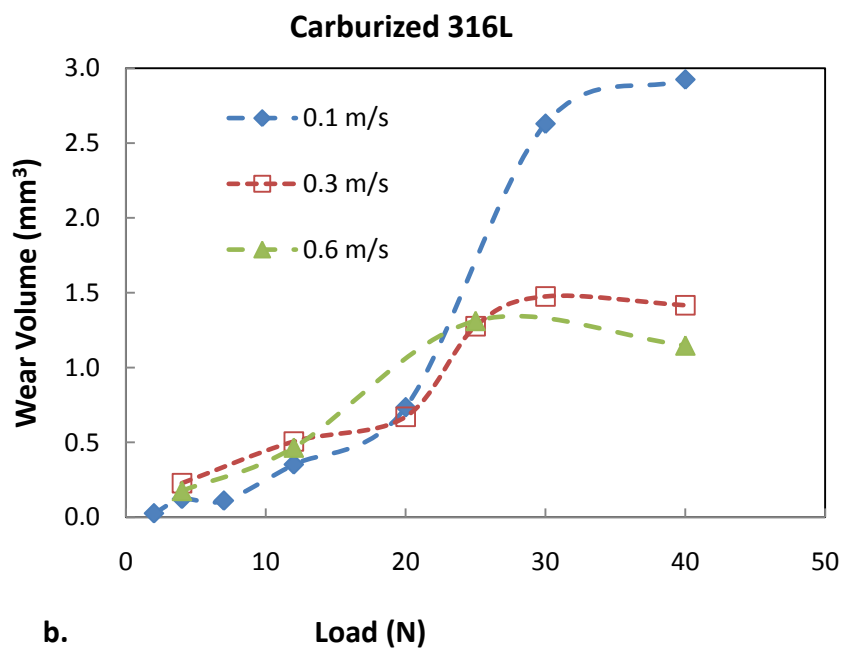
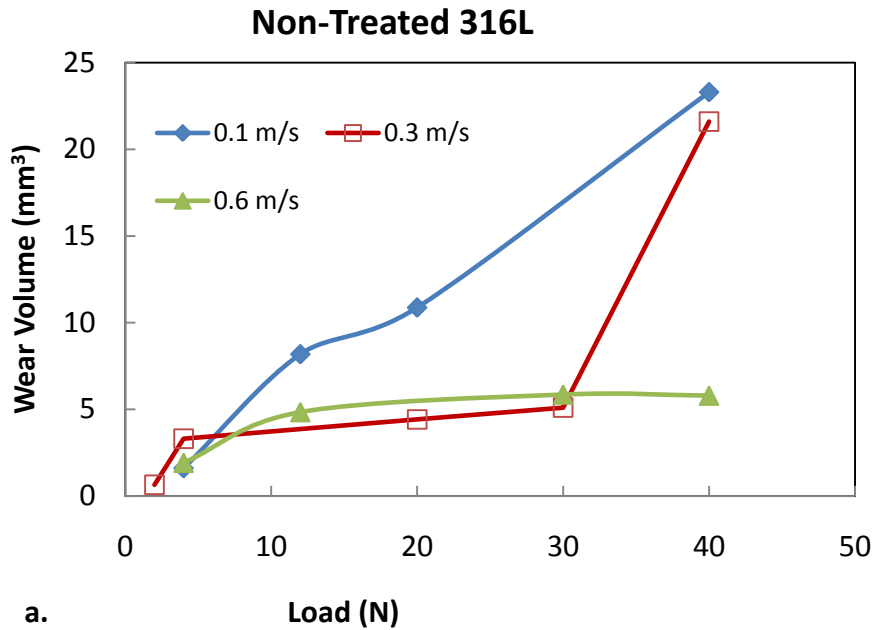


Figure 38 Pin-on-disk test results comparing (a.) Non-treated 316L stainless steel, and (b.) Carburized 316L stainless steel

The volume of material lost by wear for carburized 316L was considerably smaller than for non-treated 316L under all test conditions, although small transitions in wear were observed (Fig. 38b). For 0.1 m/s sliding, a transition from $< 1 \text{ mm}^3\text{km}^{-1}$ to

almost $3 \text{ mm}^3\text{km}^{-1}$ material loss was observed between 20 N and 40 N. For 0.3 m/s sliding, a 3x change in wear rate was observed between 20 N and 30 N. For 0.6 m/s, a rapid increase in wear occurred between 12 N and 25N.

Depending on the load and sliding speed, wear volume reductions between 3.5x and 23x could be realized by low temperature carburization.

6.3.3 Wear Debris and Wear Scar Analysis

6.3.3.1 0.1 m/s Sliding Speed

At a sliding speed of 0.1 m/s and an applied load of 4 N, the wear debris of carburized 316L consisted primarily of particles below $10 \mu\text{m}$ in size and a small number of $120 \mu\text{m}$ or smaller flake-type debris (**Fig. 39c**). While these flakes were fairly large, their surfaces were textured and contained a high level of oxygen, as revealed by XEDS (**Fig. 40**). This suggests that prior to delamination fracture, sufficient time and frictional heating were available to form a protective oxide layer on the carburized 316L surface, which is characteristic of oxidative wear under low sliding speeds (7). In contrast, non-treated 316L wear debris generated under the same test conditions consisted of much more wear flake debris below $120 \mu\text{m}$ in size with no oxide scale (**Fig. 39a**). Clearly, a protective oxide film was unable to form prior to wear fracture.

When the applied load was increased to 40N, a drastic difference in wear performance was revealed. Carburized 316L wear debris consisted primarily of particles less than $5 \mu\text{m}$ in size and some flakes below $60 \mu\text{m}$ (**Fig. 39d**). In comparison, non-treated 316L wear debris generated under these conditions contained enormous flake-

like debris, up to 300 μ m or more in size (**Fig. 39b**). The presence of such a high density of massive flake debris is indicative of severe wear.

Three dimensional LCSM reconstructions of the wear scars obtained under these test conditions further illustrate the superior wear performance of carburized 316L; the non-treated 316L wear scars are much deeper and wider than the carburized wear scars (**Fig. 41**).

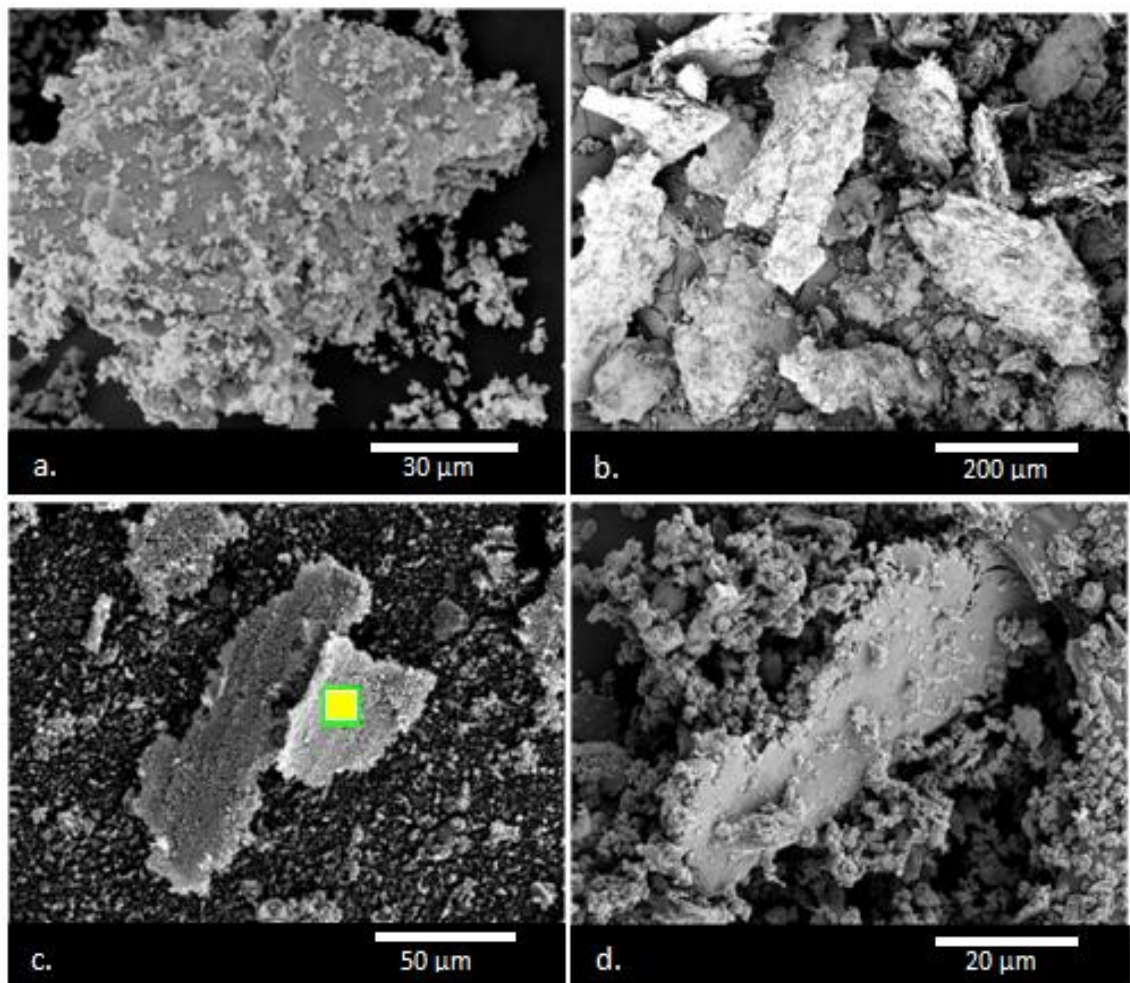


Figure 39 Wear debris generated at 0.1 m/s comparing (a.) Non-treated 316L under 4N applied load, (b.) Non-treated 316L under 40N applied load, (c.) Carburized 316L under 4N applied load; highlighted area refers to Figure 6, (d.) Carburized 316L under 40N applied load.

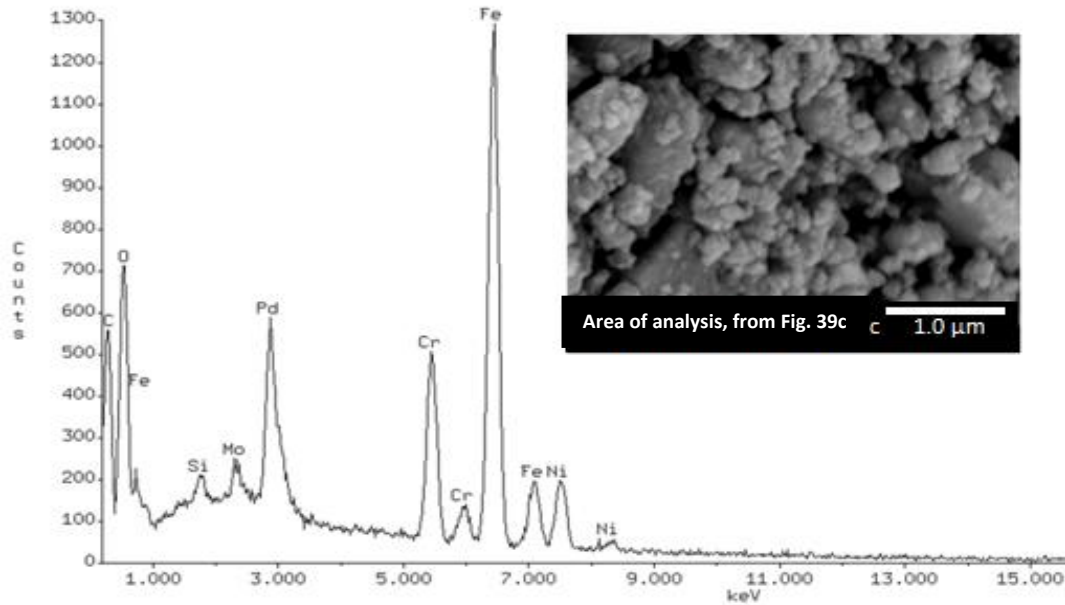


Figure 40 EDS spectrum showing the high oxygen level present on carburized flake debris resulting from sliding under a 4 N load at 0.1 m/s; the inset is a magnified image of the oxide layer highlighted in Fig. 5c.

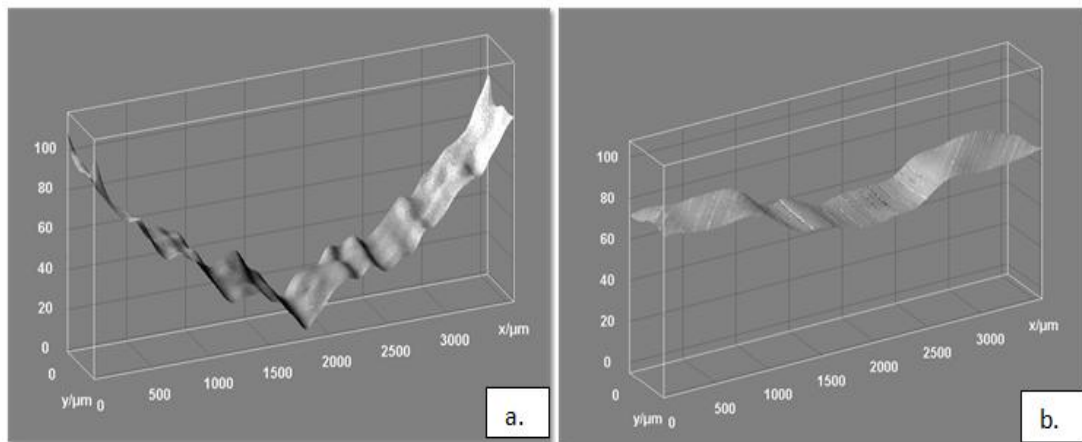


Figure 41 Wear scars generated under 40 N applied load and 0.1 m/s for (a.) Non-treated 316L, and (b.) Carburized 316L

6.3.3.2 0.3 m/s Sliding Speed

No oxide scales were observed on flake wear debris generated at 0.3 m/s from carburized or non-treated 316L. Once the load was increased to 40 N, however, a drastic difference in wear performance was revealed. Under the higher load conditions, carburized wear debris consisted of particles less than 10 μm and flakes below 40 μm in

size (**Fig. 43d**). In contrast, non-treated 316L exhibited severe wear, giving rise to a high density of massive flake debris up to 300 μm or more in size (**Fig. 43b**).

Carburized 316L wear scars were much smaller and shallower than non-treated 316L under these conditions (**Fig. 42**).

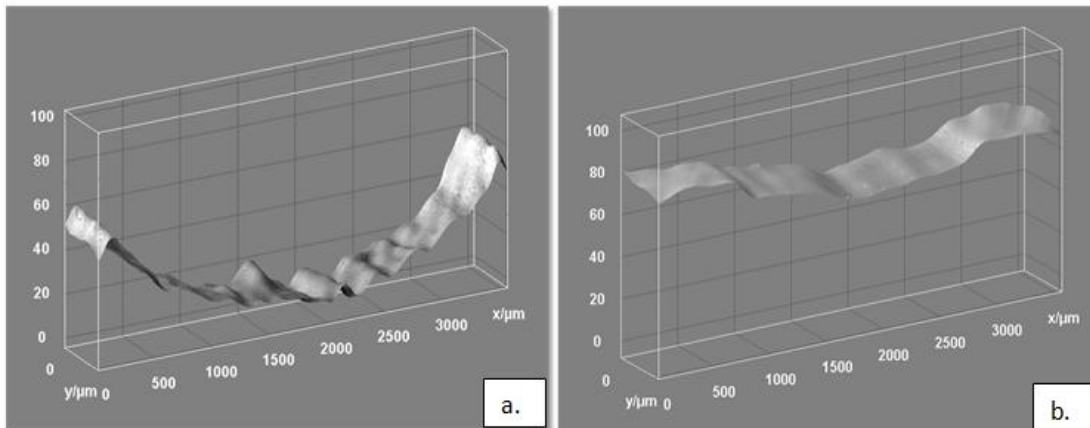


Figure 42 Wear scars generated under 40 N applied load and 0.3 m/s sliding (a.) Non-treated 316L (b.) Carburized 316L

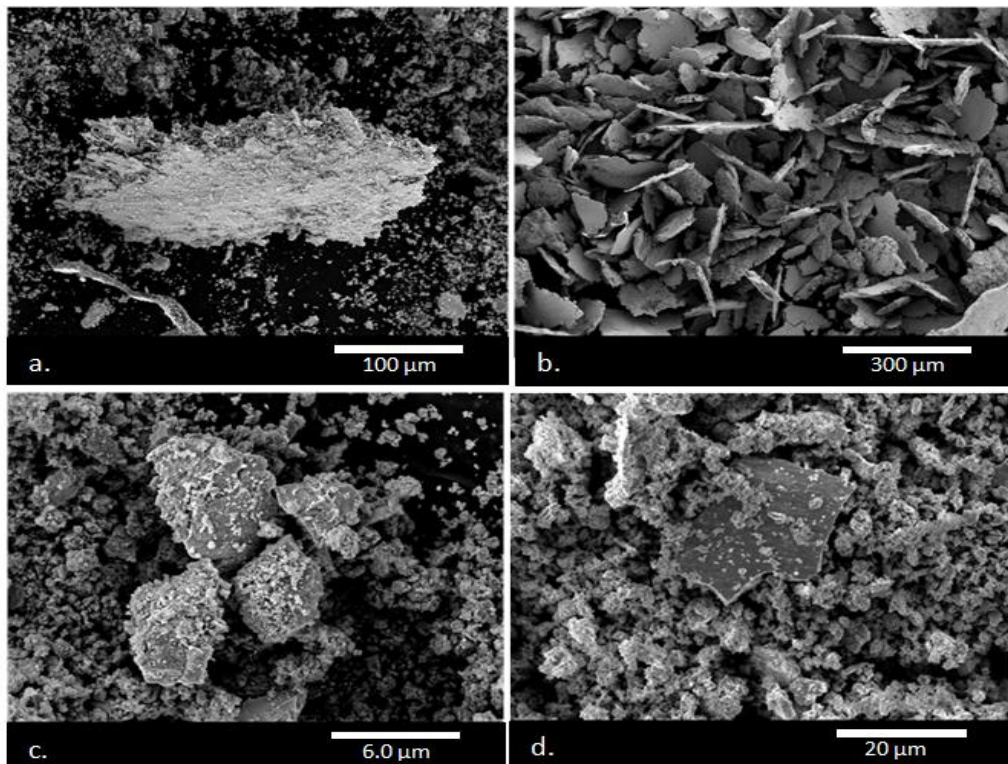


Figure 43 Comparison of wear debris generated at 0.3 m/s sliding speed for (a.) Non-treated 316L under 4 N applied load, (b.) Non-treated 316L under 40 N applied load, (c.) Carburized 316L under 4 N applied load, and (d.) Carburized 316L under 40 N applied load

6.3.3.3 0.6 m/s Sliding Speed

Wear debris generated by sliding at 0.6m/s under an applied normal load of 4N resulted in small wear particles and large severe wear flakes for non-treated 316L (**Fig. 44a**). Carburized 316L generated debris particles similar in size that were accompanied by much smaller flake debris, below 30 μm in size (**Fig. 44c**). Once the applied load was increased to 40N, wear debris generated from both carburized and non-treated 316L consisted of wear flakes less than 50 μm in size and particles below 10 μm in size (**Fig. 44b, 44d**).

The wear scars resulting from these test conditions revealed a very high degree of plastic deformation on the non-treated 316L disks (**Fig. 45a, 46a**), whereas the carburized disk scars showed much less plastic deformation (**Fig. 45b, 46b**). This results from the increased yield stress of the hardened carburized case, which attenuates traction-induced plastic deformation.

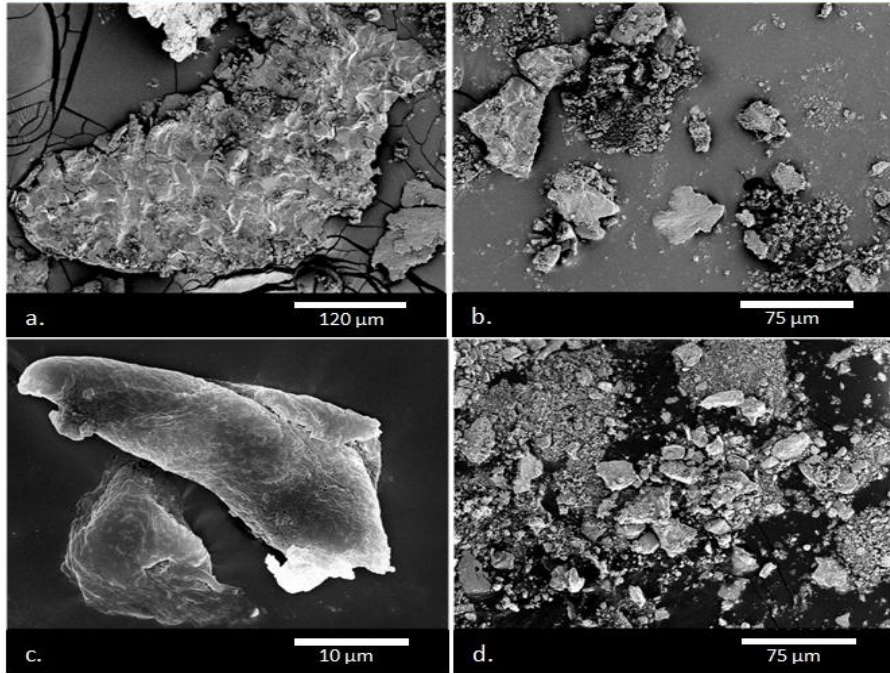


Figure 44 Comparison of wear debris generated at 0.3 m/s sliding speed for (a.) Non-treated 316L under 4 N applied load, (b.) Non-treated 316L under 40 N applied load, (c.) Carburized 316L under 4 N applied load, and (d.) Carburized 316L under 40 N applied load

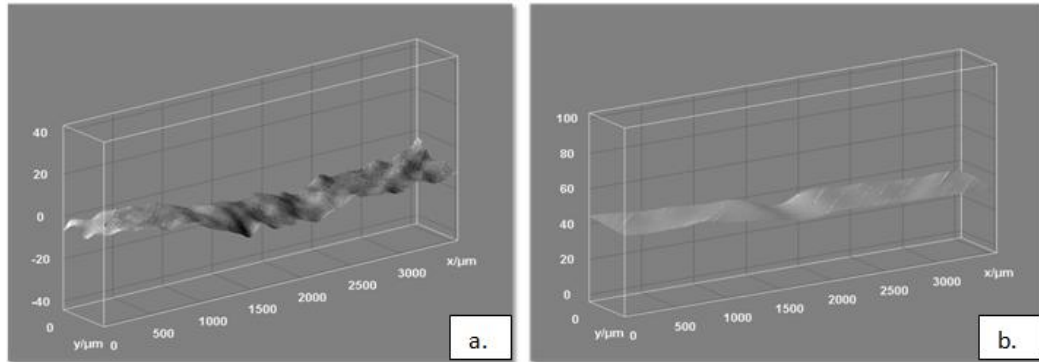


Figure 45 Wear scars generated under 40 N applied load and 0.6 m/s sliding for (a.) Non-treated 316L, and (b.) Carburized 316L

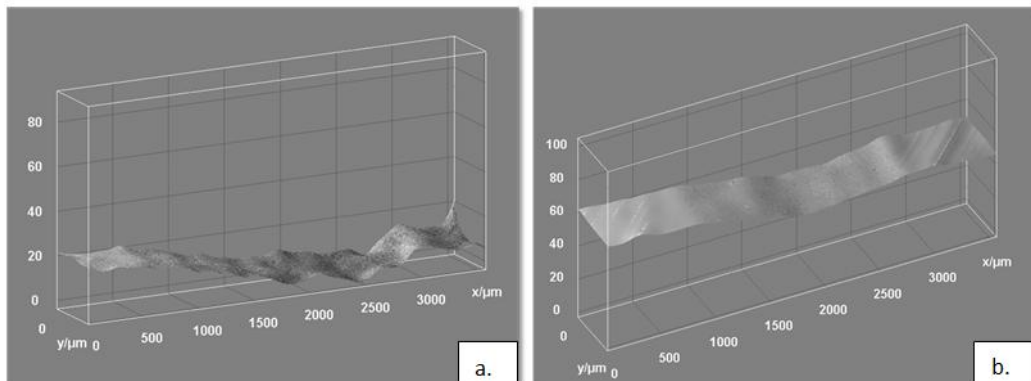


Figure 46 Wear scars generated under 40 N applied load and 0.6 m/s sliding for (a.) Non-treated 316L, and (b.) Carburized 316L

6.5 Wear Maps

The experimental data were used to determine the six coefficients describing wear volume using a least squares linear regression analysis. This analysis revealed that only the α and β coefficients describing the load and the load-velocity interaction, were statistically relevant, and are shown in **Table 5**; statistical correlates showing the goodness of fit variables are shown in **Figure 47**. These coefficients could then be used to generate the contour plots shown in **Figure 48**, which illustrate the effects of load and velocity on the wear of the two materials. As expected, increasing the applied load increased the wear of non-treated 316L much more rapidly than was the case for the carburized material. The effect of applied load on wear was roughly ten times less for carburized 316L, as indicated by comparing the α constants obtained from the regression analysis. Similarly, the effect of the interaction between applied load and sliding velocity was ten times greater for non-treated 316L. Because the β coefficient for the interaction term is negative, the predicted wear volume decreases as sliding speed increases, and results in the curvature of the contours in each plot.

	Non-treated 316L		Carburized 316L	
	α	β	α	β
Coefficient	0.642	-0.789	0.070	-0.066
P-statistic	2.29E-6	1.08E-3	9.68E-8	5.16E-3
R^2	0.92		0.92	

Table 5 Empirical wear model constants obtained by regression of pin-on-disk data for carburized and non-treated 316L stainless steel

Combining the wear debris and wear scar observations with the contour plots of the wear maps reveals drastic differences in wear mechanisms under various test conditions (**Fig. 48**). This clearly illustrates that the mild wear regime for 316L stainless steel can be significantly extended to higher applied loads and greater sliding speeds by low temperature carburization.

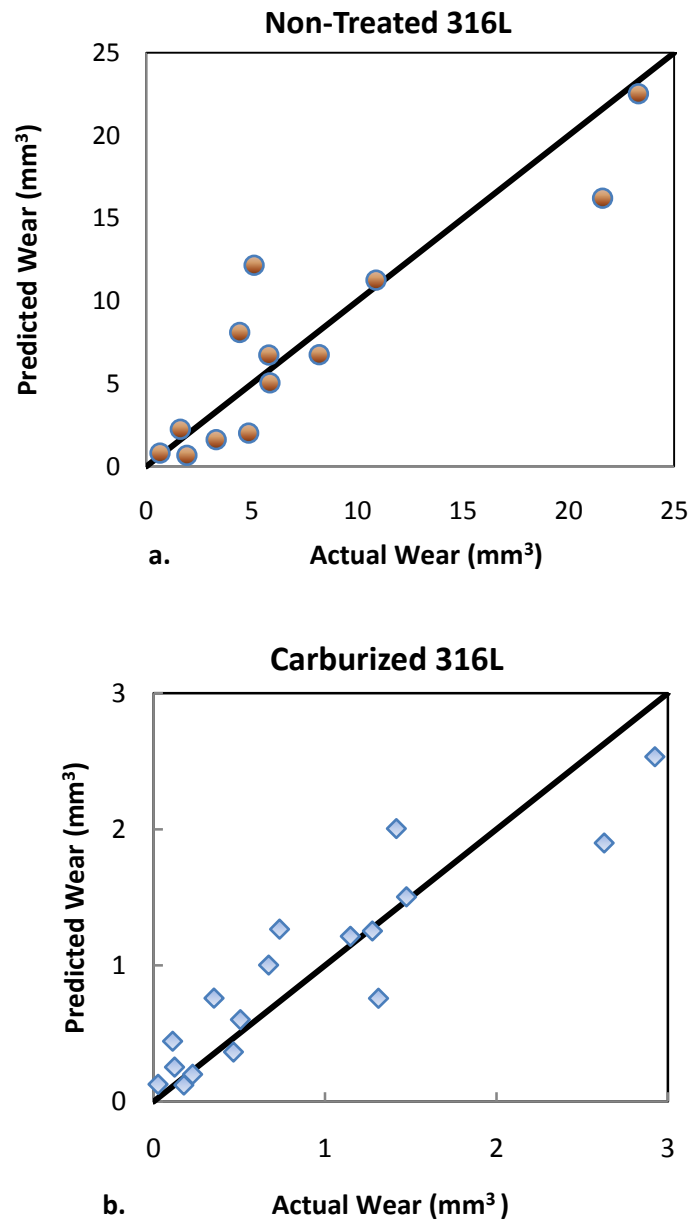


Figure 47 Parity plots showing the goodness of fit for the empirical model developed from pin-on-disk data for (a.) Non-treated 316L stainless steel, and (b.) Carburized 316L

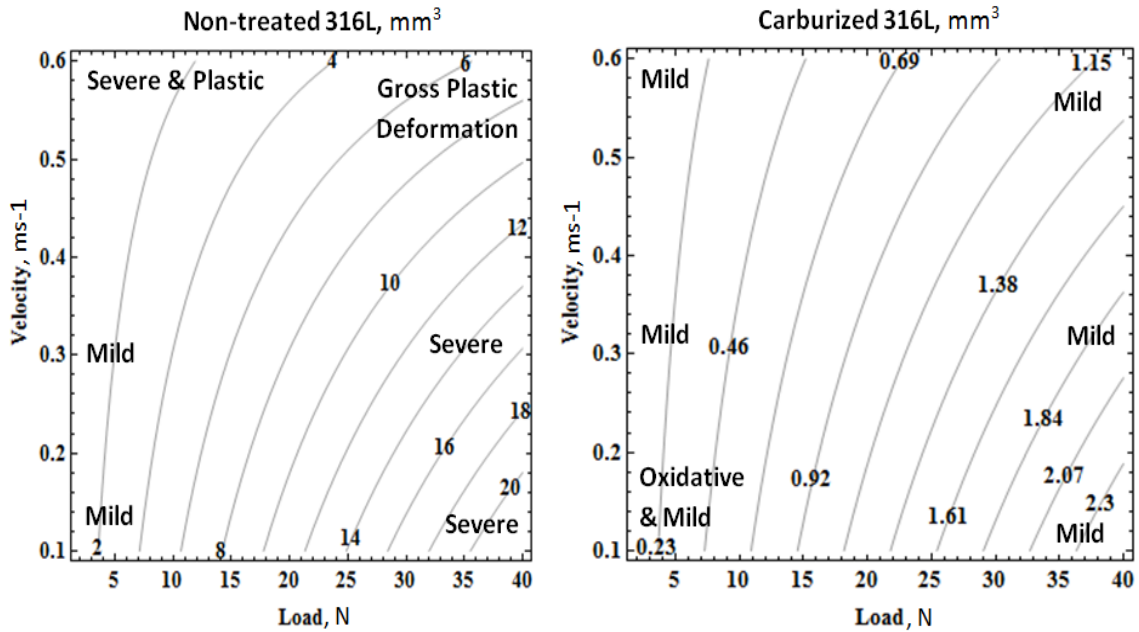


Figure 48 Wear maps comparing the observed dry sliding wear behavior under various loads and sliding speeds for (a.) Non-treated 316L, and (b.) Carburized 316L; The contour lines represent the volume of material lost by wear (mm^3) for the various conditions

6.6 Wear Maps of Carburized 316L, Summary and Conclusions

Severe wear of low temperature carburized 316L was not observed during dry sliding against alumina under the range of loads and sliding speeds studied. In contrast, non-treated 316L showed severe wear when sliding under high loads at speeds of 0.3 m/s or less, and when sliding under low loads at 0.6 m/s. At the highest sliding speed, 0.6 m/s, non-treated 316L showed extensive plastic deformation throughout the wear scar, while carburized 316L showed much less plastic deformation. This was a result of frictional heating which can significantly reduce the yield stress of the sliding surface, resulting in a greater degree of plastic deformation. Carburized 316L resisted such extensive plastic deformation under these conditions due to the high yield stress of the carburized region. Depending on the load and sliding speed, wear reductions between

3.5x and 23x were realized by low temperature carburization. This improvement in wear resistance is attributed to the increased yield stress and appreciable compressive residual stress of the hardened carburized case. The increased yield stress of the carbon-rich case provides additional resistance to plastic deformation-related wear mechanisms such as abrasive wear, cutting, and ploughing. In addition, the elevated yield stress of the case results in an increased resistance to the tractional shear stresses applied during sliding. The large magnitude of compressive residual stress within the hardened region, >2.0 GPa, diminishes the effect of stress concentrations at or near the surface during sliding. These stresses also increase the fatigue resistance of the material by inhibiting crack initiation and growth, providing additional protection to cyclic wear processes. This effect was evident by the observed flake wear debris, which was consistently more numerous and greater in size for non-treated 316L under all test conditions.

The benefits of low temperature carburization are maintained over a wide range of dry sliding conditions. The treatment extends the mild wear regime of 316L stainless steel to more extreme tribological conditions that would typically be considered too harsh for this material. Thus, the low temperature carburization process applied to austenitic stainless steel grade 316L significantly extends the useful range of tribological applications for this material. Based on these results, carburization will likely have a similar affect with other alloys provided that a similar surface hardness and residual stress depth profile are obtained.

7.0 Relationship of the Case Hardened Region's Properties to Wear Resistance

7.1 Background and Motivation

Low temperature carburization greatly enhances the wear resistance of 316L austenitic stainless steel under various conditions and when sliding against materials of various hardnesses as shown by Experiment 1 and 2. These experiments, and the work of Blau and Qu (19), examined the tribological performance of fully carburized 316L, which generally consists of a case hardened region of approximately ≈ 30 microns, a surface carbon concentration of approximately 12 at.%, and an approximate surface hardness of 12 GPa (5). These properties were achieved by processing for a full low temperature carburization cycle, which is typically more than twenty hours in length for 316L. The carburization process parameters, including treatment time, temperature, and environment, are directly related to the surface hardness and thickness of the hardened region; thus different treatment parameters may result in different degrees of wear resistance improvement. To fully understand the improvements in wear resistance achieved by low temperature carburization, a better understanding of the fundamental relationship between surface hardness, case depth, and wear resistance is needed. The objective of this experiment was to characterize the relationship between wear resistance and the properties of the case hardened layer. This was done by testing the wear resistance of carburized 316L disks containing case hardened regions of varying surface hardness and depth. A greater understanding of this relationship could enable customized treatment times for specific tribological applications; for example a

longer treatment time for a deep hardened region with maximum surface hardness and excellent wear resistance, or shorter (and thus less expensive) treatment time for an intermediate case thickness, surface hardness, and wear resistance for less demanding tribological applications.

7.2 Materials and Methods

AISI 316L disks of 1 inch diameter and 0.25" thickness (Source: Penn Stainless Inc.) were carburized at low temperature by Swagelok Co. Electropolishing was performed by Swagelok Co. following full carburization to remove layers of the case hardened region; layers of 5, 10, 15, 20, and 25 micron target thickness were removed. The resulting disks contained hardened regions of approximately 10, 15, 18, 25, 30, and 32 microns thick with varying surface hardness levels (**Fig. 49, Fig. 50**). The Vickers microhardness of each disk was tested using a Buehler microhardness indenter and a 50 g load (**Fig. 49**).

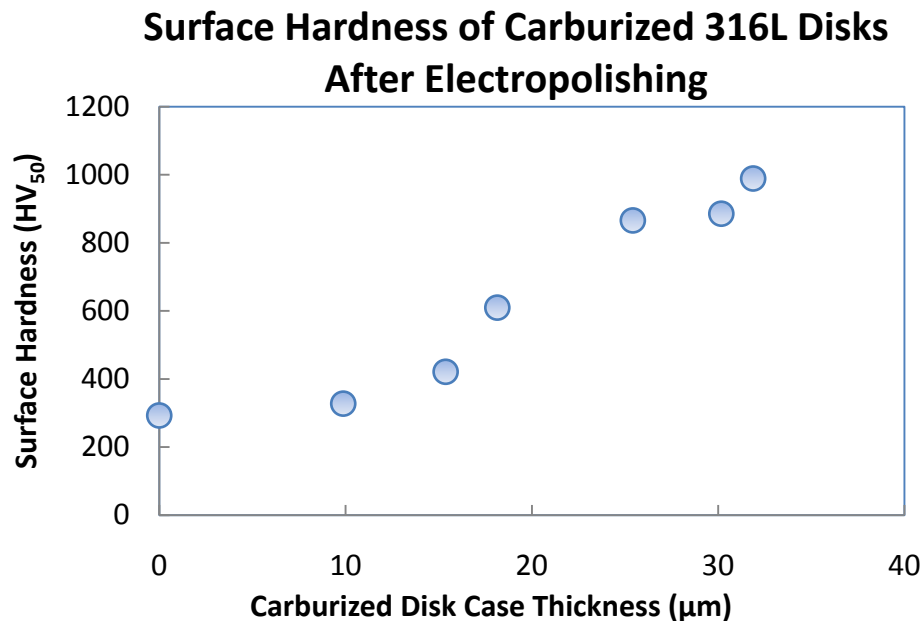


Figure 49 Carburized 316L disk surface hardness (Vickers, 50 g load) after electropolishing



Figure 50 Carburized 316L of varying surface hardness and case depths of (a.) 10 μm, (b.) 15 μm, (c.) 18 μm, (d.) 25 μm, (e.) 30 μm, and (f.) 32 μm

The surface hardness of low temperature carburized 316L is known to be directly related to the concentration of carbon dissolved in the austenite matrix (5). The carbon concentration depth profile of the fully carburized 316L disks used in this study was measured by Swagelok Co. using Glow Discharge Optical Emission Spectroscopy (GDOES) (Fig. 51). As shown by **Figure 51**, the carbon concentration is highest at the

surface, approaching ≈ 15 at.%, and reduces to below 0.2 at.% in the disk's core. The paraequilibrium hardened austenitic region extends roughly 32 microns below the surface as shown by the etched microstructure (**Fig. 50f**), which is in disagreement with the GDOES carbon profile which indicates the carbon rich region is greater than 40 microns thick. The inaccuracy of the GDOES profile is likely due to carbon measurement errors at large depths below the surface.

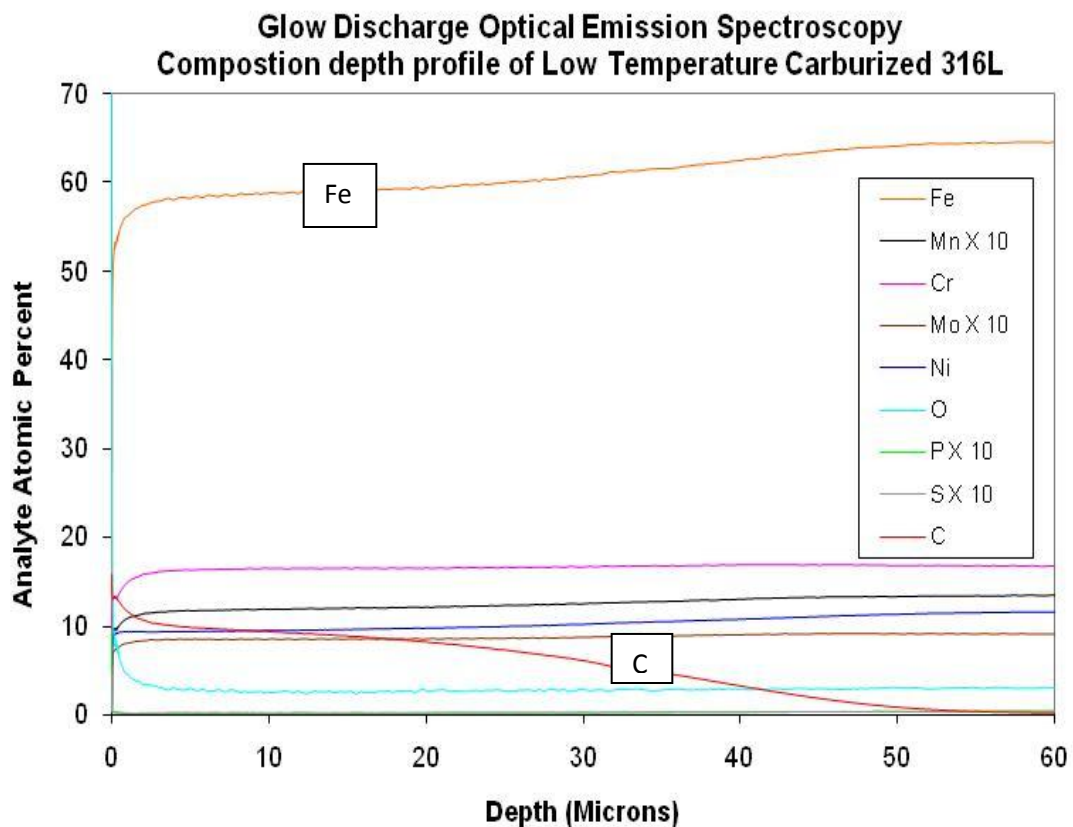


Figure 51 GDOES composition depth profile of low temperature carburized 316L, note the inaccuracy of the carbon rich region compared to that observed by Microstructural analysis (Fig. 50). (GDOES figure provided by Swagelok Co.)

The pin-on-disk test method was used to study the friction and wear behavior of each disk when sliding against an Al_2O_3 ball. The Case Western Reserve University Department of Materials Science tribometer (CETR Inc. model UMT 2.0) was used to conduct the pin-on-disk tests in accordance with ASTM G99-05 (18). Two series of tests

were conducted, the first characterizing wear sliding at 0.1 m/s under a load of 5 N; conditions in which both non-treated and carburized 316L were observed to exhibit mild wear as shown by Experiment 2. The second set of tests were conducted under an applied load of 40 N sliding at 0.1 m/s; conditions in which non-treated 316L exhibits severe wear and carburized 316L exhibits mild wear, as shown by Experiment 2. These test conditions were chosen to identify potential differences in the relationship between the characteristics of the case hardened region and the resulting wear resistance under different sliding conditions. The experimental conditions for each test are shown in **Table 6**. Note that the total sliding distance for the 40 N series of experiments was limited to 100 m. This was done to avoid complete wear through of the case hardened region when sliding under high load, which helped to ensure that the wear resistance of the various case hardened regions was observable.

Case Thickness of Carburized 316L Disk (μm)	Load (N)	Speed (m/s)	Total Sliding Distance (m)	Track Diameter (mm)	Room Temp. ($^{\circ}\text{C}$)	Relative Humidity (%)
0	5	0.1	250	10	29	61
10	5	0.1	250	10	26	67
15	5	0.1	250	10	30	62
18	5	0.1	250	10	31	58
25	5	0.1	250	10	32	59
30	5	0.1	250	10	33	63
32	5	0.1	250	10	30	60
0	40	0.1	100	10	27	61
10	40	0.1	100	10	27	63
15	40	0.1	100	10	28	63
18	40	0.1	100	10	26	61
25	40	0.1	100	10	25	59
30	40	0.1	100	10	26	66
32	40	0.1	100	10	28	61

Table 6 Case Properties vs. Wear pin-on-disk test conditions

7.3 Results and Discussion

7.3.1 Wear Results

The wear resistance of carburized 316L was strongly related to the surface hardness of the carburized region and was dependent on the applied normal load. Under an applied load of 5 N, the fully carburized disk, $\approx 32 \mu\text{m}$ case depth and $\approx 990 \text{ HV}$ surface hardness, achieved the greatest wear resistance. However, the wear resistance

of disks containing hardened regions of 20 μm or more (>610 HV) were close to that of achieved by the maximum hardened region (**Fig. 52**). Once the disk surface hardness fell below ≈ 420 HV, wear rapidly increased (**Fig. 53**). This suggests that a shorter treatment time resulting in a case thickness of ≈ 18 μm and a surface hardness of ≈ 610 HV will result in a wear resistance improvement that is only $\approx 25\%$ less than that obtained by “full” carburization (when sliding under these conditions). These results also indicate that if a critical level of surface hardening is not reached, (roughly 420 HV under these conditions), significant wear resistance improvements will not be realized.

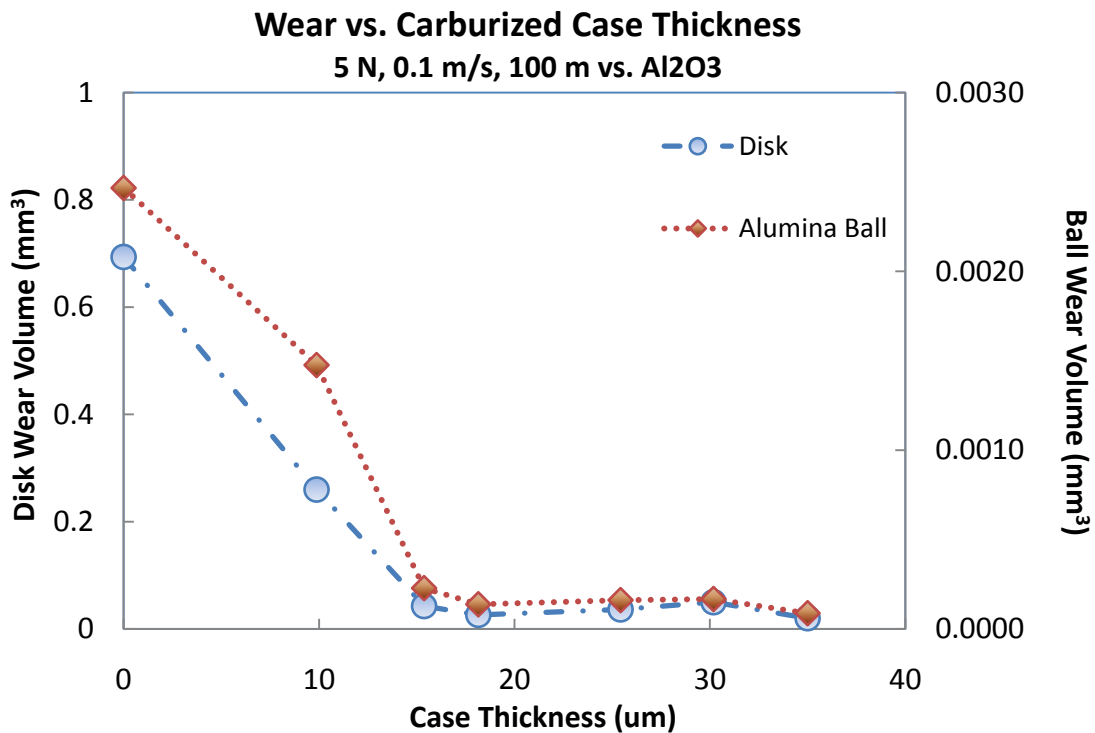


Figure 52 Wear vs. Case Thickness for carburized 316L sliding at 0.1 m/s against alumina under a 5 N applied load

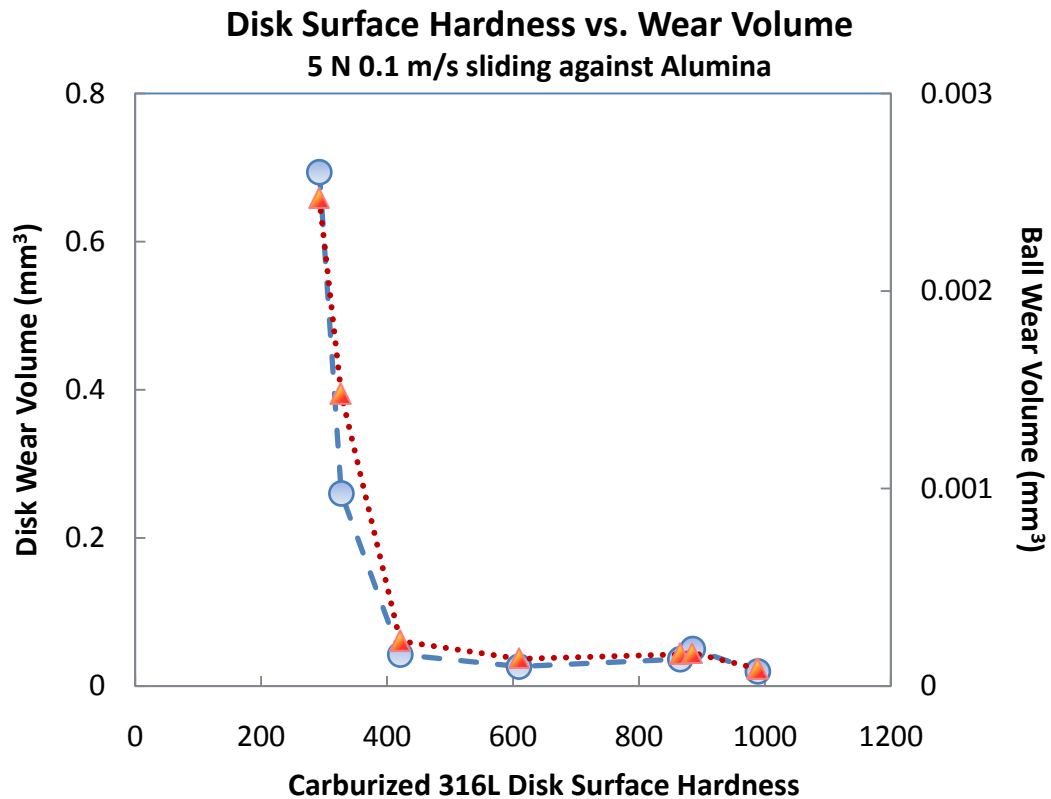


Figure 53 Influence of carburized 316L surface hardness on wear when sliding against alumina under an applied load of 5 N at 0.1 m/s

When the applied normal load was increased to 40 N, the relationship between the characteristics of the case hardened region and wear resistance was slightly different. The non-treated disk was found to have the least wear resistance, and the fully carburized disk (≈ 32 μm case depth, ≈ 990 HV hardness) was found to have $\approx 6x$ greater wear resistance (**Fig. 54**). Surprisingly, samples with a case thickness of ≈ 18 μm and a surface hardness of ≈ 610 HV showed even less wear than the fully carburized disk, improving wear resistance by $\approx 17x$. Interestingly, the minimum amount of alumina ball wear also occurred for sliding against the carburized 316L disk of ≈ 18 μm case depth and ≈ 610 HV surface hardness, and wear of the alumina ball counterface increased once the hardness and case depth of the carburized disk exceeded this level. Once the disk

surface hardness dropped below ≈ 600 HV, the wear rate rapidly increased (**Fig. 55**). This suggests that, under these sliding conditions, an optimum level of disk hardness and case thickness exists, which results in minimum wear of the ball and disk. Then, as the thickness of the case hardened region increases and becomes harder, wear of the alumina counterface increases, resulting in accelerated disk wear. Below a critical level of surface hardness and case thickness, the wear rate of the disk markedly increases. This indicates that for specific applications, the carburization process could be optimized to achieve minimum disk and system wear rates by tailoring the hardness and depth of the case hardened region, and that the maximum achievable surface hardness and case depth may not necessarily give the minimum wear rate for certain tribological applications. The results also show that if carburization does not achieve a certain minimum case depth and surface hardness, significantly improved wear resistance of the base alloy will not be realized.

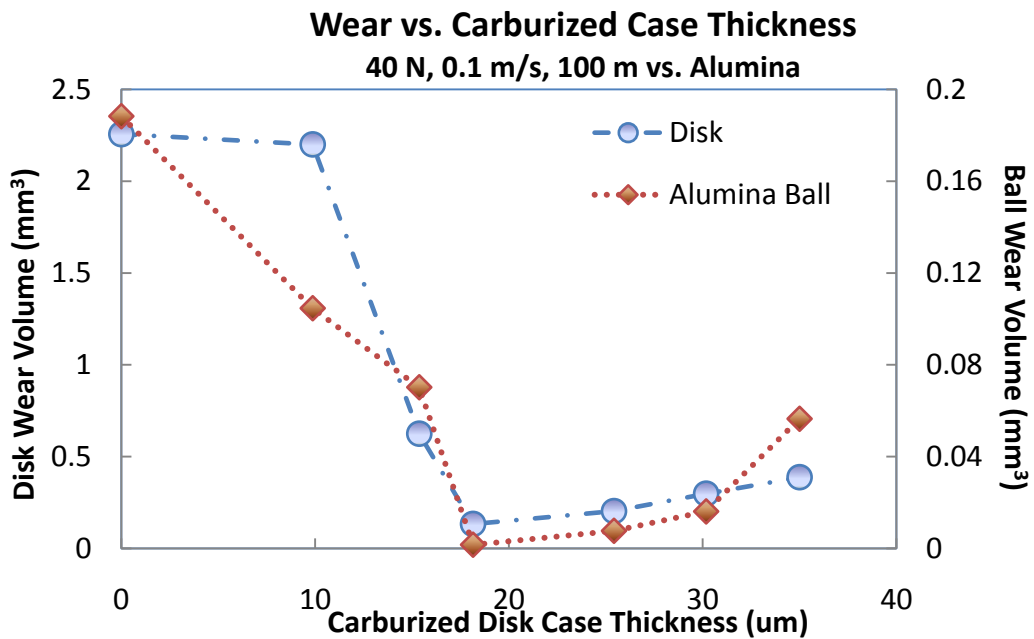


Figure 54 Disk and ball wear for an alumina ball sliding at 0.1 m/s under an applied load of 40 N against carburized 316L disks of various case thicknesses and surface hardnesses

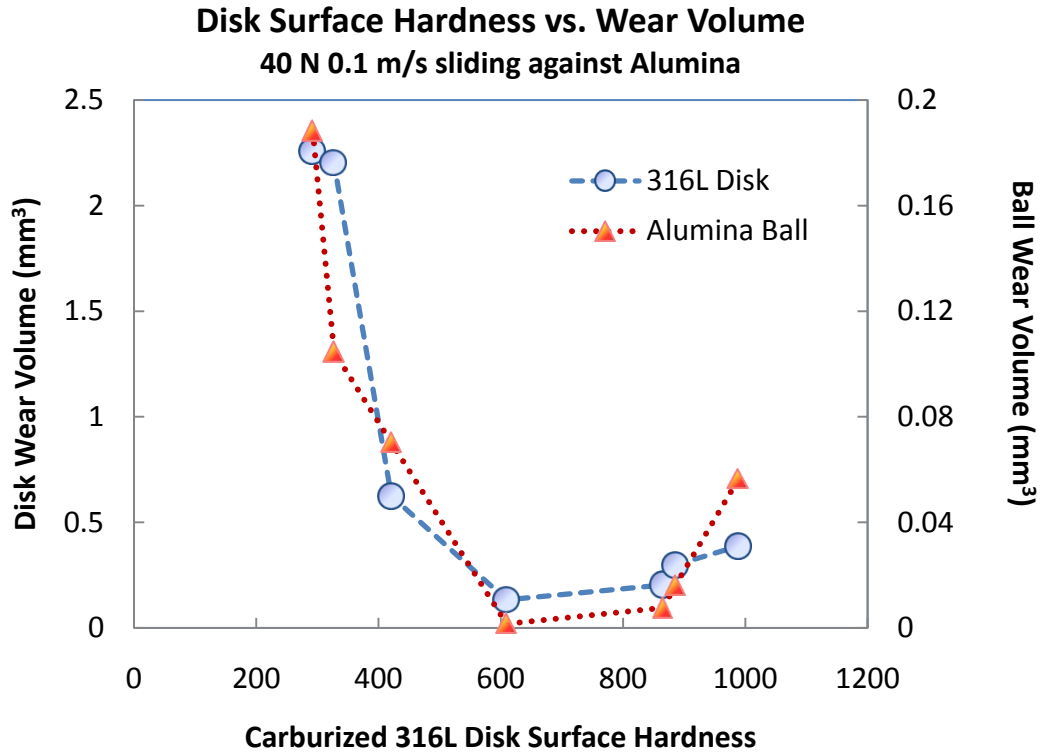


Figure 55 Influence of carburized 316L surface hardness on wear when sliding against alumina under an applied load of 40 N at 0.1 m/s

The marked wear increase as the thickness and hardness of the carburized region was reduced beyond a critical point is due (at least in part) to complete wear through of the case hardened region. This hypothesis is supported by the observed wear scar depths (**Fig. 56**), which sharply increase once the case hardened region has been worn through. The transition to greater wear is observed for case hardened regions less than $\approx 18 \mu\text{m}$ when sliding under a 40 N load, and for case hardened regions less than $\approx 15 \mu\text{m}$ when sliding under a 5 N applied load. The difference in the transition point for these two sliding conditions is due to the greater wear rate when sliding under a 40 N load.

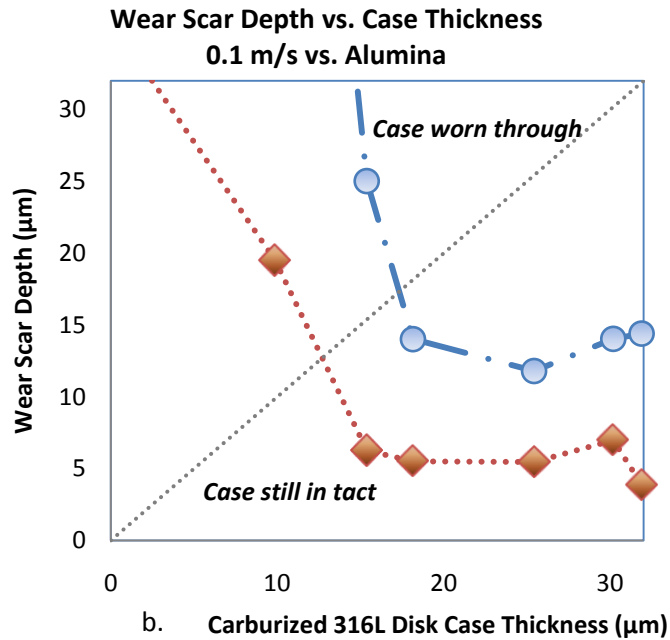
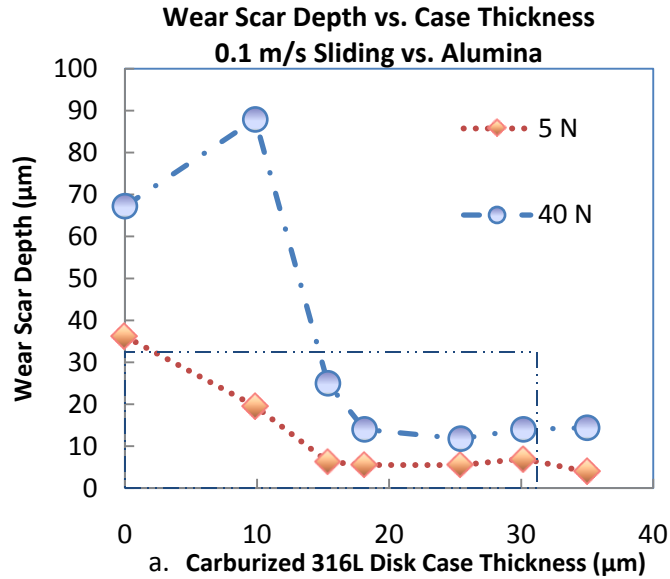


Figure 56 (a.) Disk wear scar depth vs. case thickness of carburized 316L disks for 0.1 m/s sliding against an alumina ball, and (b.) enlarged view of selected region from 56a, illustrating the sharp change to non-treated like wear once the case hardened region is worn through

7.3.2 Friction Results

The coefficient of friction was found to vary with respect to the properties of the case hardened region. When sliding under a 5 N applied load, the steady state COF of non-treated 316L was approximately 0.71. The COF increased to between 0.77 and 0.81

for carburized 316L disks with case thicknesses between 10 and 30 μm , and then decreased to 0.66 for the fully carburized disk which had a case thickness of approximately 32 μm and a surface hardness of ≈ 990 HV (**Fig. 57**). Sliding under a 40 N load, the COF had a different relationship with the case thickness and surface hardness of carburized 316L. Minimum COF was observed for non-treated 316L, ≈ 0.45 , which increased to ≈ 0.48 for carburized 316L with a case depth of ≈ 18 μm , and increased further to 0.52 for the maximum case hardened sample (**Fig. 57**). These results indicate that for dry sliding against alumina, the steady state level of friction varies with the properties of the case hardened region, and that the optimum combination of wear resistance and friction might be achieved for an intermediate level of surface hardening and surprisingly not for the maximum level of hardening. For example, from this experiment, sliding against alumina under a 40 N load, carburized 316L with a case depth of ≈ 18 μm and surface hardness of ≈ 610 HV achieved a ≈ 17 x improvement in wear resistance while increasing friction by only $\approx 8\%$, while the deepest and hardest case achieved only a ≈ 6 x increase in wear resistance with a $\approx 15\%$ increase in friction.

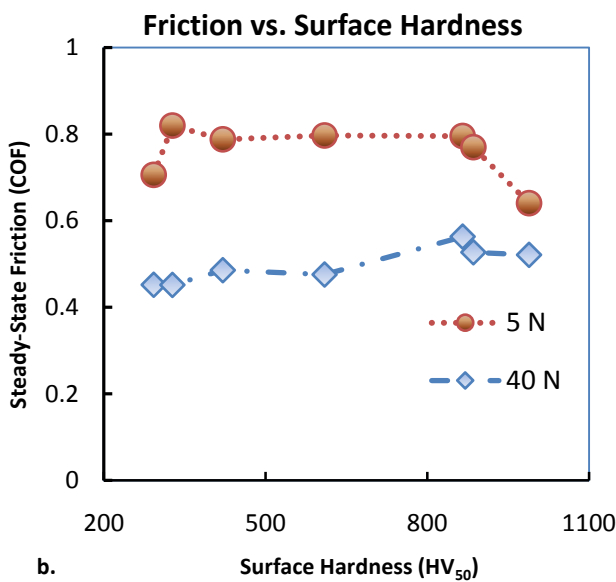
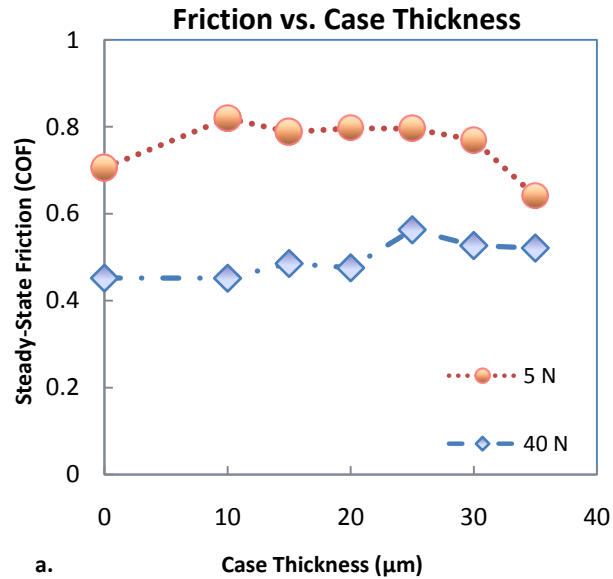


Figure 57 Steady state friction for dry 0.1 m/s sliding of an alumina ball vs. carburized 316L disks; (a.) friction vs. thickness of carburized region after electropolishing, and (b.) friction vs. surface hardness of carburized disk after electropolishing

7.4 Experiment 3 Summary

The wear resistance of carburized 316L sliding against an alumina ball was directly related to the properties of the case hardened layer of the disk. The thickness and hardness of the carburized region strongly affect wear resistance. Under a load of 5 N, maximum wear resistance was achieved for the carburized disk containing the

maximum case thickness and surface hardness; however, disks containing an intermediate level of hardening have nearly the same wear resistance as the fully carburized disk. Wear sharply increased once the carburized disk surface hardness fell below ≈ 400 HV. This was a result of the case hardened region becoming completely worn through, thus eliminating the benefits of carburization.

When sliding under a load of 40 N, the maximum disk and system wear resistance was achieved for the ≈ 18 μm thick case hardened region, which had a surface hardness of ≈ 610 HV. Once the carburized disk surface hardness increased beyond ≈ 860 HV, wear of the system significantly increased. The maximum case depth and surface hardness achieved with full carburization resulted in increased alumina ball and carburized 316L disk wear, which is likely a result of an increase in alumina wear debris particles that cause third body abrasive wear on the system. Wear rate sharply increased once the thickness of the case hardened region fell below ≈ 18 μm and ≈ 610 HV. This sudden transition in wear rate was again a result of complete destruction of the case hardened region of the wearing surface.

The sudden increase in wear rate once surface hardness falls below a critical level can be explained by a transition to more severe wear mechanisms; this is a direct result of complete wear through of the case (**Fig. 56**). Under these conditions, wear quickly destroys the carburized region before the test is complete and a transition to essentially non-treated wear behavior ensues. Once the case hardened region has been destroyed by wear, the benefits of increased surface hardness and residual compressive

stress are annihilated causing contact conditions to suddenly change and wear to increase. Because of this, the transition to non-treated wear behavior is dependent on the sliding distance, contact stress, and the properties of the “expanded austenite” region. For example, a very thick case hardened region would take a longer time to wear through, thus delaying the transition to greater wear rates.

The results show that the optimum disk, ball, and system wear resistance may not always be achieved with the maximum surface hardness and case depth attainable by low temperature carburization. Under certain conditions, intermediate surface hardening may result in equal or even greater wear resistance than that achieved by maximum hardening, which was illustrated by the results obtained for sliding under an applied load of 40 N. This is because the surface hardness achieved by low temperature carburization is so great that wear of a hard counterface such as alumina will increase, resulting in abrasive third-body wear debris. This abrasive debris tumbles between the sliding surfaces, introducing the abrasive wear process to the system and accelerating system wear. In this case, intermediate hardening of 316L optimizes system wear by limiting wear of the alumina counterface while also providing enough wear resistance for the 316L.

Steady state friction was also found to vary with the surface hardness of the case. While no definitive trend regarding the magnitude of friction coefficient could be established, friction was greater for carburized materials of any surface hardness than that of non-treated 316L under all test conditions. This is consistent with previous

observations made by Qu et al (9), as well as observations made in section 6.0 of this paper. Furthermore, depending on sliding conditions, an intermediate level of hardening may result in considerably less friction than maximum hardening as shown by **Fig. 57**. Thus for specific applications, the properties of the case hardened layer could be tailored to result in minimized wear of the tribological system, while also limiting the friction increase that results from low temperature carburization. This is consistent with the hypothesis that the high yield strength of carburized 316L is responsible for the increase in friction, and thus a carburized 316L sample of lower hardness should have lower friction under the same conditions. Tailoring the properties of the hardened region can be accomplished by adjusting carburization process parameters such as temperature, carbon activity, and treatment time; for example a shorter (and thus less expensive) treatment time could be utilized to obtain a hardened region of less depth and hardness than that achieved through a standard full carburization treatment cycle. While less than maximum hardening may result in optimized wear for certain applications, if a critical level of hardening is not met, little to no wear resistance improvement will be realized due to destruction of the case during sliding.

8.0 Discussion of Experimental Results

According to the Von Mises and Tresca yield criterion, plastic deformation will occur during sliding when tractional shear stresses exceed the shear strength of the sliding material. Thus, carburized 316L has a great advantage over non-treated 316L; the increased hardness suggests a greatly increased surface yield stress, and corresponding greatly increased shear strength. Furthermore, abrasive wear mechanisms, in which wear and plastic deformation occur when hard particles penetrate the surface of softer materials, are also attenuated by the high surface hardness and yield strength of the carburized layer. These advantages were evident by the wear resistance improvement when sliding against hard materials, and by the lesser degree of plastic deformation observed when sliding at high speeds and under high stress.

Another advantage imparted by low temperature carburization is that the high levels of compressive residual stress within the carburized case inhibit fatigue wear mechanisms. Fatigue is known to be suppressed by surface compressive residual stresses (14), and the enhanced fatigue life of carburized 316L has been observed under fully reversed ($R=-1$) cyclic loading (25). This compressive residual stress should also inhibit fatigue wear mechanisms such as delamination; the process by which cyclic load-induced cracks initiate and propagate beneath the surface, resulting in flake-like wear debris. This delamination process is a competition between ratcheting failure and low cycle fatigue (13). The increased shear strength of the carburized layer will suppress strain accumulation (ratcheting), according to the ratcheting wear model discussed by

Kapoor (**Equation 16**), which is shown again below (13); here $\Delta\gamma$ is the increment of shear strain due to the applied cyclic stress, τ_{zx} is the maximum applied shear stress at a given subsurface depth caused by sliding or rolling contact, and k_{eff} is the effective yield stress of the tribolayer in pure shear, which is increased by low temperature carburization. This hypothesis is supported by the observation of a greater quantity and size of flake debris produced during the wear of non-treated 316L, particularly at higher loads where there is a clear and distinct change of wear mechanisms. When sliding under a high contact stress, the size and quantity of flake debris jumped drastically for non-treated 316L while debris from carburized 316L contained fewer and smaller wear flake debris. The characteristics of wear debris under these conditions support the hypothesis that carburized 316L resists crack nucleation and propagation leading to improved resistance to cyclic wear processes such as delamination.

(from Equation 16)

$$\Delta\gamma = 0.00237 \left(\frac{\tau_{zx}}{k_{eff}} - 1 \right)$$

Improved wear resistance was also observed for carburized materials with lower levels of hardening than is achieved through the standard Swagelok carburization process. Samples with approximately half the surface hardness and case thickness achieved by the standard “full” carburization treatment time resulted in $\approx 26x$ less wear than non-treated 316L, compared to a $\approx 35x$ reduction for the fully carburized material when sliding under a 5 N load against alumina. Once the normal load was increased to 40 N, the moderately hardened sample resulted in $\approx 17x$ less wear than non-treated 316L while the fully hardened sample resulted in $\approx 6x$ less wear. These results show that moderate hardening can result in greatly improved wear resistance, and under some

conditions may result in greater system wear resistance than that achieved by a standard carburization cycle. These results are significant because shorter treatment times could be used to obtain a moderate level of surface hardening. In turn, shorter treatment times may reduce the cost of carburization and expedite part turnaround. While it is clear that the improved yield stress, hardness, and compressive residual stress within the carburized region results in improved wear resistance, it is not clear why such a moderate level of hardening would result in nearly the same improvement in wear resistance of a fully carburized material.

A hypothesis addressing this phenomenon relates to the contact conditions at the interface of the sliding materials. Under the contact conditions experienced during dry sliding, high contact stresses arise at the interface of contacting asperities, resulting in plastic deformation. Once these stresses exceed a certain critical level, the apparent area of contact becomes equal to the real area of contact and significant frictional heating ensues, resulting in local loss of yield strength and severe wear behavior. Low temperature carburization limits the real area of contact in two ways; firstly by inhibiting plastic deformation as a result of the high hardness and yield stress of the carburized region, and secondly by offsetting tensile stresses as a result of the compressive residual stress within the case. Once the surface hardness and residual stress within the case-hardened region drop to a level that insufficiently limits real interfacial contact area, a transition to higher wear rate ensues. When the hardness and residual stress within the carburized region are above this critical level, wear is substantially limited. While this hypothesis explains the results observed in this project

for carburized disks of various case thickness and surface hardness, further evidence is needed due to the heavy dependence of results on test conditions when using the pin-on-disk test method; particularly because the sharp transition in wear observed was due to complete wear through of the case, which is directly dependent on the total sliding distance of the test.

9.0 Summary and Conclusions

The friction and wear behavior of 316L carburized at low temperatures by the Swagelok Co. was studied under many different conditions leading to several important findings. Firstly, it was observed that low temperature carburization greatly improves the wear resistance of 316L when sliding against hard materials such as WC, M50 tool steel, or Al_2O_3 , which is partly due to increased resistance to abrasive wear. This increased wear resistance is due to the enhanced surface hardness of the carburized material which reduces plastic-deformation driven wear mechanisms. This finding shows that low temperature carburization may enable the pairing of austenitic stainless steels with very hard materials for tribological applications as a result of the high yield stress of the carburized region, which inhibits the plastic deformation associated with abrasive wear.

Wear maps were generated showing that low temperature carburization significantly extends the mild wear regime and prevents severe wear under conditions that would typically be far too harsh for 316L stainless steel. Severe wear of non-treated 316L was observed under high applied loads and sliding speeds, while carburized 316L did not show severe wear under any of the conditions studied, due to the outstanding surface hardness and biaxial compressive stresses of the case-hardened region. These results suggest that low temperature carburization not only improves wear performance, but enables the use of stainless steels in tribological applications that were previously considered too severe for traditional non-treated stainless steel.

The relationship between the wear resistance of 316L carburized at low temperature and the characteristics of the hardened region were studied. The wear resistance of carburized 316L was dependant on the surface hardness and case thickness of the hardened region. This experiment revealed that under certain tribological conditions, a shorter treatment time that results in an “expanded austenite” region of modest depth and hardness may result in equal, and in some cases better, friction and wear performance than a maximally hardened case. Thus the case properties could be tailored for specific applications to achieve maximum wear resistance and minimize wear of the tribosystem.

Such large improvements in wear resistance are a direct result of the improved hardness, shear strength, and compressive residual stress within the carburized region of 316L. High hardness limits contact of asperities with the sliding counterface, high shear strength protects the surface layer from the tractional shear stresses experienced during sliding, and the compressive residual stresses diminish the effects of stress concentrations and inhibit crack nucleation and growth by cyclic wear processes. These findings provide experimental evidence of the greatly enhanced tribological performance of 316L austenitic stainless steel when carburized at low temperatures. Low temperature carburization could enable the use of 316L in applications which were previously considered too harsh for this material, including sliding at greater speeds, under greater contact stress, and against harder materials. A tailored carburization process could be used to optimize case thickness and surface hardness in order to maximize wear resistance for certain applications, but, if a critical level of hardening is

not reached, little to no wear resistance enhancement will be realized. This may include the use of shorter treatment times which may also reduce the cost of carburization.

10.0 Recommended Work

Because the field of tribology is very broad, and the tribological behavior of a material is dependent on application conditions, additional experiments characterizing the tribological behavior of low temperature carburized stainless steels in various application conditions would be valuable. Tribological conditions that may warrant further investigation include:

- 1) Corrosive wear in various environments
 - a) marine
 - b) oil and gas related
 - c) marine
 - d) biological

- 2) Lubricated wear for various applications including automotive.
 - a) Characterization of surface film formation and comparison to that of non-treated 316L.

- 3) Contact fatigue and contact/slip studies for bearing applications.
 - a) Because high residual compressive stresses exist within the hardened case of low temperature carburized stainless steel, fatigue is expected to be suppressed within this region. Contact fatigue, which results from cyclic contact stress loading, such as on the raceway of roller bearing components, should be greatly suppressed by the compressive residual stresses within the carburized region of low temperature carburized stainless steels. This is because contact stresses are limited to the near surface region and thus, depending on contact conditions, may only effect material within the case hardened region of low temperature carburized stainless steels (and therefore within the influence of compressive residual stress). Thus, a significant increase in contact fatigue resistance is expected to result from low temperature carburization. (14), (26)

- 4) The effect of lubricating environment on contact fatigue crack growth in low temperature carburized stainless steels for marine bearing, bearings used in corrosive environments, and lubricated bearing applications.
 - a) Is environmentally assisted crack growth (EAC) suppressed by low temperature carburization?

- 5) Fretting
 - a) Fretting is the process by which corrosion and wear synergistically remove material from the surface during small amplitude sliding contact. Low temperature carburized stainless steels should significantly increase fretting resistance due to increased yield strength, shear strength, and compressive residual stresses within the surface hardened region.

- 6) Strain induced martensite (SIM), Corrosive Wear, and Cryogenic Applications.
 - a) SIM forms at room temperature during wear of partially stabilized austenitic stainless steels, such as AISI 316 or AISI 304, due to the high amount of plastic deformation that occurs during wear. Carbon is known to be a strong austenite stabilizer and thus low temperature carburization may significantly stabilize the “expanded austenite” region and prevent SIM formation during wear.
 - b) Improved corrosive wear
 - i) Preventing SIM formation in austenitic stainless steels such as 316L may result in improved corrosive wear resistance due to the absence of austenite-martensite phase boundaries on the surface of tribological contacts.
 - c) Enabling cryogenic application
 - i) Austenitic stainless steels are widely used for cryogenic applications (1) . Metastable austenitic stainless steels may experience SIM formation due to contact damage which can result in brittle fracture due to the cryogenic application temperature being below the ductile to brittle transition temperature (DBTT) of martensite. If SIM is inhibited by the high carbon content of low temperature carburized materials, to what temperature is

the martensite start temperature (M_s) suppressed. If M_s is sufficiently suppressed, low temperature carburization may enable the use of austenitic stainless steels in certain cryogenic applications in which the formation of SIM results in brittle surface fracture. Preventing SIM formation at low temperatures may prevent such fracture from occurring by stabilizing the austenite structure (even when plastically deformed), which is of adequate ductility at low temperatures due to its very low DBTT. (27) (1)

Appendix

A1.0 Wear of Low Temperature Carburized Martensitic Precipitation Hardened Stainless Steels

Pin-on-disk wear tests were conducted on three martensitic precipitation hardened stainless steel alloys, before and after low temperature carburization. The alloys investigated were: 1.) PH13-8, 2.) PH15-5, and 3.) 17-4. Each alloy was supplied by, and carburized at 380°C by the Swagelok Co. These tests were conducted as a feasibility study to gain an understanding of how effectively low temperature carburization could improve the wear resistance of this class of stainless steel alloys.

Low temperature carburization increased the hardness of PH13-8 and PH15-5 by roughly two times, and PH17-4 by more than 3 times (**Fig. A.1**). The high magnitude of hardness increase observed in PH17-4 suggests the possible formation of carbides. If carbides have formed, this would indicate that a lower treatment temperature is needed for PH17-4. The microstructure of these three carburized alloys is being investigated separately from this wear resistance survey.

Hardening of PH Stainless Steels

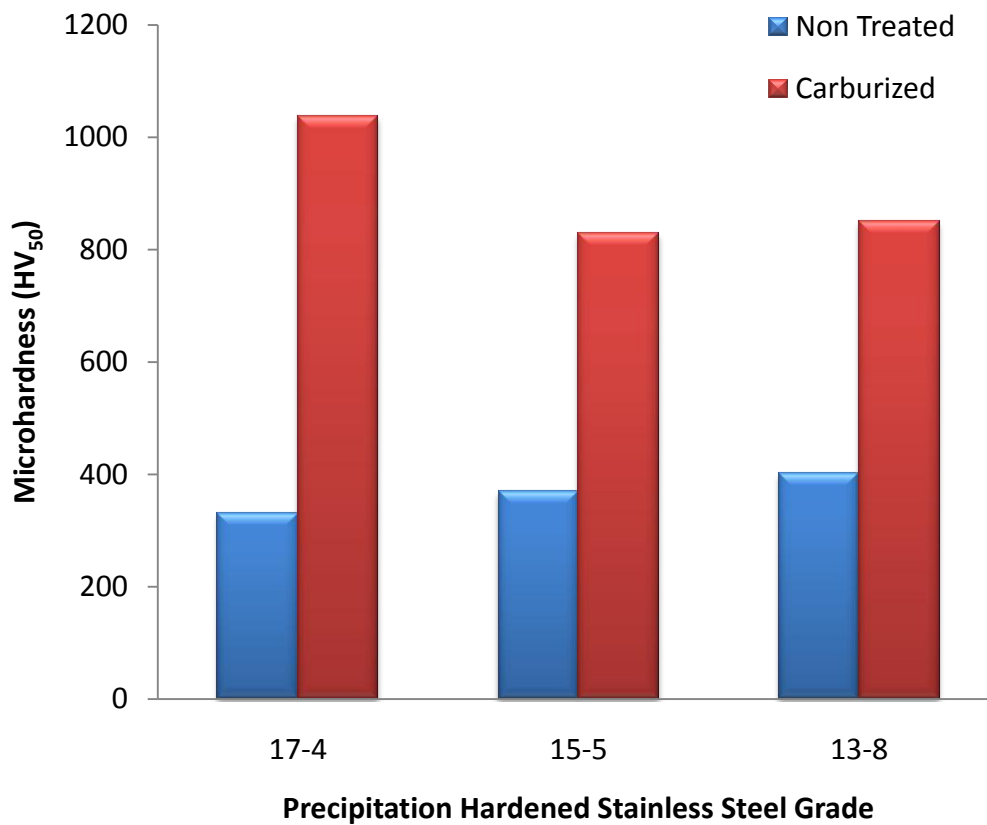


Fig A. 1 Low temperature carburization hardening of precipitation hardened martensitic stainless steels

The wear resistance of these alloys was evaluated using the Case Western Reserve CETR UMT2.0 tribometer pin-on-disk apparatus. An alumina ball (McMaster Carr) was used as the counterface sliding at 0.1 m/s against each disk under an applied load of 5 N, for a total of 10,000 revolutions. The wear track diameter was set at 25 mm for each test. The results show that low temperature carburization results in immensely improved wear resistance for the alloys tested (**Fig. A.2**). PH15-5 wear resistance was increased by ≈ 30 times, PH 13-8 wear resistance was improved by ≈ 50 times, and that of PH17-4 by more than 100 times. This magnitude of wear resistance improvement is

much greater than that observed in 316L, where up to 23x reduction in wear has been observed under similar test conditions.

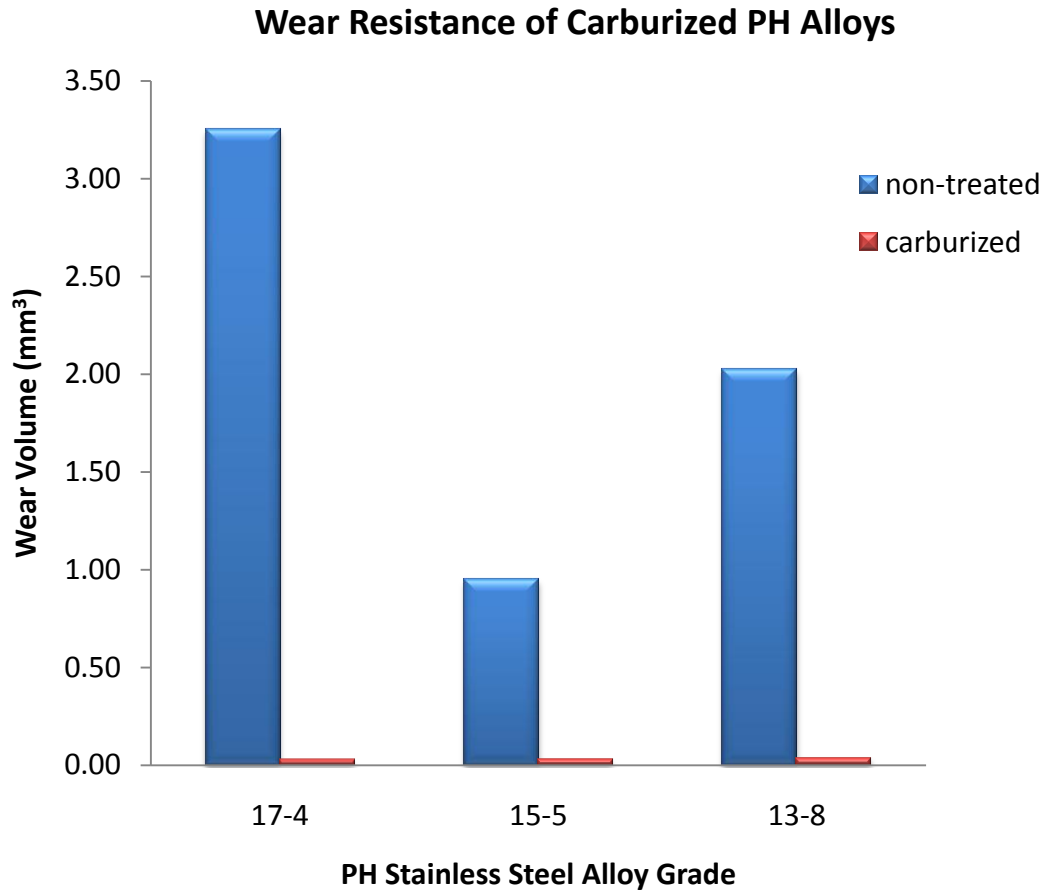


Fig A. 2 Low temperature carburization wear resistance improvement for martensitic precipitation hardened stainless steels

These results demonstrate that low temperature carburization can drastically improve the wear resistance of martensitic precipitation hardened alloys. An investigation of the microstructure of the carburized specimens is needed to identify if any carbides have formed, the concentration of carbon that is in solution within the martensite matrix, and the depth of carbon penetration.

Works Cited

1. *ASM Metals Handbook, 10th edition*. Materials Park, OH : ASM International, 1995.
2. **E. Hall, C. Briant**. Chromium depletion in the vicinity of carbides in sensitized austenitic stainless steels. *Metallurgical Transactions. A*, 1984, Vol. 15, 5:793.
3. **Frank Ernst, Y. Cao, G. Michal, A. Heuer**. Carbide Precipitation in Austenitic Stainless Steel Carburized at Low Temperature. *Acta Materialia*. 2006, 55:1895-1906.
4. **M. Hillert, J. Agren**. On the definitions of paraequilibrium and orthoequilibrium. *Scripta Materialia*. 2004, Vol. 50, 5.
5. **G.M. Michal, et al**. Carbon Supersaturation Due to Paraequilibrium Carburization: Stainless Steels With Greatly Improved Mechanical Properties. *Acta Materialia*. 2006, 54:1597.
6. **F. Martin, et al**. Carburization-Induced Passivity of 316 L Austenitic Stainless Steel. *Electrochemical and Solid-State Letters*. 2007, Vol. 10, 12:76.
7. **G.W. Stachowiak**. *Engineering Tribology*. 3. s.l. : Elsevier Butterworth-Heinemann, 2005.
8. **B. Bhushan**. *Principles and Applications of Tribology*. New York : John Wiley & Sons Inc., 1999.
9. **I.M. Hutchings**. *Tribology: Friction and Wear of Engineering Materials*. s.l. : CRC Press Inc., 1992.
10. **M. Ashby, et al**. Temperature Maps for Frictional Heating in Dry Sliding. *Tribology Transactions*. 1991, 34:577.
11. **K.L. Johnson**. *Contact Mechanics*. 1. Cambridge : Cambridge University Press, 1985.
12. **K. Aoki, T. Shirahata, et al**. *Stainless Steel* . 2001, P. 389.
13. **A. Kapoor, F.J. Franklin**. Tribological Layers and the Wear of Ductile Materials. *Wear*. 2000, 245:204-215.
14. **S. Suresh**. *Fatigue of Materials*. 2 s.l. : Cambridge University Press, 1998.
15. **Lancaster, Herst**. *Journal of Applied Physics*. 1956.
16. **J.K. Lancaster**. *Proceedings of the Royal Society of London*. 1963.

17. **S.C. Lim, et al.** *Acta Metallographica*. 1987.
18. **ASTM.** G99-05 Standard Test Method for Wear Testing with a Pin-on-disk Apparatus. 2007.
19. **P. Blau, et al.** Tribological Properties of Stainless Steels Treated by Colossal Carbon Supersaturation. *Wear*. 2007, 263:719.
20. **M.G. Gee, N.J. McCormick.** The Application of Confocal Scanning Microscopy to the Examination of Ceramic Wear Surfaces. *Journal of Applied Physics*. 1992, 25:A230.
21. **Peter Blau, Jun Qu.** An Efficient Method for Accurately Determining Wear Volumes of Sliders with Non-Flat Wear Scars and Compound Curvatures. *Wear*. 2006, 261:848.
22. **P.J. Blau.** *Friction science and technology: from concepts to applications*. Boca Raton : CRC Press, 2009.
23. **Carpenter Technology Corporation.**
24. **McMaster-Carr Supply Company.**
25. **N. Agarwal, et al.** Enhanced Fatigue Resistance in 316 L Austenitic Stainless Steel Due to Low-Temperature Paraequilibrium Carburization. *Acta Materialia*. 2007, 55:5572.
26. **U. Racke, H. Blumenauer.** Influence of Residual Stress on Fatigue Crack Growth Behavior of Case-Hardening Steels. [book auth.] V Hauk HP Hougardy E Macherauch HD Tietz. *Residual Stresses*. Oberursel : s.n., 1993.
27. **W. Hubner.** Phase transformation in austenitic stainless steels during low temperature stressing. *Tribology International*. 2001, 34.
28. **Williams P, et al, Swagelok Company.** Patent #6,547,888. April 15, 2003.
29. —. Patent #6,461,448. October 8, 2002.
30. —. Patent # 6,165,597. December 26, 2000.
31. —. Patent # 6,093,303. July 25, 2000.
32. **C. Briant, A. Ritter.** The effects of deformation induced martensite on the sensitization of stainless steel. *Metallurgical Transactions. A*, 1980, Vol. 11, 12:2009.
33. **Z.L. Zhung, T. Bell.** *Surface Engineering*. 1985, 1:131.

34. **G.M. Michal, et al.** Carbon Paraequilibrium in Austenitic Stainless Steel.
Metallurgical and Materials Transactions A. 2006, Vol. 37.
35. **E. Rolinski.** *Surface Engineering*. 1987, 3:35.